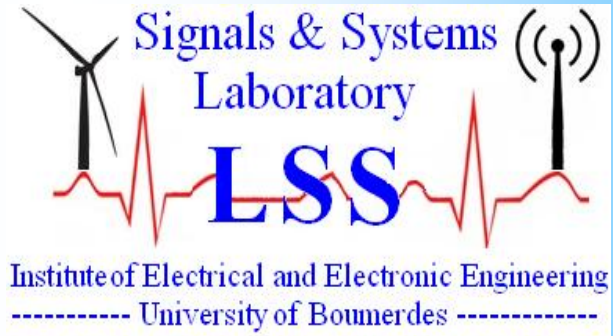


People's Democratic Republic of Algeria
Ministry of Higher Education and Scientific research
M'hamed Bougara University, Boumerdes
Institute of Electrical and Electronic Engineering,
Laboratory of Signals and Systems (LSS)

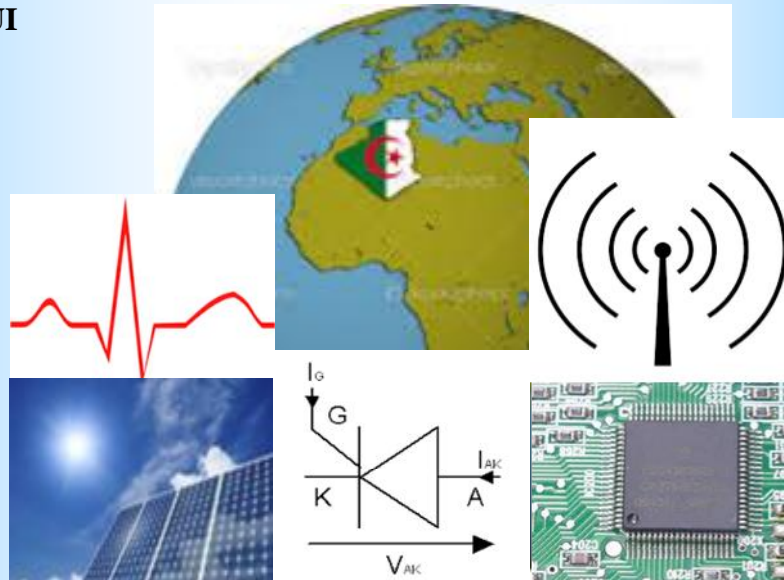


ALGERIAN JOURNAL OF SIGNALS AND SYSTEMS

Journal Director
Pr. Hamid BENTARZI

ISSN : 2543-3792

Journal Editor-in-chief
Dr. Abdelmadjid RECIQUI



Volume : 1 Issue : 1 (June 2016)

Laboratory of Signals and Systems

Address : IGEE (Ex-INELEC), Boumerdes University, Avenue de l'indépendance, 35000, Boumerdes, Algeria

Phone/Fax : 024 79 57 66

Email : lss@univ-boumerdes.dz ; ajsyssig@gmail.com

Director of Journal:

Pr. BENTARZI Hamid

Editor in Chief :

Dr. RECIOUI Abdelmadjid

Editorial Board Members:

Pr. REFOUFI Larbi (Honor member)

Pr. HARICHE Kemal

Pr. AZRAR Arab

Dr. KHELDOUNA Issa

Dr. CHALLAL Mouloud

Dr. DAAMOUCHE A. Elhamid

Dr. KOUADRI A. Elmalek

Dr. OUADI Abderrahmane

Dr. DAHIMENE A. Hakim

Dr. KHOUAS A. Hakim

Mr. ZITOUNI Abdelkader

Reviewer's Board Members

Pr. ALBARBAR A., Manchester Metropolitan University, United Kingdom

Pr. ARSHAD M. K., Univ. of Malaysia Perlis, Malaysia

Pr. AZZOUZI M., Univ. of Djelfa, Algeria

Pr. BECHERIF M, UTMB, France

Pr. BEGUENANE R., Canada

Pr. BELATRECHE A. Univ. of Ulstern, UK

Pr. BENALI K., UCL, Belgium

Pr. BENZID R., Univ. of Batna, Algeria

Pr. BENAMROUCHE N., Univ. of Tizi-ouzou, Algeria

Pr. BERKOUK A., ENP, Algeria

Pr. BENAZZOUZ D., UMBB, Algeria

Pr. BOULAKROUNE M., Univ. of Ouargla, Algeria

Pr. BOUTEJDAR A., Univ. of Magdeburg, Germany

Pr. CHIKOUCHE D., Univ. of M'sila, Algeria

Pr. CHOUBANI F., SUP'COM, Tunisia

Pr. DHERBECOURT P., Université de Rouen, France

Pr. ZEROUG H., USTHB, Algeria

Pr. EL MOUSSATI A., ENSA Oujda, Morocco

Pr. EI- OUALKADI A., Univ. of Abdelmalek Essaadi, Morocco

Pr. ESSAIDI M., Univ. of Titouan, Morocco

Pr. EVAN Vaclavik, Univ. of Switzerland, Switzerland

Pr. FORTAKI T., Univ. of Batna, Algeria

Pr. GUESSOUM A, Univ. of Blida, Algeria

Pr. HADJEM A., Orange Labs, France

Pr. HERZOG, Univ. of Switzerland, Switzerland.

Pr. IKHLEF A., Univ. of Newcastle, United Kingdom

Pr. JOSÉ Ragot, Institut National Polytechnique de Lorraine, France

Pr. KHEZZAR A., Univ. of Constantine, Algeria

Pr. KIDOUUCHE A., UMBB, Algeria

Pr. KRIM F., Univ. of Setif, Algeria

Pr. LACHOURI A., Univ. of Skikda, Algeria

Pr. MAUN J. C., ULB, Belgium

Pr. MEKHALEF S., Univ. of Malaysia, Malaysia

Pr. NAKAMATSU K., Univ. of Hyogo, Japan

Table of contents

Preface	1
Digital Control Fuzzy Logic for a Water Tank Level Using Arduino.....	2
F. Chabni, R. Taleb, A. Benbouali, M.A. Bouthiba	
Fault Tolerant Control of Induction Motor Drives Subject to Rotor Resistance Adaptation.....	11
N. Boumalha, D. Kouchih, M. Tadjine, M.S. Boucherit	
Sensitivity Enhancement of Methane Detection Based On Hollow Core Photonic Crystal Fiber.....	23
R.Boufenar, M. Bouamar, A.Hocini	
Photovoltaic effect in Light Emitting Diodes.....	30
K. Remidi, A. Cheknane, M. Haddadi	
A Combined Sliding Mode Space vector Modulation Control of the Shunt Active Power Filter Using Robust Harmonic Extraction Method.....	37
A. Dahdouh, S. Barkat, A. Chouder	
Hyperchaos-Based Cryptosystem for Multimedia Data Security.....	47
S. Benzegane, S. Sadoudi, M. Djeddou	
Sliding mode control of a Five-Phase Series-Connected Two-Motor Drive.....	59
L. Nezli, O. Zouaid	
Design and Evaluation of a DSP Based Differential Relay of Power Transformer.....	69
A. Abdelmoumene, R.Bouderbala, H.Bentarzi	
Fast Ensemble Empirical Mode Decomposition Using the Savitzky Golay Filter	79
Wahiba Mohguen And Raïs El'hadi Bekka	

Preface

We are honored to announce the publication of the new journal: "Algerian Journal of Signals and Systems", which is published quarterly by the Signals and systems Laboratory at the Institute of Electrical and Electronic Engineering, M'hamed Bougara University of Boumerdes.

Papers dealing with all aspects of electrical systems and signals are considered for publication. Manuscripts must be in English, original and should not be under consideration for publication by any other journals. The authors are invited to upload both the pdf and Word files of their papers using the Website of the journal.

This *Journal* is dedicated to the memory of **Pr. Larbi Refoufi** who passed away on February 1, 2015 at the age of 60 "to God we belong, and to him is our return". **Pr. Larbi Refoufi** is the former director of the research laboratory who has put the first stone of this publication.

We are convinced that «Algerian Journal of Signals and Systems" will provide the opportunity to publish papers with authentic and insightful scientific and technological information on the latest advances in electrical and electronic engineering. We are looking forward to your submission to our Journal.

Journal Director
Pr. Hamid BENTARZI

People's Democratic Republic of Algeria
Ministry of Higher Education and Scientific research
M'hamed Bougara University, Boumerdes
Institute of Electrical and Electronic Engineering,
Laboratory of Signals and Systems (LSS)



ALGERIAN JOURNAL OF SIGNALS AND SYSTEMS

ISSN : 2543-3792

Title: Digital Control Fuzzy Logic for a Water Tank Level Using Arduino

Authors: F. Chabni, R. Taleb, A. Benbouali, M.A. Bouthiba

**Affiliation: Electrical Engineering Department, Hassiba Benbouali University
Laboratoire Génie Electrique et Energies Renouvelables (LGEER), Chlef,
Algeria**

Page range: 2-10

IMPORTANT NOTICE

This article is a publication of the Algerian journal of Signals and Systems and is protected by the copyright agreement signed by the authors prior to its publication. This copy is sent to the author for non-commercial research and education use, including for instruction at the author's institution, sharing with colleagues and providing to institution administration. Other uses, namely reproduction and distribution, selling copies, or posting to personal, institutional or third party

Volume : 1 Issue : 1 (June 2016)

Laboratory of Signals and Systems

Address : IGEE (Ex-INELEC), Boumerdes University, Avenue de l'indépendance, 35000,
Boumerdes, Algeria

Phone/Fax : 024 79 57 66

Email : lss@univ-boumerdes.dz ; ajsyssig@gmail.com

Digital Control Fuzzy Logic for a Water Tank Level Using Arduino

Fayçal CHABNI, Rachid TALEB*, Abderrahmen BENBOUALI, Mohammed Amin BOUTHIBA
Electrical Engineering Department, Hassiba Benbouali University
Laboratoire Génie Electrique et Energies Renouvelables (LGEER), Chlef, Algeria
*r.taleb@univ-chlef.dz

Abstract: Fuzzy logic control has been successfully utilized in various industrial applications; it is generally used in complex control systems, such as chemical process control. Today, most of fuzzy logic controls are still implemented on expensive high performance processors. This paper analyzes the effectiveness of a fuzzy logic control using a low cost controller applied to water level control system. The paper also gives a low cost hardware solution and practical procedure for system identification and control. We started, first by identifying the process to obtain its mathematical model. Then we used two methods to control our system (PI and fuzzy control). Simulation and experimental results are presented.

Keywords: Fuzzy control, PI, Water Tank level, System identification, Arduino.

1. INTRODUCTION

The extraordinary development of digital processors (Microprocessors, Microcontrollers) and their wide use in control systems in all fields have led to significant changes in the design of control systems. Their performance and low cost makes them suitable for use in control systems of all kinds that require a lot more capabilities and performance than those provided by the analog controllers.

In certain industry branches, the liquid level control problem is often encountered. The nature of the liquid and friction of control mechanism and other factors makes the system nonlinear [1, 2]. In nowadays, the best-known industrial process controller is the PID controller because of its simplicity, good robustness, high reliability and it can be easily implemented in any processor, but using a PID controller is not fully convenient when it comes to dealing nonlinear systems [3, 4]. But these systems can be successfully controlled using fuzzy logic controllers because of their independency from the mathematical model of the system.

2. SYSTEM DESCRIPTION

Adjusting a liquid level in a tank is the main objective of this work, the structure of the entire system is as shown in Fig. 1. The system consists of a water tank, a liquid level sensor, a pump based on a 12V direct current motor, an electronic circuit (Arduino and a DC/DC step down converter).

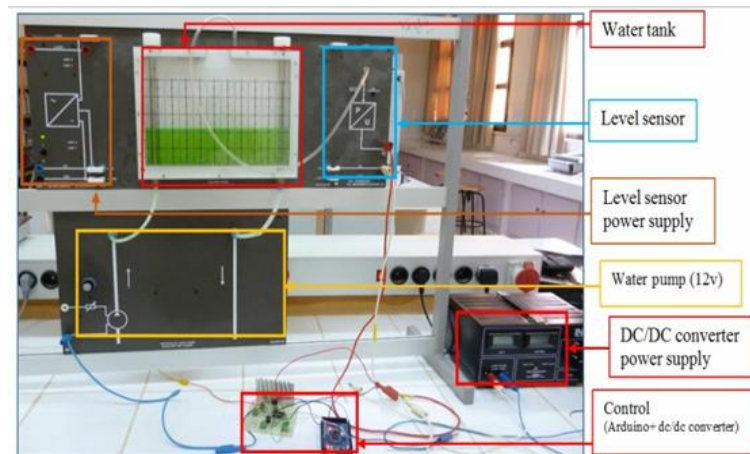


Fig. 1. Structure of water level control

The structure chart of the water tank level system is shown in Fig. 2 which the liquid flows into the top of the tank by a dc motor pump and leaves from the bottom, through a pip equipped with an adjustable valve to adjust manually the flow rate of the liquid leaving the tank and to simulate leaks (disturbances).

The Arduino will act as an acquisition board in identification phase, once we obtain the model of the system the Arduino will play the role of an independent controller, the computer is just used for displaying signals and to impose set points for the controller, it will communicate with the Arduino through RS232 communication.

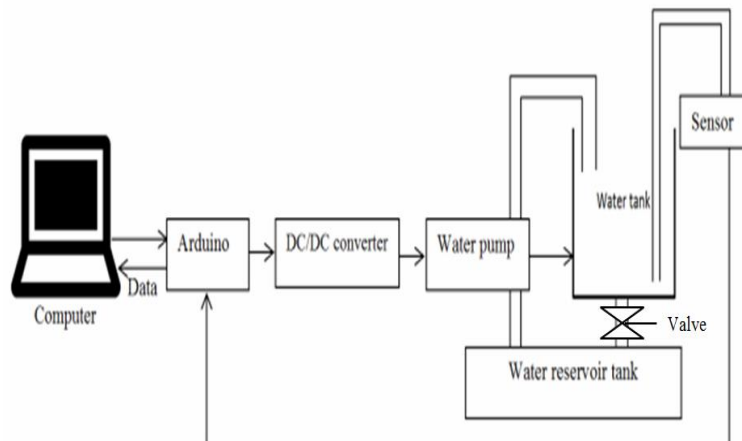


Fig. 2. Structure chart of water tank control system

3. SYSTEM IDENTIFICATION

In order to obtain the mathematical model of the process, we used Arduino as an interface between the computer and the system. The computer is equipped with software that can store incoming samples from Arduino, and then we used "MATLAB identification toolbox" shown in Fig. 3, to process the samples and to obtain the model.

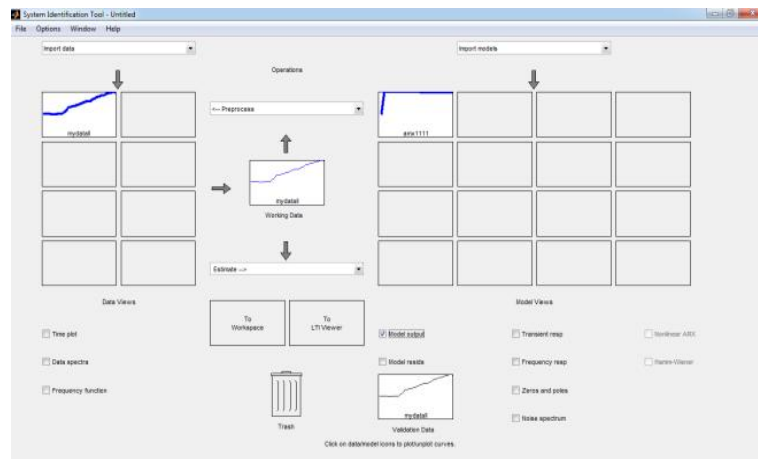


Fig. 3. Graphical user interface of the identification tool box

Fig. 4 shows the open loop response of our system to a constant input $u(t)$, 15.8cm is the final value of the output $y(t)$ to a 7.6 input. This corresponds to the steady-state error of 54.6 percent, which is quite large. That is why we have to design a controller that can eliminate the steady-state error. With the help of MATLAB identification toolbox we deduced that the function transfer and it is:

$$G(z) = \frac{0.004483z^{-1}}{1 - 0.8852z^{-1}}, \text{ sampling time } T_s = 0.2s \quad (1)$$

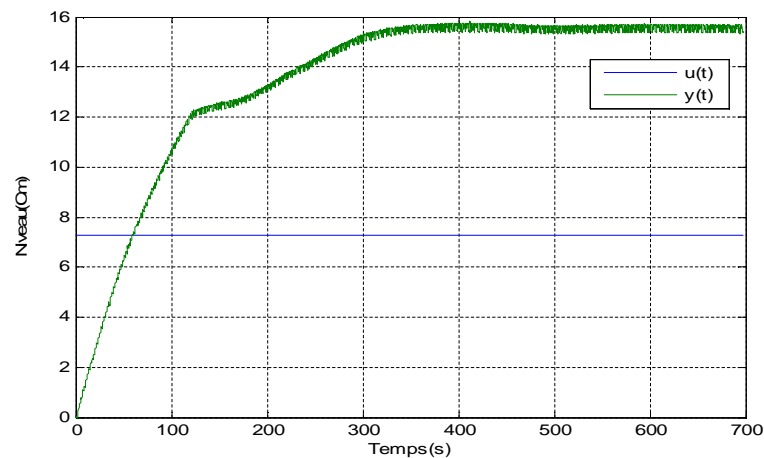


Fig. 4. Response of the system

Fig. 5 represents a comparison between system response and transfer function response to the same input. And we can see that the transfer function response almost matches the reel system response.

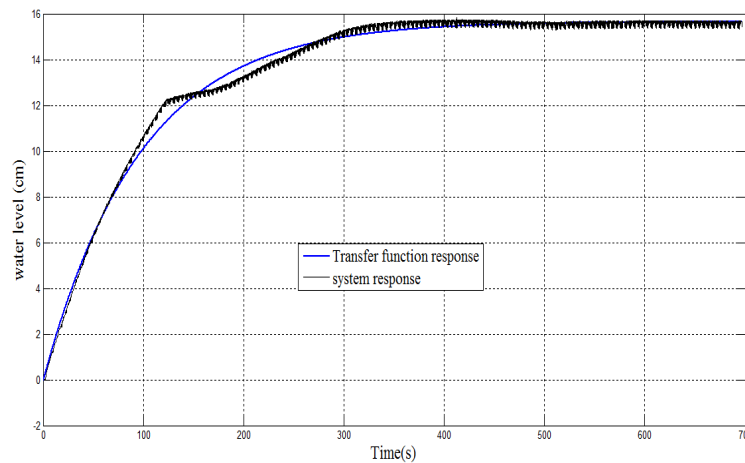


Fig. 5. Comparison between system response and transfer function response to the same input

4. PI CONTROLLER

A Proportional-Integrate-Derivative controller (PID) is a control mechanism, the role of this controller is to minimize the error between a set point and measured data, the control algorithm contains three terms proportional, integrate and derivative term [5, 6]. The most popular controller industrial field is the PI (Proportional-Integrate) controller and it is a special case of a PID controller, it has only two constant parameters K_p and K_i , where K_p is the proportional gain and K_i is the integral gain [7, 8]. The control algorithm $u(t)$ and the controller transfer function $C(p)$ are given by the following relationships:

$$u(t) = K_p (\varepsilon(t) + \frac{1}{\tau_i} \int_0^t \varepsilon(t) dt) \quad (2)$$

$$C(p) = K_p \frac{1 + \tau_i p}{\tau_i p} = K_p (1 + K_i \frac{1}{p}) \quad (3)$$

The design of the PI controller was done using Matlab/Simulink and it was based on the mathematical model obtained from the identification phase. The simulation shown in Fig. 6 was used for testing the performance of our controller, the gains (K_p and K_i) were calculated using pole placement method, ($K_p = 1.145$ and $K_i = 0.015$). Fig. 7 shows the results obtained by the simulation.

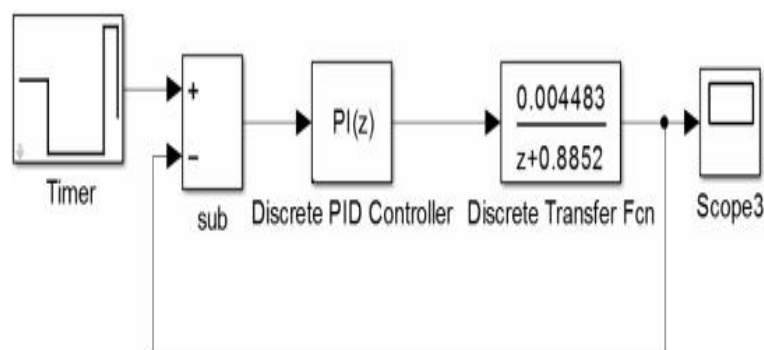


Fig. 6. Simulation of PI controller in simulink

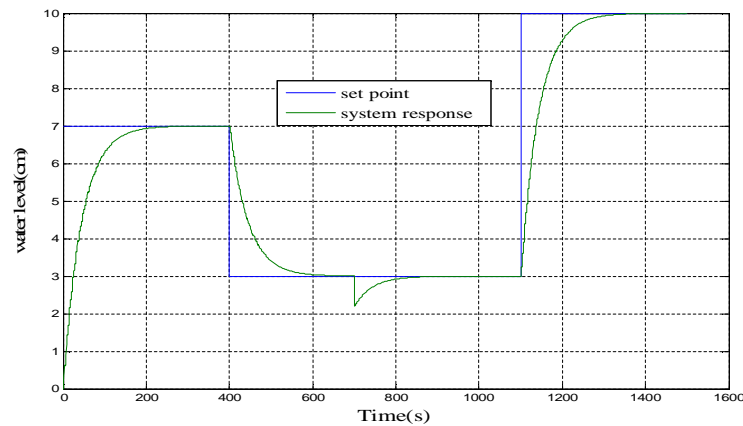


Fig. 7. Behavior of the process with a PI controller (simulation)

After the controller was designed and tested in Matlab/Simulink, the function of the controller mentioned earlier was implemented in Arduino, and then we used it to control our system. Fig 8 presents the behavior of the system with PI controller.

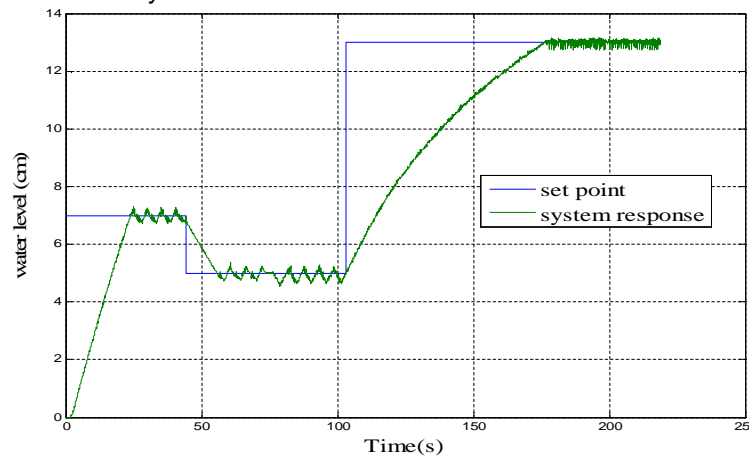


Fig. 8. Behavior of the process with a PI controller (experimental results)

5. FUZZY LOGIC CONTROLLER

The Fuzzy Logic controller consists basically of four parts: fuzzification interface, knowledge base, inference engine, and a defuzzification interface. Fig. 9 shows the basic configuration of a fuzzy logic controller. Each of these parts plays a different role in the control process and affects the performance of the controller and the behavior of the whole system. The fuzzification is the transformation of numerical data from the input to linguistic terms. The knowledge base provides necessary information for all the components of the fuzzy controller [9, 10]. The fuzzy inference engine or the logical decision-making is the core (brain) of the controller. It is capable of simulating the decision-making of human beings. At the end of the inference step, the obtained result is a fuzzy value that we cannot directly use to control our process, so the value should be defuzzified to obtain a crisp value and that is the role of the defuzzification interface.

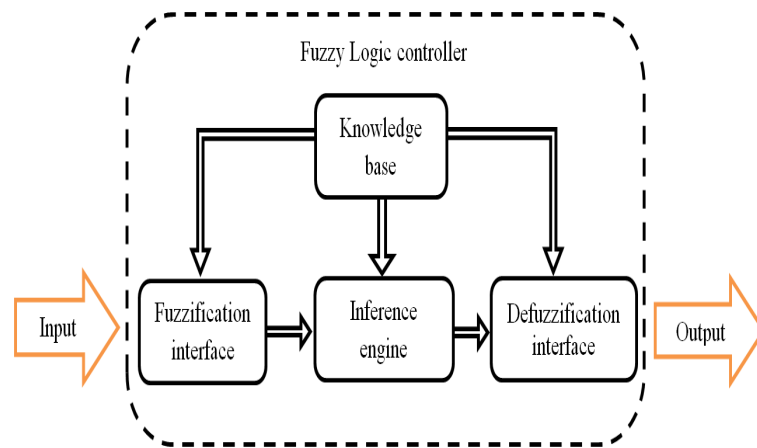


Fig. 9. Basic configuration of a fuzzy logic controller

The fuzzy logic controller usually works with more than two input signals, the system error e and the change rate in the error Δe . The error of the system is defined as the difference between the set point $y_r(k)$ and the plant output $y(k)$ at a moment k :

$$e(k) = y_r(k) - y(k) \quad (4)$$

The variation of the error signal at the moment k is given by the following relationship:

$$\Delta e(k) = e(k) - e(k - 1) \quad (5)$$

The configuration of the proposed fuzzy controller is shown in Fig.10. In1 is the system error and In2 is the variation of the error signal.

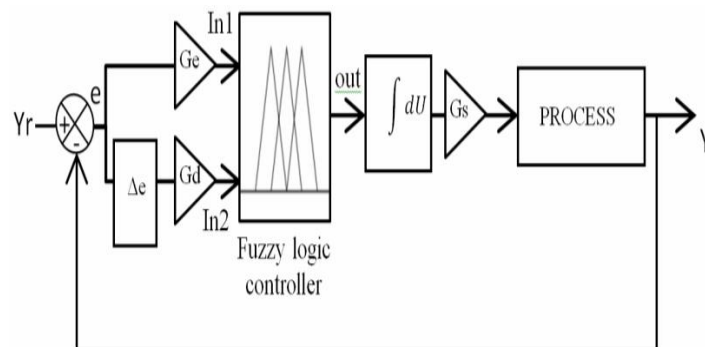


Fig. 10. Fuzzy controller in a closed loop system

The simulation shown in Fig. 11 was used to test the performance of our fuzzy controller and to determine the controller gains.

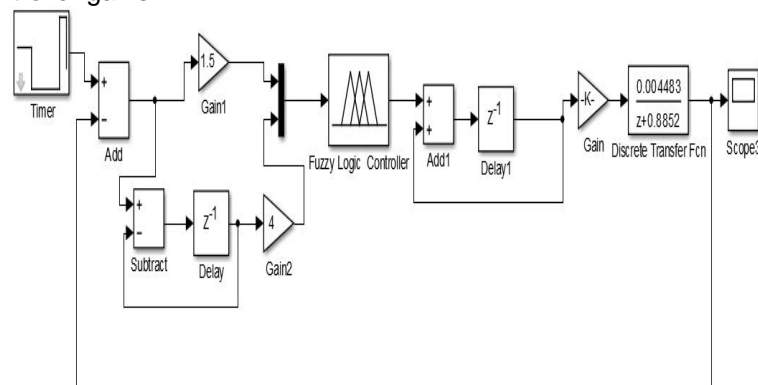


Fig. 11. Simulink model

Using Matlab toolbox “fuzzy logic toolbox”, shown in Fig. 12, we designed a fuzzy logic controller with two inputs (error and error derivative) and one output. The proprieties of our controller are given in the Table. 1.

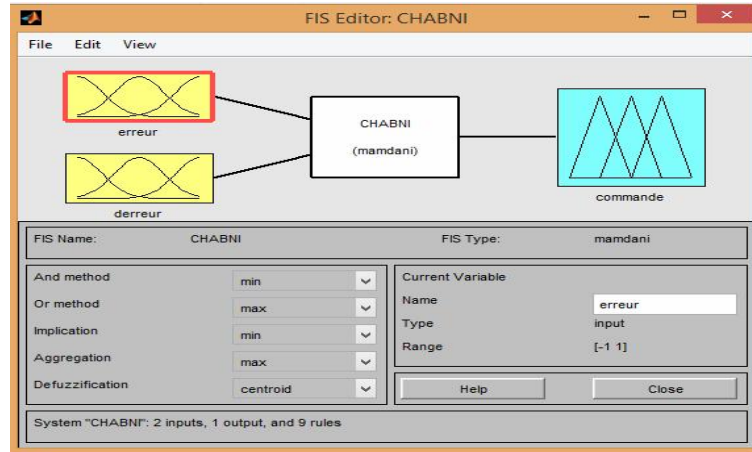


Fig. 12. Graphical user interface of the fuzzy logic toolbox

Table 1. Proprieties of the fuzzy logic controller

Controller type	Mamdani
And method	Min
Or method	Max
Implication	Min
Defuzzification	Centroid

The chosen membership functions of our output and input signals are all similar, they are shown in Fig. 13.

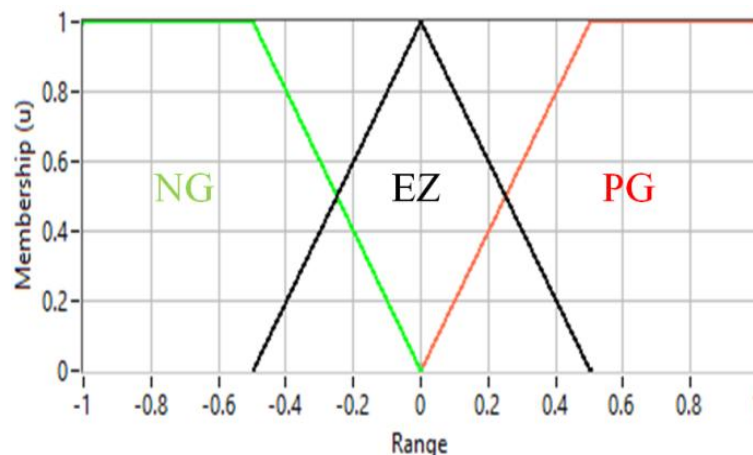


Fig. 13. Membership functions of In1 and In2 and out

The design of the table below (Table .2) was based on the principles of a basic control system which are: If the error is big, and the error rate changes fast, then the controller should eliminate the error quickly and if the error is small, and the error rate change is not fast, then the controller

should eliminate the error slowly and if the error is zero, and the error rate doesn't change, then the control command should be zero. The labels inside the table are linguistic variables.

Table 2. Fuzzy rules

In2 \ In1	NG	EZ	PG
NG	NG	NG	EZ
EZ	NG	EZ	NG
PG	EZ	PG	PG

The labels in the Table 2 are as follows: NG = very low, EZ = zero and PG = very high.

After many simulations we found the values of constants that satisfy our controller standards. Table 3 shows the values of these constants. The result of the simulation is presented in Fig. 14.

Table 3. Controller gains

Error gain (Ge)	1.5
Error changing rate gain (Gd)	4
Output gain (Gs)	150

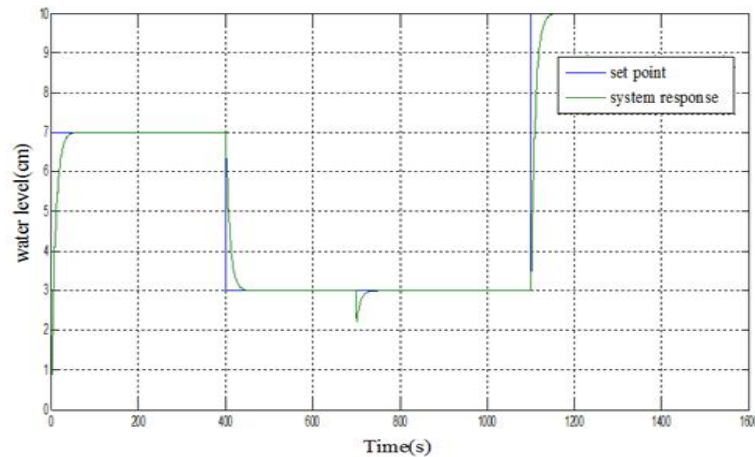


Fig. 14. Behavior of the process with a fuzzy controller (simulation)

After the controller was designed and tested in Matlab/Simulink, the function of the controller mentioned earlier was implemented in Arduino, and then we used it to control our system. Fig. 15 presents the behavior of the system with a fuzzy logic controller.

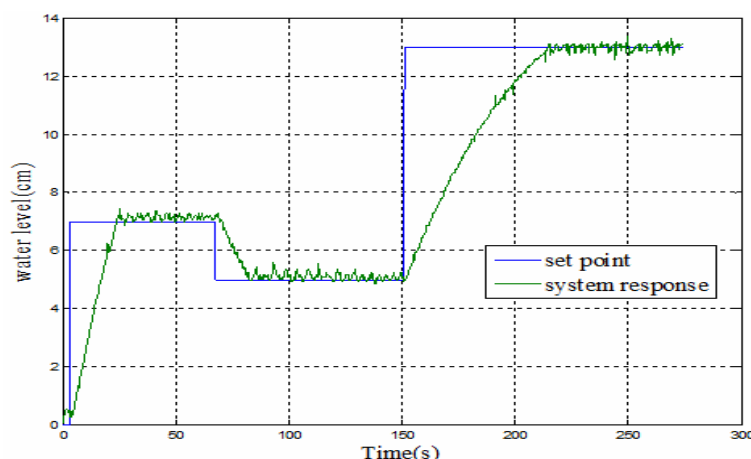


Fig. 15. Behavior of the process with a fuzzy controller (experimental results)

The system was submitted to perturbations (in simulation and experiment). From Figs. 7, 8, 14 and 15 we can see that the fuzzy controller have better performance and stability in every given set point and fast error compensation.

6. CONCLUSION

In this paper we proposed a low cost solution to apply fuzzy logic control for a water tank level control system by using an Arduino, and using it also as a low cost solution for system identification. We reached the main objective of this work which is to test the effectiveness of fuzzy logic control using Arduino, by comparing it to a PI controller. The general structure of both controllers (PI and fuzzy) were presented in this work. The simulations and experimental results showed the superiority of fuzzy control over the conventional control systems.

References

- S. Krivic, M. Hujdur, A. Mrzic, S. Konjicija, "Design and implementation of fuzzy controller on embedded computer for water level control," Proceedings of the 35th International Convention, MIPRO, Opatija, pp. 1747-1751, 21-25 May 2012.
- P. Liu, L. Li, S. Guo, L. Xiong, W. Zhang, J. Zhang, C.Y. Xu, "Optimal design of seasonal flood limited water levels and its application for the Three Gorges Reservoir," Journal of Hydrology, Elsevier Ltd, vol. 527, pp. 1045-1053, August 2015.
- X. Fang, T. Shen, X. Wang, Z. Zhou, "Application and Research of Fuzzy PID in Tank Systems," 4th International Conference on Natural Computation (ICNC'08), Jinan, vol. 4, pp. 326-330, 18-20 October 2008.
- K. Ou, Y.X. Wang, Z.Z. Li, Y.D. Shen, D.J. Xuan, "Feedforward fuzzy-PID control for air flow regulation of PEM fuel cell system," International Journal of Hydrogen Energy, Elsevier Ltd, vol. 40, no. 35, pp. 11686-11695, 21 September 2015.
- V. Vindhya, V. Reddy, "PID-Fuzzy logic hybrid controller for a digitally controlled DC-DC converter," International Conference on Green Computing, Communication and Conservation of Energy (ICGCE), Chennai, pp. 362-366, 12-14 December 2013.
- K. Guesmi, N. Essounbouli, A. Hamzaoui, "Systematic design approach of fuzzy PID stabilizer for DC-DC converters," Energy Conversion and Management, Elsevier Ltd, vol. 49, no. 10, pp. 2880-2889, October 2008.
- C.S. Tan, B. Ismail, M.F. Mohammed, M.F.N. Tajuddin, S. Rafidah, A. Rahim, Z.M. Isa, "Study of Fuzzy and PI controller for Permanent-Magnet Brushless DC motor drive," 4th International on Power Engineering and Optimization Conference (PEOCO), Shah Alam, pp. 517-521, 23-24 June 2010.
- A. Terki, A. Moussi, A. Betka, N. Terki, "An improved efficiency of fuzzy logic control of PMLBDC for PV pumping system," Applied Mathematical Modelling, Elsevier Ltd, vol. 36, no. 3, pp. 934-944, March 2012.
- M.S.M. Aras, S.N. Bin Syed Salim, E.C.S. Hoo, I.A.B.W.A. Razak, M. Hendra Bin Hairi, "Comparison of Fuzzy Control Rules Using MATLAB Toolbox and Simulink for DC Induction Motor-Speed Control," International Conference of Soft Computing and Pattern Recognition (SOCPAR'09), Malacca, pp. 711-715, 4-7 December 2009.
- G. Bosque, I. Del Campo, J. Echanobe, "Fuzzy systems, neural networks and neuro-fuzzy systems: A vision on their hardware implementation and platforms over two decades," Engineering Applications of Artificial Intelligence, Elsevier Ltd, vol. 32, pp. 283-331, June 2014.

People's Democratic Republic of Algeria
Ministry of Higher Education and Scientific research
M'hamed Bougara University, Boumerdes
Institute of Electrical and Electronic Engineering,
Laboratory of Signals and Systems (LSS)



ALGERIAN JOURNAL OF SIGNALS AND SYSTEMS

ISSN : 2543-3792

Title: Fault Tolerant Control of Induction Motor Drives Subject to Rotor Resistance Adaptation

Authors: N. Boumalha, D. Kouchih, M. Tadjine, M.S. Boucherit

Affiliation: Electronic Department, University Saad Dahlab, Blida, Algeria

Page range: 11-22

IMPORTANT NOTICE

This article is a publication of the Algerian journal of Signals and Systems and is protected by the copyright agreement signed by the authors prior to its publication. This copy is sent to the author for non-commercial research and education use, including for instruction at the author's institution, sharing with colleagues and providing to institution administration. Other uses, namely reproduction and distribution, selling copies, or posting to personal, institutional or third party websites are not allowed.

Volume : 1 Issue : 1 (June 2016)

Laboratory of Signals and Systems

Address : IGEE (Ex-INELEC), Boumerdes University, Avenue de l'indépendance, 35000, Boumerdes, Algeria

Phone/Fax : 024 79 57 66

Email : lss@univ-boumerdes.dz ; ajsyssig@gmail.com

Fault Tolerant Control of Induction Motor Drives Subject to Rotor Resistance Adaptation

N. Boumalha ^{(1)*}, D. Kouchih ⁽²⁾, M. Tadjine ⁽¹⁾, M.S. Boucherit ⁽¹⁾

⁽¹⁾Automation Control Department, National Polytechnic School, Alger, Algeria

⁽²⁾Electronic Department, University Saad Dahlab, Blida, Algeria

E-mail: (boumalhanoureddine/djkouchih/tadjine/ms_boucherit@yahoo.fr)

Abstract: This paper describes the synthesis of a vector fault tolerant control of induction motor drives using an adaptive observer. This observer is used to detect the rotor resistance and flux components using the stator terminal voltages and currents. The rotor resistance is adapted using a new algorithm which does not imply a high computational load. Stability analysis based on Lyapunov theory is performed in order to guarantee the closed loop stability. The rotor resistance is used for the correction of the controllers and the rotor time constant. To verify the tolerance and the applicability of this control, we consider the stator inter-turn fault which is frequently encountered in practice. An analytical method for the modelling of this fault is presented. The equations which describe the transient as well as steady state behavior of unsymmetrical induction machine including the computation of machine inductances are presented. These inductances are calculated analytically using the magnetic field distribution through the machine air-gap. Simulation results are provided to evaluate the consistency and performance of the proposed fault tolerant control of induction motor based vector control.

Keywords— Adaptive observer; Fault tolerant control; Induction machine; Vector control.

I. INTRODUCTION

The induction machine (IM) is used in wide variety of applications as a mean of converting energy. Pumps, electrical vehicles and asynchronous generators are but few applications of large IM. The vector control has been recognized as the algorithm that gives the IM drives fast dynamic response. It provides the same performances as achieved by direct current machines. The IM are subject to different faults, due to a combination of thermal overloading, transient voltage stresses, mechanical stresses and environmental stresses [1-4]. From a number of surveys, it can be deduced that stator faults account approximately 40 % of all failures. An important problem is that the rotor resistance varies with respect to abnormal conditions. For vector controlled IM, the rotor resistance variation modifies the performances of the control system when we use a control law with fixed parameters [5-6]. Therefore, the fault tolerant control (FTC) is necessary to preserve some pre-specified performances: continuity, quality of services and stability. Some FTC schemes require explicit detection and estimation of the fault (active FTC), while some FTC schemes operate using robust controllers without such explicit detection (passive FTC) [7-9]. The proposed FTC is a combination between an active and passive FTC. The advantage of this combined FTC is that when the fault is not tolerant an alarm signal will indicate that the operator's intervention is necessary. The proposed approach consists to compensate the rotor resistance variation, due to faults, using a new algorithm for an online adaptation. Many researches have been done on adaptation of the rotor resistance [10-15]. In this paper, a new algorithm is proposed for the adaptation of the rotor resistance. This method is established using stability analysis based on Lyapunov theory. It is important to note that for low speed operation, the appropriate fault harmonics approach the fundamental frequency. In this condition, the distinction between the different harmonics is delicate and the classical spectral analysis of stator current is inconvenient for fault detection [16-17]. The observed rotor resistance is considered as a very interesting tool for this purpose. The research on condition monitoring and fault tolerant control of IM needs an accurate model. For this purpose, we have to elaborate a suitable model which enables us to predict the performances and to extract fault signatures on electromagnetic torque and stator current of unsymmetrical IM. The machine inductances are calculated analytically from the machine structure using the magnetic field distribution through the machine air-gap. The obtained faulty model provides a good compromise between modeling accuracy and simulation time. To verify the consistency and the applicability of the proposed approach, we consider the variation of rotor resistance due to temperature and the operation of IM with stator interturn fault. The contribution of this paper is that it provides an effective FTC strategy using a new and practical algorithm for the adaptation of rotor resistance. In addition, a new approach for the modelling of unsymmetrical IM is proposed.

II. VECTOR CONTROL TECHNIQUE

In order to obtain the machine inductances, firstly should be obtained the spatial distribution of magnetomotive force produced by a phase “j” of the stator windings. Using this distribution it is possible to get the harmonic components of magnetic flux linkage between the two phases “i” and “j”. The principle of the vector control is that the torque and flux of the IM are controlled separately similarly to the direct current machine with separate excitation. The vector control is based on the orientation of the rotating frame d-q axis, as the d axis coincides with the rotor flux direction. The orientation of the magnetic flux along the d axis led to the annulation of the quadrature component, thus

$$\begin{aligned} \phi_{qr} &= 0 \\ \phi_{dr} &= \phi_r \end{aligned} \tag{1}$$

In a reference frame according to the rotating field, the voltage equations in the synchronously reference frame are

$$\begin{cases} \frac{di_{ds}}{dt} = -\frac{1}{\sigma L_s} \left(R_s + R_r \frac{L_m^2}{L_r} \right) i_{ds} + \omega_s i_{qs} + \frac{1}{\sigma L_s} \left(R_r \frac{L_m}{L_r} \right) \phi_{dr} + \frac{1}{\sigma L_s} v_{ds} \\ \frac{di_{qs}}{dt} = \omega_s i_{ds} - \frac{1}{\sigma L_s} \left(R_s + R_r \frac{L_m^2}{L_r} \right) i_{qs} - \frac{1}{\sigma L_s} \left(\frac{L_m}{L_r} \right) \omega_s \phi_{dr} + \frac{1}{\sigma L_s} v_{qs} \\ \frac{d\phi_{dr}}{dt} = R_r \frac{L_m}{L_r} i_{ds} - \frac{R_r}{L_r} \phi_{dr} \\ J \frac{d\Omega}{dt} = T_e - T_l - f_v \Omega \end{cases} \tag{2}$$

v_{ds} , v_{qs} are the components of stator voltage vector, i_{ds} , i_{qs} are the components of stator current vector, ϕ_{dr} , ϕ_{qr} are the components of rotor flux vector, σ is the leakage factor, R_s and R_r are stator and rotor resistance, L_s and L_r represent the stator and rotor cyclic inductances and L_m is the stator-rotor cyclic mutual inductance. ω_s , ω are the stator and mechanical pulsation. J is the inertia of the rotor and the connected load, T_e the electromagnetic torque, T_l the load torque, Ω the mechanical angular speed and f_v is the viscose friction coefficient. For vector controlled IM. The block diagram of the proposed control scheme of induction motor is represented in Figure 4. The blocs SMC1, SMC2, and SMC3 are sliding mode controllers.

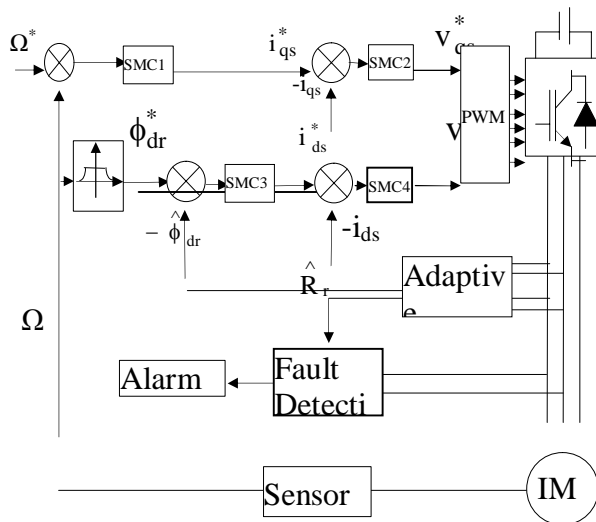


Fig. 1. Vector Fault tolerant Control scheme

III. ADAPTIVE OBSERVER

The objective is to determine the mechanism adaptation of the rotor resistance. The structure of the observer is based on the induction motor model in stator reference frame. The adaptive observer is represented in figure 2.

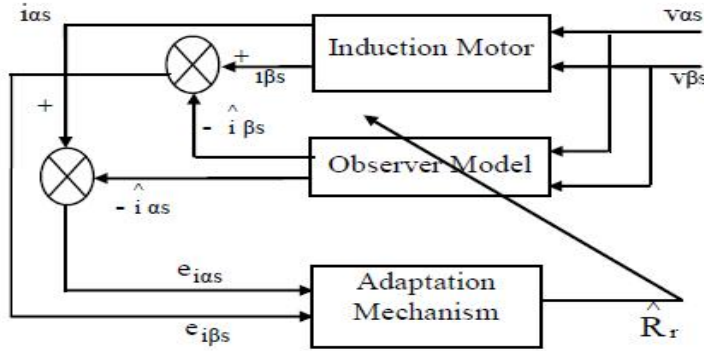


Fig. 2. Global adaptive observer.

In the stationary reference frame, the state equations of the induction motor are expressed.

$$\begin{cases} \frac{di_{\alpha s}}{dt} = -\frac{1}{\sigma L_s} \left(R_s + R_r \frac{L_m^2}{L_r^2} \right) i_{\alpha s} + \frac{1}{\sigma L_s} R_r \frac{L_m}{L_r^2} \Phi_{\alpha r} + \frac{1}{\sigma L_s} \omega \frac{L_m}{L_r} \Phi_{\beta r} + \frac{1}{\sigma L_s} v_{\alpha s} \\ \frac{di_{\beta s}}{dt} = -\frac{1}{\sigma L_s} \left(R_s + R_r \frac{L_m^2}{L_r^2} \right) i_{\beta s} - \frac{1}{\sigma L_s} \omega \frac{L_m}{L_r} \Phi_{\alpha r} + \frac{1}{\sigma L_s} R_r \frac{L_m}{L_r^2} \Phi_{\beta r} + \frac{1}{\sigma L_s} v_{\beta s} \\ \frac{d\Phi_{\alpha r}}{dt} = \frac{R L_m}{L} i_{\alpha s} - \frac{R_r}{L} \Phi_{\alpha r} - \omega \Phi_{\beta r} \\ \frac{d\Phi_{\beta r}}{dt} = \frac{R L_m}{L} i_{\beta s} - \frac{R_r}{L} \Phi_{\beta r} + \omega \Phi_{\alpha r} \end{cases} \quad (3)$$

$v_{\alpha s}$, $v_{\beta s}$ are the components of stator voltage vector, $i_{\alpha s}$, $i_{\beta s}$ are the components of stator current vector, $\Phi_{\alpha r}$, $\Phi_{\beta r}$ are the components of rotor flux vector.

The IM state model is expressed in the nonlinear form as follows.

$$\begin{cases} \frac{dX}{dt} = f(x, u) \\ y = h(x, u) \end{cases} \quad (4)$$

$$X^T = (i_{\alpha s} \ i_{\beta s} \ \Phi_{\alpha r} \ \Phi_{\beta r}), \ Y = \begin{pmatrix} i_{\alpha s} \\ i_{\beta s} \end{pmatrix}, \ U = \begin{pmatrix} v_{\alpha s} \\ v_{\beta s} \end{pmatrix}$$

By linearizing the above state model, we can write:

$$\begin{cases} \frac{dX}{dt} = AX + BU \\ Y = CX \end{cases} \quad (5)$$

$$A = \frac{\partial f}{\partial x}, B = \frac{\partial f}{\partial u}$$

$$C_i = \frac{\partial h}{\partial x} \tag{6}$$

The matrices are defined by

$$A = \begin{pmatrix} -a & 0 & \frac{R_r L_m}{L_r b} & \omega \frac{L_m}{b} \\ 0 & -a & -\omega \frac{L_m}{b} & \frac{R_r L_m}{L_r b} \\ \frac{R_r L_m}{L_r} & 0 & \frac{R_r}{L_r} & -\omega \\ 0 & \frac{R_r L_m}{L_r} & +\omega & -\frac{R_r}{L_r} \end{pmatrix}, B = \begin{pmatrix} \frac{1}{\sigma L_s} & 0 \\ 0 & \frac{1}{\sigma L_s} \\ 0 & 0 \\ 0 & 0 \end{pmatrix}, C = \begin{pmatrix} 1 & 0 & 0 & 0 \\ 0 & 1 & 0 & 0 \end{pmatrix}$$

$$a = \frac{1}{\sigma L_s} \left(R_s + R_r \frac{L_m^2}{L_r^2} \right), b = \sigma L_s L_r, \sigma = 1 - \frac{L_m^2}{L_s L_r}$$

A linear state observer can then be derived by considering the mechanical speed as a constant parameter during the sampling time. This is considered because its variation is very slow comparing to the electrical variables. The model of the observer is expressed [18-19]

$$\begin{cases} \frac{d\hat{X}}{dt} = \hat{A}\hat{X} + BU + G(Y - \hat{Y}) \\ \hat{Y} = C\hat{X} \end{cases} \tag{7}$$

The matrix of gain G is selected such as the eigenvalues of the matrix A-GC are in the left plane half of the complex plan and that the real part of the eigenvalues is larger in absolute value than the real part of the eigenvalues of the state matrix A [18-19].

The machine parameters are assumed to be perfectly known, the rotor resistance is unknown. We define

$$\delta R_r = R_r - \hat{R}_r \tag{8}$$

The symbol $\hat{}$ denotes estimated values and G is the observer gain matrix.

We will determine the differential system describing the evolution of the error

$$e = X - \hat{X} \tag{9}$$

The state matrix of the observer can be written

$$\hat{A} = A + \delta A \tag{10}$$

$$\delta A = \begin{pmatrix} +\frac{1}{\sigma L_s} \delta R_r & 0 & -\frac{L_m}{b L_r} \delta R_r & 0 \\ 0 & +\frac{1}{\sigma L_s} \delta R_r & 0 & -\frac{L_m}{b L_r} \delta R_r \\ -\frac{L_m}{L_r} \delta R_r & 0 & \frac{\delta R_r}{L_r} & +\delta \omega \\ 0 & -\frac{L_m}{L_r} \delta R_r & 0 & \frac{\delta R_r}{L_r} \end{pmatrix} \tag{11}$$

Then, we can write

$$\frac{d\hat{X}}{dt} = \hat{A}\hat{X} + BU - GCe \quad (12)$$

Thus

$$\frac{de}{dt} = (A - GC)e - \delta A \hat{X} \quad (13)$$

We define the Lyapunov function

$$V = e^T e + \frac{(\delta R_r)^2}{\lambda} \quad (14)$$

λ is a positive scalar. The Lyapunov function should contain term of the difference δR_r to obtain mechanism adaptation. The stability of the observer is guaranteed for the condition [20-21]

$$\frac{dV}{dt} < 0 \quad (15)$$

The derivative of the Lyapunov function

$$\frac{dV}{dt} = 2e^T \frac{de}{dt} + 2 \frac{\delta R_r}{\lambda} \frac{d\delta R_r}{dt} \quad (16)$$

The first term becomes

$$2e^T \frac{de}{dt} = 2e^T (A - GC)e - 2e^T \delta A \hat{X} \quad (17)$$

The rotor flux components cannot be measured. In addition, the flux dynamic is faster than the machine parameters dynamic. To obtain the adaptation mechanism of the rotor resistance, we accept that

$$\begin{aligned} \hat{\Phi}_{\alpha r} &= \Phi_{\alpha r} \\ \hat{\Phi}_{\beta r} &= \Phi_{\beta r} \end{aligned} \quad (18)$$

Thus

$$e^T \delta A \hat{X} = \frac{\delta R_r}{\sigma L_s} \delta R_r \left(\hat{i}_{\alpha s} e_{i\alpha s} + \hat{i}_{\beta s} e_{i\beta s} \right) - \frac{L_m}{b L_r} \delta R_r \left(\hat{\Phi}_{\alpha r} e_{i\alpha s} + \hat{\Phi}_{\beta r} e_{i\beta s} \right) \quad (19)$$

For the second term of (16), we can write

$$2 \frac{\delta R_r}{\lambda} \frac{d\delta R_r}{dt} = 2 \frac{\delta R_r}{\lambda} \frac{dR_r}{dt} - 2 \frac{\delta R_r}{\lambda} \frac{d\hat{R}_r}{dt} \quad (20)$$

We consider the hypothesis of a slowly varying regime for the machine parameters, thus

$$\frac{dR_r}{dt} \approx 0 \quad (21)$$

Consequently

$$\frac{d\delta R_r}{dt} = - \frac{d\hat{R}_r}{dt} \quad (22)$$

Finlay, we obtain

$$\frac{dV}{dt} = 2e^T(A - GC)e - 2\frac{\delta R_r}{\lambda} \frac{d\hat{R}_r}{dt} + 2\delta R_r \left[\frac{L_m}{bL_r} \left(\hat{\Phi}_{\alpha r} e_{i\alpha s} + \hat{\Phi}_{\beta r} e_{i\beta s} \right) - \frac{1}{\sigma L_s} \left(\hat{i}_{\alpha s} e_{i\alpha s} + \hat{i}_{\beta s} e_{i\beta s} \right) \right] \quad (23)$$

If the term $2e^T(A - GC)e$ is negative, the condition $\frac{dV}{dt} < 0$ is verified for

$$2\delta R_r \left[\frac{L_m}{bL_r} \left(\hat{\Phi}_{\alpha r} e_{i\alpha s} + \hat{\Phi}_{\beta r} e_{i\beta s} \right) - \frac{1}{\sigma L_s} \left(\hat{i}_{\alpha s} e_{i\alpha s} + \hat{i}_{\beta s} e_{i\beta s} \right) \right] - 2\frac{\delta R_r}{\lambda} \frac{d\hat{R}_r}{dt} = 0 \quad (24)$$

This condition can be verified if

$$\frac{d\hat{R}_r}{dt} = +\lambda \left[\frac{L_m}{bL_r} \left(\hat{\Phi}_{\alpha r} e_{i\alpha s} + \hat{\Phi}_{\beta r} e_{i\beta s} \right) - \frac{1}{\sigma L_s} \left(\hat{i}_{\alpha s} e_{i\alpha s} + \hat{i}_{\beta s} e_{i\beta s} \right) \right] \quad (25)$$

We obtain the adaptation mechanism in the form

$$\hat{R}_r = \int_0^t \left[\frac{L_m}{bL_r} \left(\hat{\Phi}_{\alpha r} e_{i\alpha s} + \hat{\Phi}_{\beta r} e_{i\beta s} \right) - \frac{1}{\sigma L_s} \left(\hat{i}_{\alpha s} e_{i\alpha s} + \hat{i}_{\beta s} e_{i\beta s} \right) \right] dt \quad (26)$$

The estimated electromagnetic torque is expressed

$$\hat{C}_e = \frac{3}{2} p \frac{L_m}{L_r} \left(\hat{\Phi}_{\alpha r} \hat{i}_{\beta s} - \hat{\Phi}_{\beta r} \hat{i}_{\alpha s} \right) \quad (27)$$

IV. MODELING OF UNSYMETRICAL IM

A. Modeling of interturn fault

In IM, coils are insulated one from other in slots as in end winding region. The biggest probability for inter-turn fault is inter-turn between turns in the same coil. When an inter-turn fault occurs, the phase winding has less turns. As a result of the inter-turn fault, the mutual between the phase in which inter-turn is occurred and all of the circuits in machine are altered. Initially, we consider the sample example, where the coil U-V has four turns and occupied two slots. When, a short circuit occurred between the contact points c_1 and c_2 , three turns in series are obtained. In addition, a new short-circuited turn which we call the short circuited phase D is created and magnetically coupled with all the other circuits. It is evident that the phase current and the currents which follow in the short-circuited phase produce opposite MMFs.

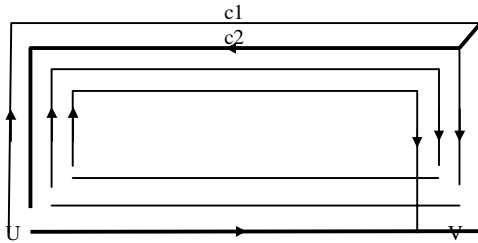


Fig. 3. Short-circuited coil.

The new phase D is described by the voltage equation

$$r_d i_d + \frac{d\Phi_d}{dt} = 0 \quad (28)$$

Φ_d , i_d and r_d are respectively the magnetizing flux, the current and the resistance of the new phase D.

Applying the following method for the calculation of machine inductances, we obtain the self and mutual inductance of the new phase and all the other circuits.

The equations describing the three phase induction machine with n rotor's bars can be written in the conventional vector-matrix form, wherein the machine parameters are calculated in the healthy and faulty modes.

B. Stator voltage equations

In the case of unsymmetrical conditions, we employ line to line voltages as inputs in simulation model. The stator voltage equation becomes

$$[\mathbf{u}_{sf}] = [\mathbf{R}_s] [\mathbf{i}_{sf}] + \frac{d[\Phi_{sf}]}{dt} \quad (29)$$

$$[\mathbf{u}_{sf}] = [u_{ab} \ u_{bc} \ u_{ca} \ 0]^T$$

$$[\mathbf{i}_{sf}] = [i_{as} \ i_{bs} \ i_{cs} \ i_d]^T$$

$$[\mathbf{R}_s] = \begin{bmatrix} r_{as} & -r_{bs} & 0 & 0 \\ 0 & +r_{bs} & -r_{cs} & 0 \\ -r_{as} & 0 & +r_{cs} & 0 \\ 0 & 0 & 0 & +r_d \end{bmatrix} \quad (30)$$

u_{ab} , u_{bc} and u_{ca} are the line to line voltages.

i_{as} , i_{bs} and i_{cs} are the line currents.

r_{as} , r_{bs} and r_{cs} are the resistances of stator windings.

The flux equations are expressed

$$[\Phi_{sf}] = [A_f] [\Phi_s] \quad (31)$$

$$[\Phi_s] = [L_{ss}] [i_s] + [L_{sr}] [i_r] \quad (32)$$

$$[A_f] = \begin{bmatrix} +1 & -1 & 0 & 0 \\ 0 & +1 & -1 & 0 \\ -1 & 0 & +1 & 0 \\ 0 & 0 & 0 & +1 \end{bmatrix} \quad (33)$$

L_{ss} , and L_{sr} are the matrices of the stator, and the stator-rotor mutual inductances. i_r is the rotor vector current.

When lots of short-circuited turns are created. They will be identical and have no conductive contact with other phases. They can be analyzed with the same manner as the case of one short-circuited turn.

C. Rotor voltage equations

The rotor cage is composed of n bars and the end ring circuit. It is modeled by an equivalent circuit containing n magnetically coupled circuits. Each rotor loop consists of two adjacent bars and the two portions of the end ring connect them as follows.

The rotor voltage equation is expressed

$$0 = [\mathbf{R}_r] [\mathbf{i}_r] + \frac{d[\Phi_r]}{dt} \quad (34)$$

With

$$[\Phi_r] = [L_{rs}] [i_s] + [L_{rr}] [i_r] \quad (35)$$

$$[L_{rs}] = [L_{sr}]^T \quad (36)$$

$[i_r]$ is the rotor vector current;

$[R_r]$ is the n by n symmetric matrix of the rotor resistances;

$[L_{rs}]$ is the matrix of rotor-stator mutual inductances;

n is the number of bars.

In the case of healthy rotor, it can be demonstrated that [22-23]

$$[R_r] = \begin{bmatrix} R_0 & -r_b & 0 & \dots & \dots & 0 & -r_b \\ -r_b & R_0 & -r_b & \dots & \dots & 0 & 0 \\ \dots & \dots & \dots & \dots & \dots & \dots & \dots \\ \dots & \dots & \dots & \dots & \dots & \dots & \dots \\ 0 & 0 & \dots & \dots & -r_b & R_0 & -r_b \\ -r_b & 0 & \dots & \dots & \dots & -r_b & R_0 \end{bmatrix} \quad (37)$$

$$R_0 = 2(r_b + r_e) \quad (38)$$

r_e is the end ring segment resistance and r_b is the total bar resistance.

L_{rr} is the n by n symmetric matrix of the rotor inductances. In the case of healthy rotor, it can be verified that [22-23]

$$[L_{rr}] = \begin{bmatrix} L_{kk}+L_0 & L_{km}-l_b & L_{km} & \dots & L_{km} & L_{km} & L_{km}-l_b \\ L_{km}-l_b & L_{kk}+L_0 & L_{km}-l_b & \dots & L_{km} & L_{km} & L_{km} \\ \dots & \dots & \dots & \dots & \dots & \dots & \dots \\ \dots & \dots & \dots & \dots & \dots & \dots & \dots \\ L_{km} & L_{km} & \dots & \dots & L_{km}-l_b & L_{kk}+L_0 & L_{km}-l_b \\ L_{km}-l_b & L_{kj} & \dots & \dots & \dots & L_{km}-l_b & L_{kk}+L_0 \end{bmatrix} \quad (39)$$

$$L_0 = 2(l_b + l_e) \quad (40)$$

L_{kk} is the magnetizing inductance of each rotor loop, l_b is the rotor bar leakage inductance and l_e is the rotor end ring leakage inductance. L_{km} is the mutual inductance between two rotor loops.

D. Electromagnetic torque

The mechanical equation is

$$J \frac{d\Omega}{dt} = T_e - T_l - f_v \Omega \quad (41)$$

The electromagnetic torque can be obtained by the magnetic co-energy variation of the machine relative to the electrical displacement. It can be expressed [24]

$$T_e = \frac{P}{2} [i_s]^t \frac{\partial [L_{sr}]}{\partial \theta} [i_r] \quad (42)$$

p is the number of poles pairs and θ is the electrical angular displacement of the rotor.

V. SIMULATION RESULTS

The technique presented in the previous sections, has been implemented in the MATLAB environment. To illustrate performances of the proposed control, particularly at low speeds, we simulated the symmetrical and unsymmetrical operations.

A. Symmetrical operation

We simulated a loadless starting up mode with reference speed of -250 rpm; at $t = 0.5$ s, the reference speed is inverted and becomes +250 rpm, then at $t = 1$ s, nominal torque of 13.5 J/rad is applied on the shaft. At $t = 1$ sec, the rotor resistance increases of 100 %. The simulation results are shown in figure 8.

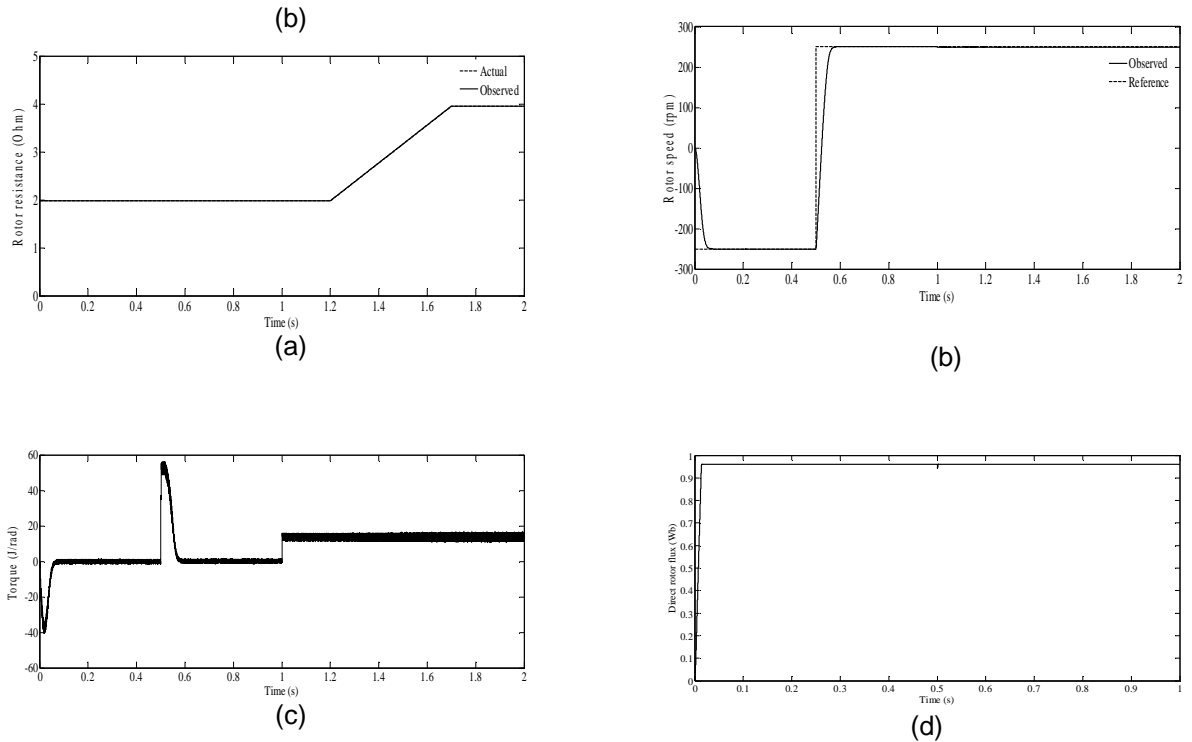
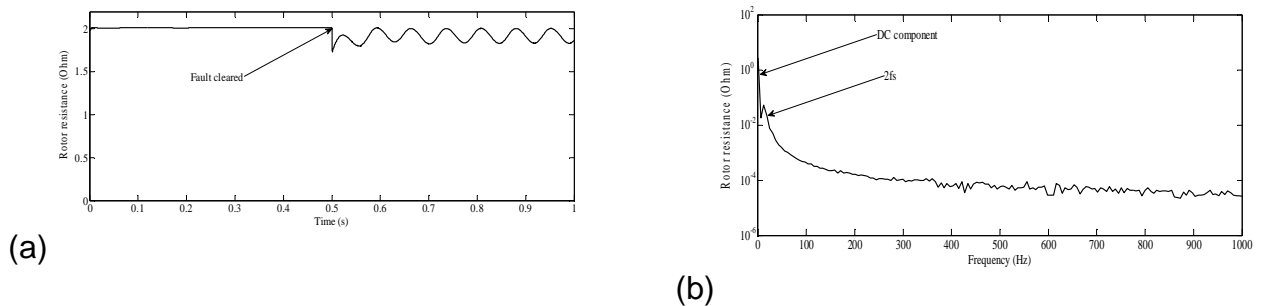


Fig. 8. Simulation results of DFOC controlled IM with rotor resistance variation: (a) rotor resistance, (b) rotor speed, (c) electromagnetic torque, and (d) direct component of rotor flux.

It is clear that the internal or external disturbances like changes in load torque, reference speed or rotor resistance variation don't allocate the performances of the proposed control. The flux tracks its reference value. The rotor speed response is also insensitive to parameters variation. Consequently, the global control scheme introduces good performances of robustness, stability and precision, particularly, under disturbance caused by parameter variation.

B. Unsymmetrical operation

We simulated a load starting up mode with a reference speed of +250 rpm. An interturn fault of 5 % is occurred on the first winding at $t = 0.5$ s. The simulation results are shown in figure 9.



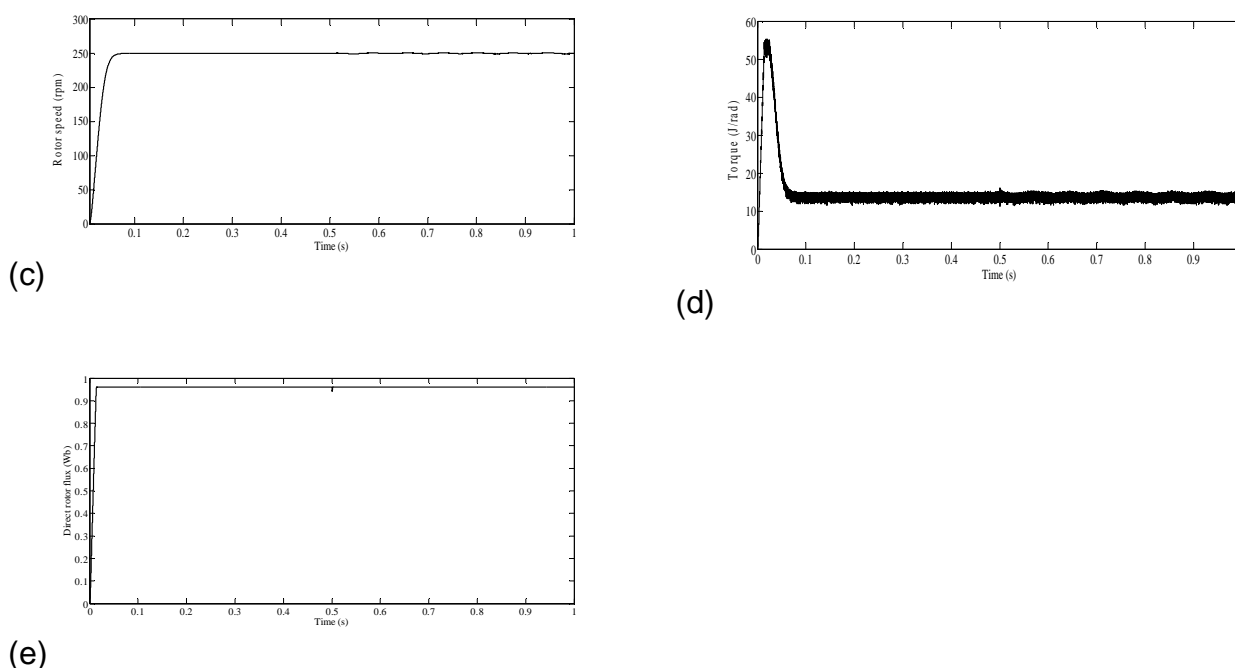


Fig. 9. Simulation results of DFOC controlled IM under stator interturn fault: (a) rotor resistance, (b) spectrum analysis of the observed rotor resistance, (c) rotor speed, (d) electromagnetic torque and, and (e) direct component of rotor flux.

For faulty condition, the rotor speed and flux still equal to their reference values. For the electromagnetic torque, pulsating component is generated to compensate the fault effect which is considered as internal disturbance. The observed rotor resistance decreases and oscillates below its nominal value with the frequency of $2f_s$. Such value of rotor resistance is considered as a fictitious quantity which only serves to superpose the Clark model to the faulty one in unsymmetrical operation.

VI. CONCLUSION

In this paper a new approach for vector fault tolerant control has been developed. For this purpose, an adaptive observer, based on the rotor resistance adaptation, has been synthesized. The estimated rotor resistance is used for the correction of the rotor time constant, decoupling terms and the controllers. At low speeds, the observed rotor resistance can be used as a very interesting tool for fault detection purpose. An on line adaptation of the rotor resistance made more robust and more stable the adaptive observer. In faulty conditions, the machine is unbalanced and significant variation of rotor resistance is produced. Using the proposed FTC, the rotor speed and flux remain equal to their reference values. On the other hand, a pulsating torque is generated. If the stator current is not exceeding the acceptable level, the machine continues to operate with degraded performances until its repair or exchange. So, it's always necessary to execute early fault detection for less damage. The obtained algorithm of the rotor resistance has the advantage to be easily implantable in a calculator. The proposed approach has well made more robust and more stable the IM based DFOC.

VII. Appendix

MACHINE PARAMETERS

Stator phase resistance	$r_s = 1.5950 \Omega$
Rotor phase resistance	$r_r = 1.3053 \Omega$
Effective air-gap	$g = 0.35 \text{ mm}$
Stack length	$L = 125 \text{ mm}$
Rotor radius	$r = 37.35 \text{ mm}$

Stator phase leakage inductance	$L_{ls} = 0.0040 \text{ H}$
Rotor phase leakage inductance	$L_{lr} = 0.0033 \text{ H}$
Drive inertia	$J = 0.045 \text{ kg.m}^2$
Friction coefficient	$f_v = 0.0038 \text{ kg.m}^2.\text{s}^{-1}$
Stator phase turns	$N_s = 124$
Rotor bar resistance	$r_b = 3.04\text{E}-4 \text{ } \Omega$
Rotor end ring segment resistance	$r_e = 8.75\text{E}-7 \text{ } \Omega$
Rotor bar leakage inductance	$l_b = 5.16\text{E}-7 \text{ H}$
End ring segment leakage inductance	$l_e = 1.59\text{E}-9 \text{ H}$

VIII. REFERENCES

1. S.G. Khalaf, A.M. Haider, "Diagnosis and fault tolerant control of the induction motors techniques a review", Australian Journal of Basic and Applied Sciences, Vol. 4, No. 2, 2010, pp. 227-242.
2. G. Stefan, M.A. Jose, L. Bin, G.H. Thomas, "A survey on testing and monitoring methods for stator insulation systems of low-voltage induction machines focusing on turns insulation problems", IEEE Transactions on Industrial Electronics, Vol. 55, No. 12, 2008, pp. 4127-4136.
3. Z. Pinjia, D. Yi, G.H. Thomas, L. Bin, "A survey of condition monitoring and protection methods for medium-voltage induction motors", IEEE Transactions on Industry Applications, Vol. 47, No. 1, 2011, pp. 34-46.
4. M.T. Rangarajan, B.L. Sang, C.S. Greg, "Gerald B.K., Jiyeon Y.A., Thomas G.H. Survey of methods for detection of stator-related faults in induction machines", IEEE Transactions on Industry Applications, Vol. 43, No. 4, 2007, pp. 920-933.
5. R. Kianinzhad, B. Nahid-Mobarkeh, F. Betin, G.A. Capolino, "Robust sensorless vector control of induction machines", Iranian Journal of Science & Technology, Transactions B, Engineering, Vol. 33, No. 2, 1994, pp. 133-147.
6. J. Ramadas, T. Thyagarajan, V. Subrahmanyam, "Robust performance of induction motor drives," International Journal of Recent Trends in Engineering, Vol. 1, No. 3, 2009, pp. 25-29.
7. S. Arfat, G.S. Yadava, S. Bhim, "A review of stator fault monitoring techniques of induction motors", IEEE Transactions on Energy Conversion, Vol. 20, No. 1, 2005, pp. 106-114.
8. O. Jasim, C. Gerada, M. Sumner, J.A. Padela, "A simplified model for induction machines with faults to aid the development of fault tolerant drives", Proceedings of the 13th International Power Electronics and Motion Control Conference, Poznan, Poland, 2008, pp. 1173-1180.
9. D. Demba, M.E. Benbouzid, A. Makouf, "A fault tolerant control architecture for induction motor drives in automotive applications", IEEE Transactions on Vehicular Technology, Vol. 53, No. 6, 2004, pp. 1847-1855.
10. J.C. Moreira, T.A. Lipo, "A new method for rotor time constant tuning in indirect field oriented control", IEEE Transactions on Power Electronics, Vol. 8, No. 4, 1993, pp. 626-631.
11. A.P. Garcia, J.L.D. Rodriguez, "Indirect field oriented control with rotor time constant adaptation", 4th International Conference on Electronics Control and Signal Processing, Florida, USA, November 17-19, 2005, pp. 169-174.
12. D.S. Reddy, K.L.P. Reddy, M.V. Kumar, "On line estimation of rotor time constant and speed of a vector controlled induction motor drives with model reference controller (MRAC)", International Journal of Engineering Research and Applications, Vol. 2, No. 6, 2012, pp. 172-179.
13. I.K. Bousserhane, A. Hazzab, "Direct field oriented control using backstepping strategy with fuzzy rotor resistance estimation for induction motor speed control", Information Technology and Control, Vol. 35, No. 4, 2006, pp. 403-411.
14. D.P. Marcetic, S.N. Vukosavić, "Speed Sensorless AC drives with the rotor time constant parameter update", IEEE Transactions on Industrial Electronics, Vol. 54, No. 5, 2007, pp. 2618-2625.
15. H. Kubota, K. Matsue, "Speed sensorless field oriented control of induction motor with rotor resistance adaptation", IEEE Transactions on Industry Applications, Vol. 30, No. 5, 1994, pp. 1219-1224.
16. D. Kouchih, M. Tadjine, M.S. Boucherit, "Adaptive observation of stator flux and resistance for fault tolerant control of induction motor drives based DTC", The Mediterranean Journal of Measurement and Control, Vol. 10, No. 1, 2014, pp. 167-175.
17. D. Kouchih, R. Hachelaf, N. Boumalha, M. Tadjine, M.S. Boucherit, "Vector fault tolerant control of induction motor drives subject to stator interturn faults", The 16th Power Electronics and Motion Control Conference and Exposition, Antalya, Turkey, September 21-24, 2014.
18. D. Kouchih, M. Tadjine, M.S. Boucherit, "Improved direct torque control of induction motors using adaptive observer and sliding mode control", Archives of Control Sciences, Vol. 23, No. 3, 2013, pp. 361-376.

19. D.G. Luenberger, "An Introduction to observers", IEEE Transactions on Automatic Control, Vol. 16, No. 6, 1971, pp. 596-602.
20. J. J. E. Slotine, W. Li, "Applied Nonlinear Control", Prentice Hall Inc., 1991, Englewood Cliffs NJ.
21. C. Edwards, S.K. Spurgeon, "Sliding mode control", theory and applications. The Taylor & Francis systems and control book series, 1998.
22. L. Xiaogang, L. Yuefeng, H.A. Toliyat, A. El-Antably, and T.A. Lipo, "Multiple coupled circuit modeling of induction machines", IEEE Transactions on Industry Applications, Vol. 31, No. 2, 1995, pp. 311-318.
23. G. Houdouin, G. Barakat, B. Dakyo, E. Destobbeleer, "A winding function theory based global method for the simulation of faulty induction machines", Proceedings of the IEEE Electric Machines and Drives Conference, Madison, Wisconsin, USA, 2003, pp. 297-303.
24. P.C. Krause, "Analysis of Electric Machinery", McGraw-Hill Book Company, 1987.

People's Democratic Republic of Algeria
Ministry of Higher Education and Scientific research
M'hamed Bougara University, Boumerdes
Institute of Electrical and Electronic Engineering,
Laboratory of Signals and Systems (LSS)



ALGERIAN JOURNAL OF SIGNALS AND SYSTEMS

ISSN : 2543-3792

Title : Sensitivity Enhancement of Methane Detection Based On Hollow Core Photonic Crystal Fiber

Authors: R.Boufenar, M. Bouamar, A.Hocini

Affiliation:(1)Laboratory analysis of signals and systems, Electronics Department, Mohamed Boudiaf University BP.166, road Ichebilia, M'sila 28000 Algeria.

(2) Nuclear research center, BP 180 Ain Oussera/Djelfa 17000/Algeria.

Page range: 23-29

IMPORTANT NOTICE

This article is a publication of the Algerian journal of Signals and Systems and is protected by the copyright agreement signed by the authors prior to its publication. This copy is sent to the author for non-commercial research and education use, including for instruction at the author's institution, sharing with colleagues and providing to institution administration. Other uses, namely reproduction and distribution, selling copies, or posting to personal, institutional or third party websites are not allowed.

Volume : 1 Issue : 1 (June 2016)

Laboratory of Signals and Systems

Address : IGEE (Ex-INELEC), Boumerdes University, Avenue de l'indépendance, 35000, Boumerdes, Algeria

Phone/Fax : 024 79 57 66

Email : lss@univ-boumerdes.dz ; ajsyssid@gmail.com

Sensitivity Enhancement of Methane Detection Based On Hollow Core Photonic Crystal Fiber

R.Boufenar^{(1), (2)*}, M. Bouamar⁽¹⁾, A.Hocini⁽¹⁾

⁽¹⁾ Laboratory analysis of signals and systems, Electronics Department, Mohamed Boudiaf University BP.166, road Ichebilia, M'sila 28000 Algeria.

⁽²⁾ Nuclear research center, BP 180 Ain Oussera/Djelfa 17000/Algeria.
Rabouf@yahoo.fr

Abstract: Monitoring methane (CH₄) concentration is essential in many industrial and environmental applications. Emission of such gases is indeed important to detect for health, safety and environmental reasons. The major risk in all these areas is an explosion hazard, which may occur if methane reaches its Lower Explosive Limit (LEL) of 5% concentration in air. For that reason, it is necessary to develop gas sensors to monitor that methane levels below this value. Due to a weak absorption of methane, this gas is difficult to detect using conventional methods. Hollow core photonic crystal fibers (HC-PBF) have emerged as a promising technology in the field of gas sensing. The strong interaction achievable with these fibers are especially advantageous for the detection of weakly absorbing regions of methane. In this paper, we investigated, by full vectorial finite element method (FV-FEM) in Rsoft CAD environment, the dependency of relative sensitivity on the fiber parameters and wavelength. Consequently, we introduced the optimal structure of an index guiding hollow core photonic crystal fiber capable of measuring methane concentrations down to 0.1% in air. The simulations showed that the sensing sensitivity increased with an increase in the core diameter and a decrease in the distance between centers of two adjacent holes.

Key Words: Photonic crystal fiber, Methane, Finite element method, Rsoft CAD.

1. INTRODUCTION

Sensing of gas species and their concentrations is widely used for process control, environmental and safety monitoring. Methane detection is extremely important for safety monitoring in chemical facilities, gas plants, landfill sites, mines and domestic environments. The major risk in all these areas is an explosion hazard, which may occur if methane reaches its Lower Explosive Limit (LEL) of 5% concentration in air. For that reason, it is necessary to develop gas sensors to monitor that methane levels below this value.

Methane shows molecular absorption lines at different regions of the infrared spectrum. In particular, weak absorption lines are present in the near infrared $\nu_2 + 2\nu_3$ band at 1.3 μm [1]. Gas sensors operating at this wavelength range benefit from the low cost light sources and detectors fully developed for telecommunication applications. However, conventional spectroscopic gas cells typically show interaction Pathlengths of few centimeters, which makes difficult the detection of methane in this region [2].

Optical gas spectroscopic systems are attractive for gas detection since they provide high spectral resolution, precise gas species identification and possibility of remote and distributed measurements [3].

Optical fibers used for gas sensing offer clear advantages such as immunity to electromagnetic interference, small size, low cost and the possibility for distributed measurements. Different fiber designs including fibers with a small hole in the center of the core [4] and D-shaped optical fibers [5] have previously been employed in gas sensing. However, such fiber sensors suffer from a poor overlap between the gas volume and the mode field of the propagating light, which results in weak absorption and therefore long length of fibers, are required.

Hollow optical waveguides have also been used but they are usually multi-mode and their losses are high, which limits the practical waveguide length to a few meters [6].

To overcome the limitation of the low sensing sensitivity, more research work needs to be done. Parameters such as sensitivity and fiber length need to be considered in detail in order to optimize a gas sensor. The Beer-Lambert law [7] gives the relationship between absorption length (fiber length), gas concentration and light intensity. In addition, in order to minimize the response time of the sensor, the fiber should be as short as possible while still long enough to provide a sufficient signal. The optimum length depends on the molecular species to be monitored and the amount of gas present in the environment.

For gases with weak absorption lines or in low concentration, an increased sensitivity can be obtained by using longer fiber length. However, the attenuation increases with the length of the fiber.

Effects limiting the sensitivity of the detection are mainly fiber loss and background noise, which is expected to result from the polarization properties and the aligning of the fiber.

An effective way to increase the sensing sensitivity is to design new structures, in which a significant fraction of the total modal power can be made to overlap with the gas.

Photonic crystal fibers (PCFs) [8] is a breakthrough in fiber optic technology, leading to unprecedented properties that overcome many limitations. In contrast with traditional optical fibers, PCFs are made of single material and have several geometric parameters that can be manipulated for larger flexibility of design.

With the modulation of the size and location of the cladding air holes, the characteristics of PCFs, such as mode shape, transmission spectrum, nonlinearity, dispersion and birefringence, could be tunable to manage the anticipated values [9].

Additionally, the existence of air holes, running along the length of the fiber, create new abilities for the appropriate interaction between light and sample through evanescent fields in the holes [10].

This enables further dynamic modification of the waveguide properties and provides perspectives for various all-in-fiber tunable or sensing devices.

In this paper, an evanescent field sensor for methane detection based on the photonic crystal fiber is introduced, in which the core consists of an air hole with dimensions smaller than the dimensions of the cladding holes to satisfy the effective index guiding criterion.

Due to the central hole, the difference between the refractive indices of the core and cladding dropped, more light would penetrate into the cladding, and thus the sensitivity increased.

The larger central hole diameter (d) showed the higher evanescent field fraction, nevertheless, the central hole diameter should be less than the cladding hole diameter (d_{cl}), to satisfy the effective index guiding Criterion.

Although due to the smaller air hole in the center, the evanescent field interaction was enhanced, but this type of PCFs had a huge confinement loss [11].

In this work we have carried out consequently, an optimal structure for simultaneously achieving more sensitivity and less confinement losses.

2. SIMULATED METHOD

Among the full vectorial methods used in modeling PCFs, the finite element method (FEM) [12] is particularly effective for handling curved interfaces with high accuracy, and it is obviously a good choice for the analysis of combined circular and elliptical shape.

In the modal solution approach based on the FV-FEM, the intricate cross section of the PCF can be accurately represented using many triangles of different shapes and sizes. This flexibility makes the FV-FEM preferable to other approaches.

In this study, we have adopted an efficient FV-FEM with PMLs to predict all the propagation characteristics of the waveguide with high accuracy.

The fiber cross-section representation is very accurate as the domain is divided into subdomains with triangular or quadrilateral shape, where any refractive index profiles can be properly represented.

Applying the variational FV-FEM procedure to Maxwell's equations, the following vector wave equation is derived [13].

$$\nabla \times ([s]^{-1} \nabla \times \vec{E}) - k_0^2 n^2 [s] \vec{E} = 0 \quad (1)$$

Where $k_0 = 2\pi/\lambda$ the free-space wavenumber, λ is the wavelength, \vec{E} denotes the electric field, n is the refractive index, $[s]$ is the PML matrix, and $[s]^{-1}$ is the inverse of the PML matrix.

When applying an FV-FEM to PCFs, a curvilinear hybrid edge/nodal element [14] is very useful for avoiding spurious solutions and for accurately modeling curved boundaries of air holes. Dividing the fiber cross section into a number of the curvilinear hybrid elements, from Eq. (1) we can obtain the following eigenvalue equations:

$$[k]\{E\} = k_0^2 n_{eff}^2 [M]\{E\} \quad (2)$$

Where $[k]$ and $[M]$ are the finite element matrices, $\{E\}$ is the discretized electric field vector consisting of the edge and nodal variables, and n_{eff} is the effective index. For an efficient calculation, we take advantage of the symmetries of the first modes in the structure by simulating only a quarter of the PCF cross section, on which we apply a suitable combination of short circuits. Moreover, with these electromagnetic short circuits, it is possible to select a family of modes with a given polarization.

3. NUMERICAL ANALYSIS

The cross-section of the analyzed fiber is shown in Fig.1. It consists of triangular lattice formed by five rings of periodic arrangement air holes.

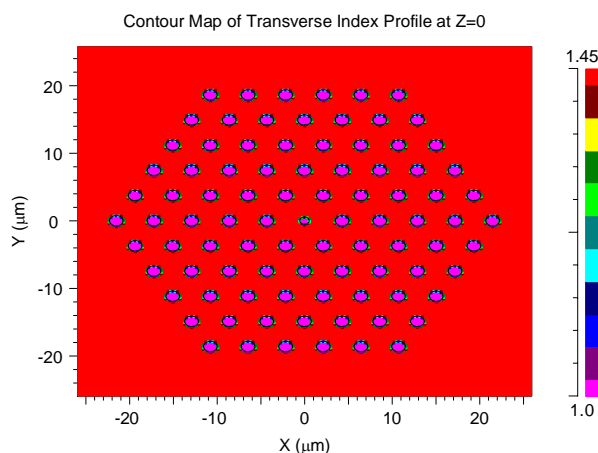


Fig.1 Cross section of the design PCF.

A small air hole is introduced in the center of PCF structure, and the diameter (d) of the defected core is smaller than the diameters of the cladding air holes. We choose two degree of freedom (d, Δ) respectively the core diameter and the distance between adjacent holes.

In the design procedure, we set the outer ring to have the same air-hole diameter (d_{cl}), to reduce fabrication complexity. Parameters (d) and (Δ) are adjusted and their influence on the sensitivity curve is investigated.

To review the proposed PCF optical properties, the finite element method (FEM) for solving Maxwell's equations was applied due to its proven reliability and high accuracy for analysing the PCF [12].

The structure of the design influences the field distribution significantly. According to the theory of the effective index [15], introduction of the air-core decreases the effective index of the fiber core. The air-core decreases the effective index of the fiber core, which leads to the weakness of the confinement effect of the cladding. As a result, the field limited in the core extends to the cladding gradually. Consequently, the modes of such fibers are inherently leaky. Moreover, we must consider that the imaginary part of its complex propagation constant represents the leakage loss of a mode.

For having an appropriate model of the leakage, an open boundary condition is required, which doesn't create reflection at the boundary. Perfectly matched layers (PMLs) are so far the most efficient absorption boundary condition for this purpose.

The confinement loss L_c , in decibels per meter is given by [16, 17]:

$$L_c = 8.686K_0 I_m [n_{eff}] \quad (3)$$

Where $I_m [n_{eff}]$ is the imaginary part of the effective index.

The evanescent field in the air holes is absorbed by the methane species, and the gas concentration can be obtained from the intensity through the Beer-Lambert law [18,20]:

$$I(\lambda) = I_0(\lambda) \exp[-r a_m(\lambda) l C] \quad (4)$$

Where I is the output light intensity in the presence of gas and I_0 refers the output light intensity without the presence of the gas.

In addition, a_m which is a function of the wavelength, is the methane absorption coefficient, l and C , respectively, denote the length of the PCF used for detection (interaction length) and C the methane concentration, and finally, r is a relative sensitivity coefficient defined as [21,22]:

$$r = \frac{n_r}{n_e} \cdot f \quad (5)$$

Where n_r refers to the refractive index of the methane, the effective refractive index of the guided mode is presented by n_e , and f is the fraction of the total power located in the holes; in the meantime, in the typical fiber, f can be calculated by [21,22]:

$$f = \frac{\int_{holes} (E_x H_y - E_y H_x) d_x d_y}{\int_{totale} (E_x H_y - E_y H_x) d_x d_y} \quad (6)$$

The transverse electric and magnetic fields of the mode are introduced by E_x, E_y and H_x, H_y respectively.

Now, with solving Maxwell's equations by utilizing a finite element method, the effective refractive index n_e and the mode field pattern, E_x, E_y and H_x, H_y can be acquired.

4. RESULTS and DISCUSSION

First, we have simulated the structure of the design PCF, the confinement loss was calculated at different wavelengths using the FEM based software (FemSim). Here we interested in the wavelength range from $0.8 \mu m$ to $2 \mu m$. This range is within the low loss window of silica fiber and covers the absorption lines of the methane in the near infrared region.

Figure 2 shows the calculated confinement loss versus wavelength by changing the dimensions of the central hole. By decreasing, the diameter of the central hole from $2 \mu m$ to $1.2 \mu m$, the confinement loss will reduce because the difference of core and cladding indices is high, and consequently, more light power can be confined in the core region.

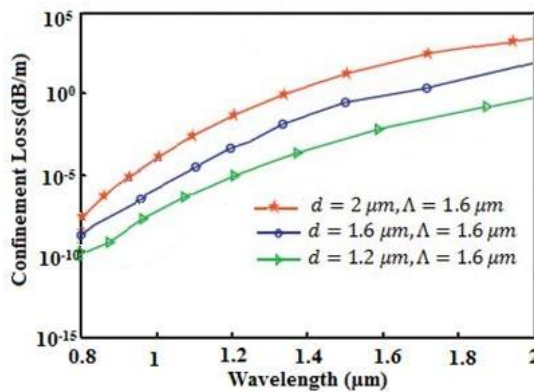


Fig.2 Confinement loss versus wavelength for different core diameters.

Generally, overlaps are quite poor for small holes. Better penetration into the holes is obtained for longer wavelengths and larger core size.

The loss plotted is for a five-ring cladding, and can naturally be reduced by adding more holes. There is huge flexibility in adjusting the sizes, shapes and positions of the microstructure holes to optimize performance. So far, we have looked at five ring structures for all designs. This allows for fast calculation, and puts all designs on an equal footing for fair comparisons of confinement loss. Once a suitable five-ring design is obtained, one can easily achieve a desirable confinement loss level (with negligible change in the basic mode structure) by adding more holes to the cladding. These results demonstrate a nearly ideal single mode waveguide for methane detection: The fiber combines almost complete overlap of light with the gas with acceptable loss over long interaction lengths.

The well-shaped mode fields, robust confinement mechanism and relatively large core size present further advantages for achieving more sensitivity.

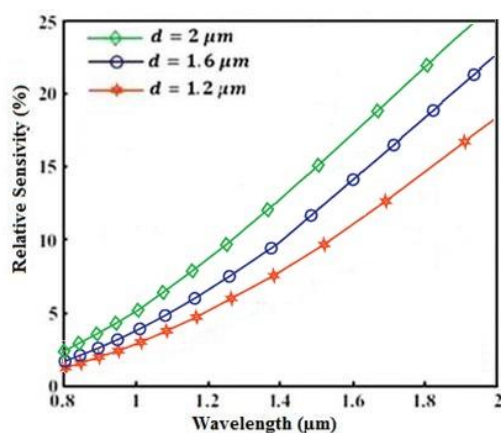


Fig.3Relative sensitivity versus wavelength for different core diameter.

Figure 3 shows the calculated relative sensitivity for the proposed PCF with varying the core diameter.

The relative sensitivity increases with increasing the core diameter because more evanescent field fraction spreads to the cladding holes and interacts with samples.

The sensitivity increases with an increase in the wavelength because the light can penetrate into the cladding holes by increasing the wavelength.

Figure 4 reviews the same basic trends, the calculated relative sensitivity for the proposed PCF with varying the distance (\square) between adjacent holes, with a reduction in (\square) from $2.4 \mu\text{m}$ to $1.6 \mu\text{m}$, the relative sensitivity increases because the cladding index reduces by a reduction in (\square), and so more light enters the cladding.

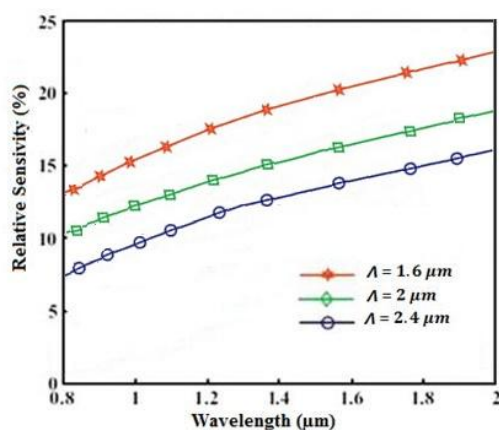


Fig.4 Relative sensitivity versus wavelength for different pitch.

5. CONCLUSION

We have analyzed and demonstrated an evanescent wave absorption sensor for methane detection using a short length of pure silica hollow core PCF.

The proposed sensor architecture is significantly simpler than other structures for controlling the sensitivity.

The design procedure for this proposed sensor structure could be more efficient and easier because relatively fewer geometrical parameters are need to be optimized. Thus, we can choose the appropriate geometric parameters to achieve the desirable sensitivity.

The relationship between the sensing properties of index guided PCF with air core and the fiber parameters, as well as the fiber length and operating wavelength, has been numerically investigated.

The sensitivity of the modified fibers depends on the penetration of the transmitted power into the fiber holes and can be controlled by controlling core and holes dimensions.

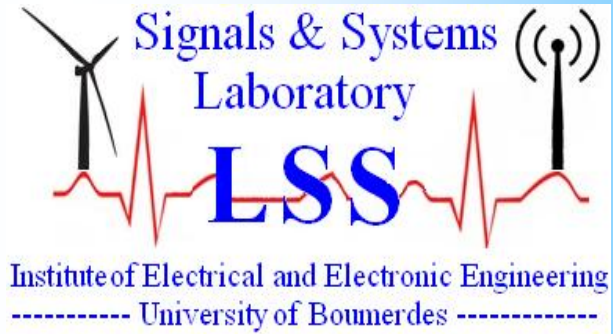
The relative sensitivity at wavelength of $\lambda = 1.33 \mu\text{m}$ that is in the Methane absorption line is enhanced. The confinement loss is also improved.

References

- [1] L. S. Rothman, D. Jacquemart, A. Barbe, D. Chris Benner, M. Birk, L. R. Brown, M. R. Carleer, C. Chackerian, Jr., K. Chance, L. H. Coudert, V. Dana, V. M. Devi, J.-M. Flaud, R. R. Gamache, A. Goldman, J.-M. Hartmann, K. W. Jucks, A. G. Maki, J.-Y. Mandin, S. T. Massie, J. Orphal, A. Perrin, C. P. Rinsland, M. A. H. Smith, J. Tennyson, R. N. Tolchenov, R. A. Toth, J. Vander Auwera, P. Varanasi, and G. Wagner, "The HITRAN 2004 molecular spectroscopic database," *J. Quant. Spectrosc. Radiat. Transfer*. Vol. 96, pp.139–204, 2005.
- [2] K. Noda, M. Takahashi, R. Ohba and S. Kakuma, "Measurement of methane gas concentration by detecting absorption at 1300 nm using a laser diode wavelength-sweep technique," *Opt. Eng.* Vol.44, 014301, 2005.
- [3] Lopez-Higuera, J. M., "Handbook of Optical Fibre Sensing Technology", Ed. John Wiley & Sons, 2002.
- [4] S. Sudo, I. Yokohama, H Yasaka, Y. Sakai, and T. Ikegami, "Optical fiber with sharp optical absorption by vibrational-rotational absorption of C₂H₂ molecules," *IEEE Photonics Technol. Lett.* Vol.2, pp. 128-131, 1990.
- [5] W. Jin, G. Stewart, and B. Culshaw, "Prospects for fibre optic evanescent field gas sensors using absorption in the near-infrared," *Sens. and Act.* Vol. 38, Issues 1-3, pp. 42-47, 1997.
- [6] J. Harrington, "A review of IR transmitting hollow waveguides," *Fiber Integr. Opt.* Vol.19, pp. 211–227, 2000.
- [7] G. Stewart, J. Norris, D.F.Clark, et al., "Evanescent-wave chemical sensors a theoretical evaluation," *International Journal of Optoelectronics*, 6, pp. 227-238, 1991.
- [8] Philip St.J. Russell "Photonic-Crystal Fibers" *J. Lightwave Technol.* Vol. 24, Issue 12, pp. 4729-4749, 2006.
- [9] Shuguang Li, Xiaoxia Zhang, and Govind P. Agrawal "Characteristics of photonic crystal fibers designed with an annular core using a single material" *Applied Optics*, Vol. 52, Issue 13, pp. 3088-3093, 2013.

- [10] W. Jin, H.L. Ho, Y.C. Cao, J. Ju, L.F. Qi "Gas detection with micro and nano-engineered optical fibers" *Optical Fiber Technology*, Vol. 19, Issue 6, Part B, pp. 741–759 December 2013.
- [11] Saeed OLYAEE, Hassan ARMAN "Improved gas sensor with air-core photonic bandgap fiber" *Frontiers of Optoelectronics*, Vol. 8, Issue 3, pp. 314-318, September 2015.
- [12] F. Brechet, J. Marcou, D. Pagnoux, and P. Roy, "Complete analysis of the characteristics of propagation into photonic crystal fibers, by the finite element method," *Optical Fiber Technology*, Vol. 6, Issue 2, pp.181–191, 2000.
- [13] K. Saitoh, M. Koshiba, "Full-vectorial imaginary-distance beam propagation method based on a finite element scheme: application to photonic crystal fibers," *IEEE J. Quantum Electron.* Vol.38, Issue 7, pp.927-933, 2002.
- [14] M. Koshiba, Y. Tsuji, "Curvilinear hybrid edge/nodal elements with triangular shape for guided-wave problems," *J. Lightwave Technol.* Vol.18, Issue 5, pp. 737-743, 2000.
- [15] Jingyuan Wang, Chun Jiang, Weisheng Hu, Mingyi Gao "Properties of index-guided PCF with air-core" [Optics & Laser Technology, Vol.39, Issue 2](#), pp. 317-321, March 2007.
- [16] HuseyinAdemgil and ShyqyriHaxha "PCF Based Sensor with High Sensitivity, High Birefringence and Low Confinement Losses for Liquid Analyte Sensing Applications" *Sensors*, Vol. 15(12), 31833-31842, 2015.
- [17] Md. Mahbub Hossain and Md. Maniruzzaman "Study of Confinement Loss in Photonic Crystal Fiber" proceedings International Conference on Materials, Electronics & Information Engineering, ICMEIE-2015.
- [18] Benchong Li, Jun Lou, Hongzhi Xu, Jie Huang, Ben Xu, Weimin Shen "Numerical investigation of photonic crystal fiber sensor sensitivity based on evanescent wave absorption" *Proc. SPIE 9274, Advanced Sensor Systems and Applications VI*, 92741V, November 2014.
- [19] Dong-Lin Tang, Shan He, Bing Dai, Xia-Hui Tang "Detection H2S mixed with natural gas using hollow-core photonic bandgap fiber" *Optik*, Vol.125, pp. 2547–2549, 2014.
- [20] MonirMorshed, Sayed Asaduzzaman, Md. Faizul Hug Arif and Kawsar Ahmed "Proposal of Simple Gas Sensor Based on Micro Structure Optical Fiber" 2nd Int. Conf. on [Electrical Engineering and Information Communication Technology \(ICEEICT\) 2015](#).
- [21] HuseyinAdemgil "Highly sensitive octagonal photonic crystal fiber based sensor" [Optik, Vol.125, Issue 20](#), pp. 6274-6278, October 2014.
- [22] Monir MORSHED, Md. Imran HASAN, and S. M. Abdur RAZZAK "Enhancement of the Sensitivity of Gas Sensor Based on Microstructure Optical Fiber" [Photonic Sensors](#), Vol.5, [Issue 4](#), pp. 312-320, December2015.

People's Democratic Republic of Algeria
Ministry of Higher Education and Scientific research
M'hamed Bougara University, Boumerdes
Institute of Electrical and Electronic Engineering,
Laboratory of Signals and Systems (LSS)



ALGERIAN JOURNAL OF SIGNALS AND SYSTEMS

ISSN : 2543-3792

Title : **Photovoltaic effect in Light Emitting Diodes**

Authors: **K. Remidi, A. Cheknane, M. Haddadi**

Affiliation : (1) **Dept de Physique école normale supérieure (ENS) Kouba 16050 Algiers Algeria.**

(2) **Laboratoire des Semiconducteurs et Matériaux Fonctionnels. Université Amar Telidji de Laghouat. Bd des Martyrs. BP37G Laghouat-03000-Algérie**

(3) **Dept d'électronique école nationale polytechnique (ENP) d'El-Harrach Algiers Algeria**

Page range: **30-36**

IMPORTANT NOTICE

This article is a publication of the Algerian journal of Signals and Systems and is protected by the copyright agreement signed by the authors prior to its publication. This copy is sent to the author for non-commercial research and education use, including for instruction at the author's institution, sharing with colleagues and providing to institution administration. Other uses, namely reproduction and distribution, selling copies, or posting to personal, institutional or third party websites are not allowed.

Volume : 1 Issue : 1 (June 2016)

Laboratory of Signals and Systems

Address : IGEE (Ex-INELEC), Boumerdes University, Avenue de l'indépendance, 35000, Boumerdes, Algeria

Phone/Fax : 024 79 57 66

Email : lss@univ-boumerdes.dz ; ajsyssig@gmail.com

Photovoltaic effect in Light Emitting Diodes

K. Remidi (1)*, A. Cheknane (2), M. Haddadi (3)

- (1) Dept de Physique école normale supérieure (ENS) Kouba 16050 Algiers Algeria
(2) Laboratoire des Semiconducteurs et Matériaux Fonctionnels. Université Amar Telidji de Laghouat. Bd des Martyrs. BP37G Laghouat-03000-Algérie
(3) Dept d'électronique école nationale polytechnique (ENP) d'El-Harrach Algiers Algeria
* remidi@ens-kouba.dz, remidi_kam@yahoo.fr

Abstract: This paper describes an experimental work on the electrical characterization of commercial LED of different colors and their photoelectric effect.

A research work has been carried out to develop the experimental measurement in order to show the presence of a photovoltaic effect on LEDs. For this purpose, we measured the electrical characteristics of individual LED and studied their light intensities using a pyranometer EPLEY. This work focused mainly on red, green and yellow LEDs. Moreover, we have implemented an experimental system for the measurement of sensitivity of different LEDs depending on the power of light from a light source. A comparison was made between theoretical model and experimental results.

Keywords: LEDs; Photovoltaic; effect; Characterization; light intensity.

1. INTRODUCTION

It was not until 1962 that the first red LED was created by Nick Holon yak Jr and S. Bevacqua. For several years, researchers have been limited to a few colors such as red (1962), yellow and blue (1972) [1, 2] .or green. Conventional low power LEDs are an attractive alternative in comparison to conventional products such as fluorescent lights, incandescent or discharge. They offer such a great advantage which is low power consumption, long life time and the ability to select a very specific color among many others.

In recent years LEDs are widely implemented and used in our daily life. They have a huge advantage over other types of lighting: the photon creation process of a LED is extremely effective; indeed in one LED each electron gives a photon. Thus, with a current of one ampere, a light output gives about one Watt, whereas a bulb will give only 0.1W for the same current. The more widespread use of LEDs for lighting will have an extremely important impact on the energy savings and the environment. The LED performance doubling every 3 years for the price divided by 10 every ten years [3] . At present, they are widely used in illumination and indication, billboards, traffic lights and flat panel televisions. The widespread use of these devices in both the domestic and external lighting would make substantial energy saving. However, this development raises a number of measurement problems for both aspects of characterization of lighting equipment for the security-related problems in the use of these sources. The light emitting diodes are sources of very small dimensions emitting a large flow in a solid angle reduced.

At the international level, in particular the International Commission on Illumination (CIE), several technical committees have carried out research work on different aspects of these measurements [4].

Concerning the photovoltaic effect, some research work has been done regarding this aspect; this is due to the fact that LEDs are made of a PN junction which is not opaque, the photons may reach and thereby produce a photovoltaic effect, like in the junctions case of a conventional solar cell.

This same effect can probably be observed in organic LEDs (OLEDs) according to the process described by Karzazi ([5],

It is the fact that LEDs were not suitable for this function: the hood probably suffers no antireflection coating. However, it is not quite certain that this effect exists.

2. II MATERIALS AND METHODS

A. Electrical Characterisation of conventional LEDs of different colors

Bench block diagram is shown in Figure 1 [6], temperature was controlled by the bench and the outside temperature of the LED assembly.

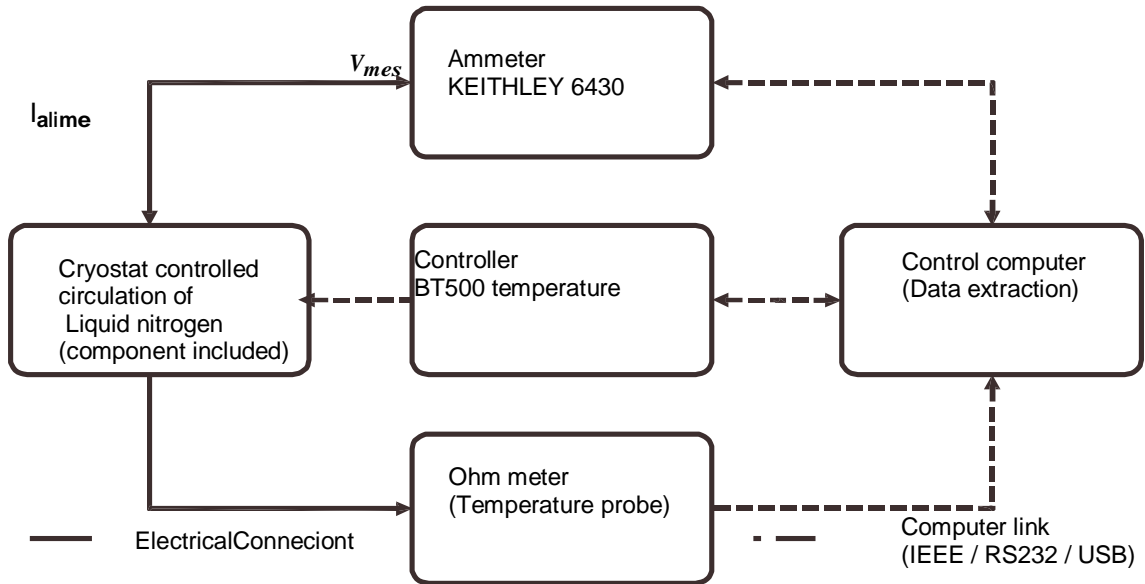


Fig.1: Schematic diagram of the bench $I = f(V)$

The equipment used consists of:

- 1- Analyzer semiconductor parameters KEITHLEY 6430 connected by an IEEE bus connected to the CPU of the control computer. This device consists of a current source (10^{-16} A to 0.1 A) 10^{-17} A resolution (error 0.1%) and a voltage source (0 to 10 V) resolution 10^{-6} V (error 0.1%) ;
 - 2- Liquid nitrogen flow cryostat LN2 is controlled where in the component. It allows temperature regulation in a range of 80 K to 350 K with a precision of 0.1 K;
 - 3- Temperature control unit (Temperature Controller BT 500) used for temperature regulation during measurements. It controls the heating resistor of the cryostat using a PID automatic system (Proportional Integral Derivative);
 - 4- Drypump (ADIXEN) whose role is to conduct a primary vacuum (1: -2 Torr) in the vacuum chamber of the cryostat;
 - 5- Ohmmeter giving a resistance value denoted R_{sonde} , corresponding to the value of the resistance of the PT100 heat sensor. This probe provides access to the TP package temperature of the LED;
- To overcome the resistance of electrical cables, the LED is connected in measure 4 son with Triaxcables (Keithley) [7, 8].

B. PV different LED Effect:

The measuring device is based on a pyranometer device which measures the luminance in W / m^2 and which is disposed in the same plane as the LED under test. We choose the correct orientation of the LED for maximum current flow at its terminals. Several measures will be taken (twenty) one day. The coefficient of the pyranometer is:

$$C = 9,56 \times 10^{-6} V / (W / m^2)$$

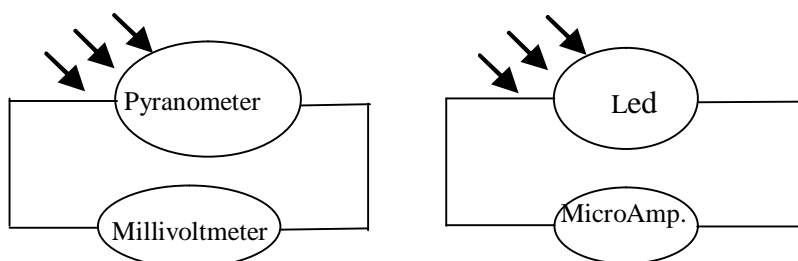


Figure 2: Diagram of the light measuring device according to the current of the LED $V_p=f(I_d)$

C. Measurement of the sensitivity of various green LEDs, yellow and red according to the power of the illumination source.

The used equipment :

- 1- A stabilized voltage supply $V = 12V$ and a current $I = 4A$ for the operation of the lamp
- 2- A light meter to measure the luminance
- 3- A digital multimeter used in ammeter to measure the current across the yellow and red LED according to the power of illumination of a light source.

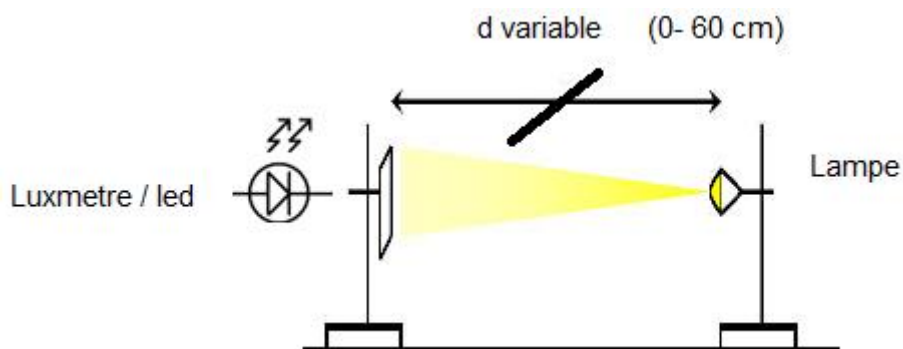


Fig. 3 measuring device Scheme E $(v) =f(I_d \text{ LED})$

3. RESULTS AND DISCUSSION

A. Current -voltage characteristic of a classic red LED

The current-voltage characteristic of a conventional LED is given in Figure 4. The first drawn in linear scale shows a threshold voltage V_s between two main areas: B where the diode is conducting ($V > V_s$) and where A diode is blocked ($V < V_s$). The behavior is the one of a diode. This plot is ideal for high injection levels ($V > V_s$). The characteristic $I(V)$ characteristic of a red LED is shown in

Figure 4. Feature red LED directly.

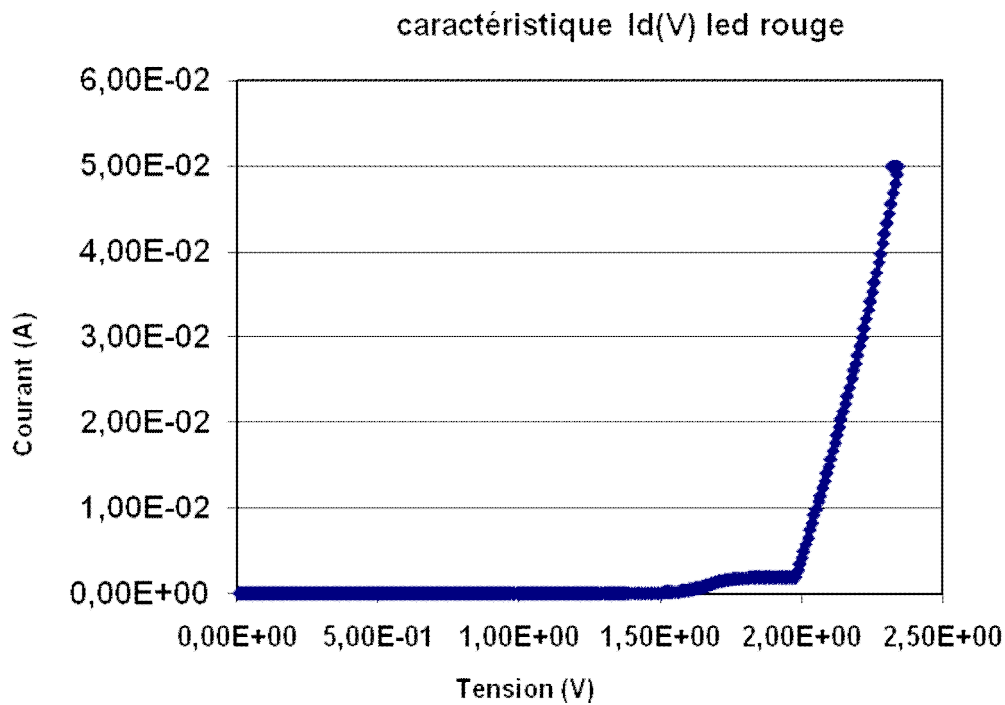


Fig 4 Characteristic $I = f(V)$ obtained from a red LED in direct

The second figure $\log I (V)$, complementary to the firestone four distinct current injection regions: possesses

$$\log (I) = f(V)$$

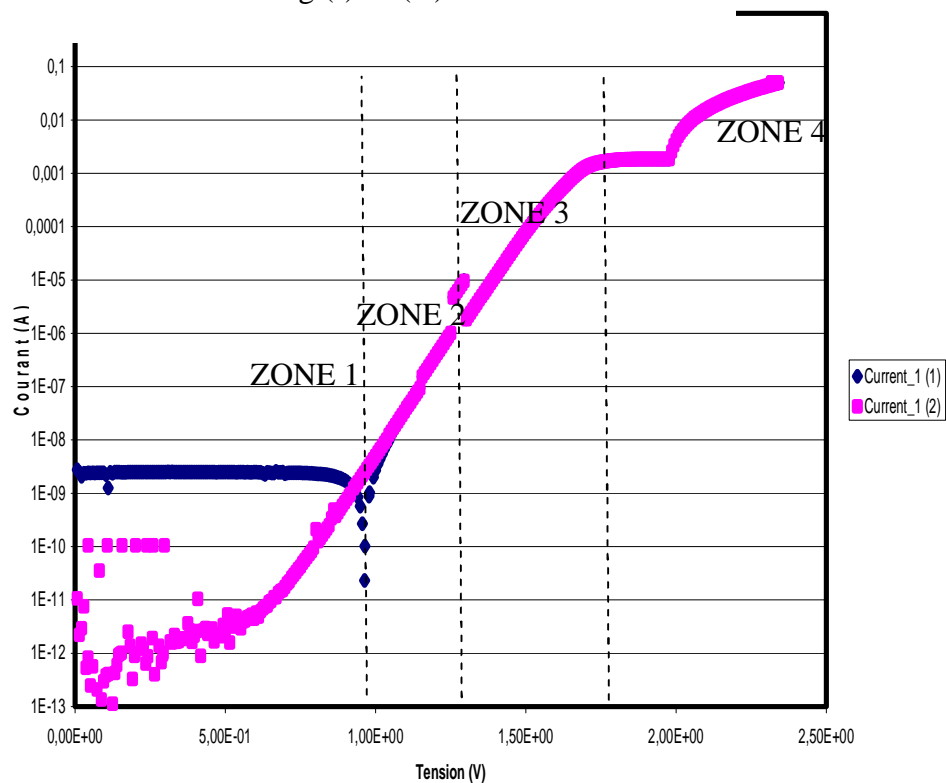


Fig. 5 Characteristic $I (V)$ characteristic of a red LED in opposite

The second figure log I (V), complementary to the firestone possesses four distinct current injection regions:

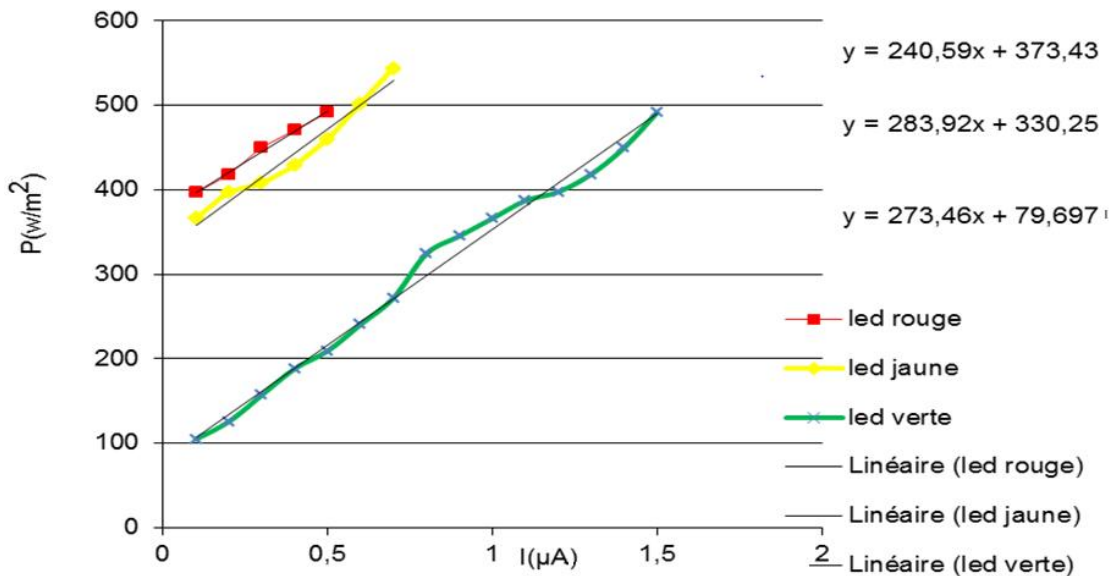
- * Very low injection level (Zone I): $I \leq 100 \text{ nA}$;
- * Low level of injection (Zone II): $100 \text{ nA} \leq I \leq 1 \mu\text{A}$;
- * Middle injection level (Zone III): $1 \mu\text{A} \leq I \leq 3 \text{ mA}$;
- * Fort injection level (Zone IV): $I \geq 3 \text{ mA}$;

This plot is very well suited to low injection levels ($V < V_s$). It is noted that the development of the models will following the route I (V) or log I (V), depending on the injection levels. The objective of this part is to remember the analytical model, well known, transport phenomena in the four areas of operation on a

B. Power of a classic red del Models.

Photovoltaic effect of different LED:

$C = 9,56 \times 10^{-6} \text{ V} / (\text{W} / \text{m}^2)$ this coefficient allows us to transform the voltage (v) across the pyranometer in light intensity (W / m^2) Table light intensity depending on the current through the various LEDs.



This graph shows a photovoltaic effect of these LEDs and we see that the green LED ($79 \text{ w} / \text{m}^2$) is more sensitive after then the yellow ($330 \text{ w} / \text{m}^2$) and the red ($373 \text{ w} / \text{m}^2$) the least sensitive and

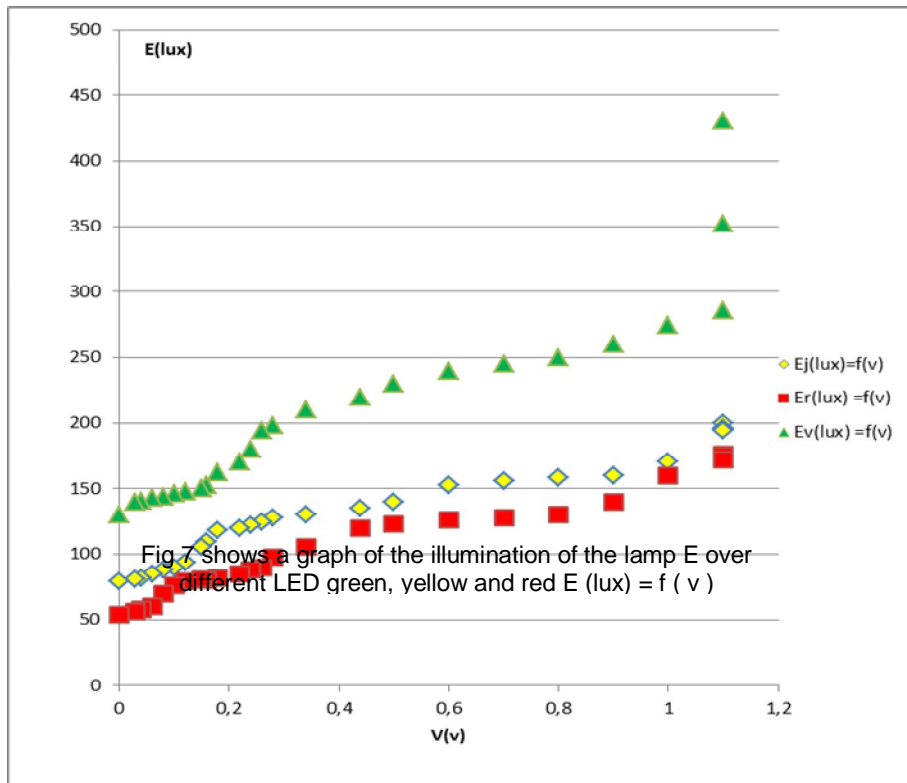
that the curve is linear for all the led's $P = A i d + b$ with $A = \frac{Dp}{Di}$

slope of the graph and b: light power when the current $I = 0$

C. Measuring the sensitivity of the different LED green, yellow and red depending on the power of the illumination of the light source (lamp).

It illuminates a light meter is a hundred centimeter distance. It simultaneously measures the light intensity, which passes through the LED and the voltage across the light meter. When the distance vary from zero to sixty centimeter between first the LED lamp powered by a DC voltage generator and for a second time between the illumination and the illuminated lamp, measuring each time the voltage across the LED with a precision digital multimeter and lamp illumination with a light meter. Figure 8 shows the following results in table form

This graph shows that illumination is quasi proportional to the terminal voltage of these different leds ,the goal of this experiment is to show that there is an effect of the lampe light on these most leds and that the same tension of the led illumination is different and that the green led is sensitive, then the yellow, the least sensitive is the red.The absolute values given by the luxmeter are not considered right strictly speaking



Indeed, the photometric head of the luxmeter recovers all the luminous flow contained in the half spaces and thus the one reflected by the objects of the part, or sent by the lamps of the ceiling light of the room if those were not extinct during the experiment. These elements will tend to modify the values of illumination really due to the LED

Moreover, the lux-meter is not calibrated. The photometric head generates errors which can be about 20% if the real filter of the photometric head is very different from the curve of sensitivity of the human eye $V(\lambda)$. Generally the luxmeter are gauged compared to one illuminating A which has a spectrum in the visible well-known one. The LED have a completely different spectra , the interaction with the shape of the filter can cause important errors on the values of illumination

We described in this work three principal experiments on the electric characterization of commercial light-emitting diodes of various colors and their photoelectric effect

The measures were voluntarily taken under real conditions of use

The First graph (V) of the characteristic voltage into direct of a classical led, in linear scale (Figure 4), it is possible to extract two functional parameters corresponding to the mode from strong level of injection: The tension of V_s threshold (X-coordinate in the beginning) and resistance series R_s (opposite of the slope). The tension of threshold is related to the tension of V_d diffusion. V_s separating two principal zones: B where the diode is busy ($V > V_s$) and A where the diode is blocked ($V < V_s$). The behavior is well that of a diode. This layout is adapted perfectly to the strong levels of injection ($V \geq V_s$).

For a polarization in tension $V \geq V_s$, the system always does not allow the transportation by diffusion. Only the recombination in the active zone is possible. The zones of containment have the role of barrier of potential. The limitation of the current is due only to the equivalent resistance of the

various layers constituting the chip. The Following equation 1 models the V_d tension at the boundaries of the del.

$$V_d = V_s + R_s I_d \quad (1)$$

V_s tension off seuil on (V) of the led

I_d current direct on (ma)of the led

I (V), complementary the second layout log to the first, distinguishes four modes from injection of current adapted to the low levels of injections ($V < V_s$).

IV-CONCLUSION:

This work allowed us to underscore the feasibility of using leds in photo detector The current photo armature induced is about 100 Na and we are very optimist forthe future results of this research. The industrial repercussions are also very important. Currently, the integration of new features in a solar candelabrum is one of the industrial priorities. One of the research activities is to develop new features within this device.

The obtained results will validate our hypotheses, which was already established, they will also make it possible to appreciate the potentialities of the LED in the photovoltaic field and to examine the niches in which they would be likely to be integrated. We had already retained of them one which is in the field as of sensors of sunning

This second work allowed us to set up means of measurement to show that there is a photovoltaic effect on the leds in ENP "El Harrach"(polytechnic school of Algiers). For this we measured the electric characteristics of various LED and studied their luminous intensities using a pyranometer EPLEY

And with the ENS of Kouba we used a device of measurement that measures the sensitivity of different leds according to the power of illumination from a source of light.

References

- [1] Neel V. Patel: "Nobel Shocker: RCA Had the First Blue LED in 1972"; 7 oct2014
- [2] C. Noah Photobiomodulation dermatology: Understanding and using LED, John Libbey Eurotext - Doin, coll. "Lasers and related technologies," 2014
- [3] (In) "Haitz law": Nature Photonics Technology Focus on LEDs volume 1; 2007
- [4] W. V.CIE 127:2007 The following members of the TC 2-45.... Report is a revision of CIE 127-1997 (Measurement of LEDs) and supersedes 27 mai 2011.
- [5] Karzazi Y., Organic Light Emitting Diodes: Devices and Applications, J. Mater. Env. Sci. 5 (1) (2014) 1-12.
- [6] Raphaël Baillot ; Thesis presented by the university of bordeaux doctoralphysical science and engineering « deffailance pour l'évaluation de la fiabilité de diesélectroluminescentes » ; 21 Novembre 2011
- [7] J J. Singleton, "Band theory and electronic properties of solids" ; Oxford University Press, 2001.
- [8] J. R. Barnes, "Robust electronic design reference book vol. 1" Springer, 2004

People's Democratic Republic of Algeria
Ministry of Higher Education and Scientific research
M'hamed Bougara University, Boumerdes
Institute of Electrical and Electronic Engineering,
Laboratory of Signals and Systems (LSS)



ALGERIAN JOURNAL OF SIGNALS AND SYSTEMS

ISSN : 2543-3792

Title : A Combined Sliding Mode Space vector Modulation Control of the Shunt Active Power Filter Using Robust Harmonic Extraction Method

Authors: A. Dahdouh, S. Barkat, A. Chouder

Affiliation: Electrical Engineering. Mohamed Boudiaf-M'sila University, M'sila, Algeria

Page range: 37- 46

IMPORTANT NOTICE

This article is a publication of the Algerian journal of Signals and Systems and is protected by the copyright agreement signed by the authors prior to its publication. This copy is sent to the author for non-commercial research and education use, including for instruction at the author's institution, sharing with colleagues and providing to institution administration. Other uses, namely reproduction and distribution, selling copies, or posting to personal, institutional or third party websites are not allowed.

Volume : 1 Issue : 1 (June 2016)

Laboratory of Signals and Systems

Address : IGEE (Ex-INELEC), Boumerdes University, Avenue de l'indépendance, 35000, Boumerdes, Algeria

Phone/Fax : 024 79 57 66

Email : lss@univ-boumerdes.dz ; ajsyssid@gmail.com

A Combined Sliding Mode Space vector Modulation Control of the Shunt Active Power Filter Using Robust Harmonic Extraction Method

ADEL DAHDOUH^{(1)*}, SAID BARKAT⁽²⁾, AISSA CHOUDER⁽³⁾

^{(1), (2), (3)} Electrical Engineering. Mohamed Boudiaf-M'sila University, M'sila, Algeria
dahdouh.adel@univ-msila.dz

Abstract: This paper presents a combined sliding mode space vector modulation control of the shunt active power filter using robust harmonic extraction method to improve the power quality such as current harmonics and reactive power compensation due to the non-linear loads and unbalanced voltage source. To verify the validity of the analysis and the feasibility of the proposed control method a set of simulation tests have been conducted using Matlab/Simulink. A comparison between the conventional instantaneous powers method (PQ) used for harmonic extracting and the new PQ based on a multivariable extraction filter demonstrates the superiority of the proposed control scheme.

Keywords: Shunt Active Power Filter (SHAPF), Multivariable Filter (MVF), Space vector Modulation (SVM), Sliding Mode controller (SMC).

1. INTRODUCTION

In recent years, the increasing use of power electronic devices has led to the deterioration of power quality due to harmonic generations [1]. The terminology and the guidelines for power quality have been described in detail at IEEE-519 and IEC-555. According to these guidelines, the allowed total harmonic distortion should be less than 5% [2].

The aforementioned problems are partially solved with the help of passive filters [3-5]. However, this kind of filter cannot solve random variations in the load current waveform and voltage waveform. On the other hand, active filters such as Static Var Compensator (SVC), Shunt Active Power Filter (SHAPF), Series Active Power Filter (SAPF), and hybrid filters are proposed to ensure power quality [6].

SHAPFs are typically used for the elimination of current harmonics, for reactive power compensation, and in balancing unbalanced current. As current harmonics are included in the system under consideration, shunt active filters are connected to the load side [7,8]. To remove harmonics and the reactive components of nonlinear loads, these filters act as sources injecting different compensation currents whose harmonic and reactive components have equal amplitude but a phase difference of 180°. Moreover, these filters are often used as static generators to balance voltage profiles and improve voltage [9].

Different control approaches for the SHAPF have been proposed. In [10] authors have applied a linear control using PI controller. The control of the SHAPF connected to a Wind system by PI controller is proposed in [11]. An intelligent controller has been applied by [12] and [13]. A four wire topology of the SHAPF has been studied in [14], [15] and [16].

The aim of this paper is twofold. Firstly to design a sliding mode controller combined with space vector modulation for the SHAPF to enhance power quality. Secondly, to compare the performances of the proposed robust harmonic extraction method with the conventional instantaneous powers method (PQ theory) to validate the proposed control scheme, through an extensive simulation results for a passive load connected through an uncontrolled bridge rectifier.

The rest of the paper is organized as follows: in section II, the control design of the SHAPF is presented, while in section III, simulation results and their discussion are given, finally a conclusion of the present work is derived.

2. CONTROL DESIGN

The basic operation of the proposed control method associated to a nonlinear load is shown in Fig. 1. The switch control signals are derived from a Space Vector Modulator (SVM). Voltage references for the SVM are derived from the sliding mode controllers. The references are computed by using the instantaneous PQ theory [17-19]. The compensation objective is to compensate current harmonics, reactive power, and to regulate the DC bus voltage. Detailed description of different parts of SHAPF is given hereafter.

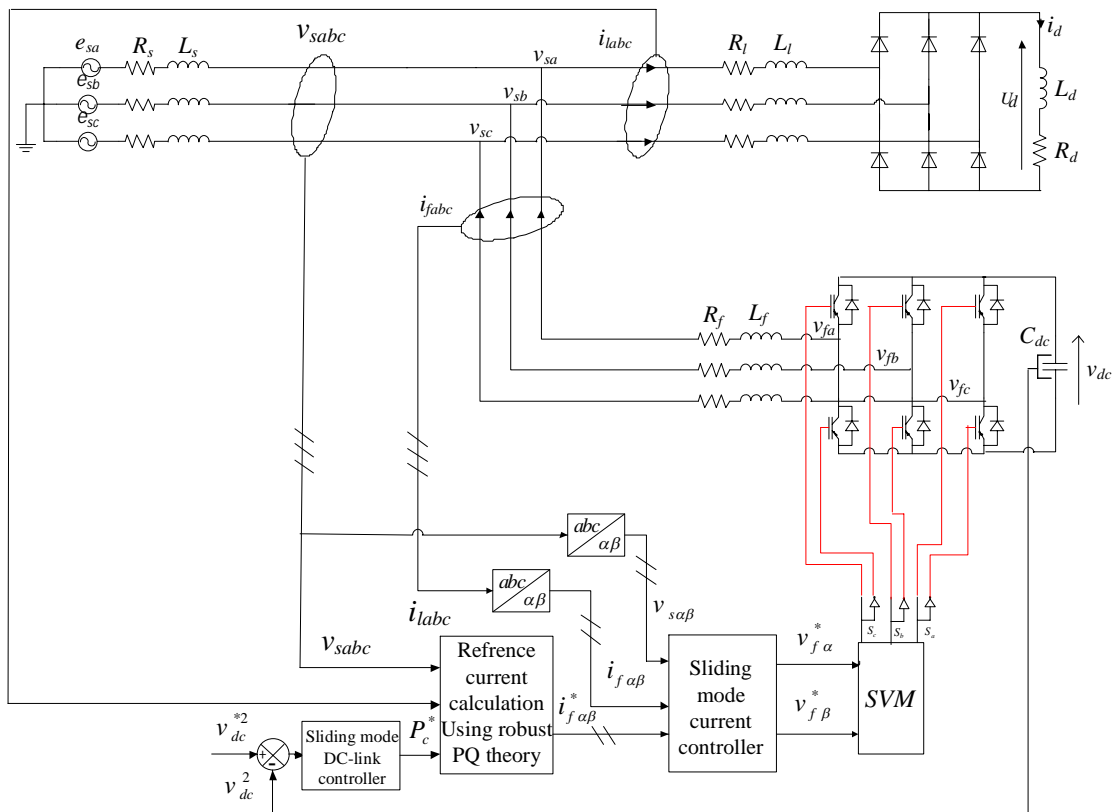


Fig. 1. Sliding mode control scheme of the SHAPF.

Mathematical Model of SHAPF

The differential equations describing the dynamic model of SHAPF are defined in stationary α - β reference frame.

The SHAPF's model is governed by the following equation.

$$\dot{x} = f(x) + g(x)u \tag{1}$$

where:

$$f(x) = \begin{bmatrix} -\frac{R_f}{L_f} i_{f\alpha} - \frac{v_{s\alpha}}{L_f} \\ -\frac{R_f}{L_f} i_{f\beta} - \frac{v_{s\beta}}{L_f} \end{bmatrix}, g(x) = \begin{bmatrix} \frac{1}{L_f} & 0 \\ 0 & \frac{1}{L_f} \end{bmatrix}, x = \begin{bmatrix} i_{f\alpha} \\ i_{f\beta} \end{bmatrix}, u = \begin{bmatrix} v_{f\alpha} \\ v_{f\beta} \end{bmatrix}$$

and $v_{s\alpha\beta}$ are the voltages of the source in the α - β coordinates, $i_{f\alpha\beta}$ and $v_{f\alpha\beta}$ are the α - β axis currents of the filter.

Harmonic extraction

Active filter depends greatly on the extraction method used to eliminate harmonics from the distorted waveforms [10], [19]. Hereafter, harmonics extraction methods are described.

A. Harmonic currents extraction using conventional PQ theory

The algorithm of the instantaneous powers theory is highlighted in Fig. 2.

Instantaneous active and reactive powers of the nonlinear load are calculated by:

$$\begin{bmatrix} P_l \\ Q_l \end{bmatrix} = \begin{bmatrix} v_{s\alpha} & v_{s\beta} \\ v_{s\beta} & -v_{s\alpha} \end{bmatrix} \begin{bmatrix} i_{l\alpha} \\ i_{l\beta} \end{bmatrix} \quad (2)$$

Where the instantaneous powers can be expressed as follows:

$$\begin{cases} P_l = \bar{P}_l + \tilde{P}_l \\ Q_l = \bar{Q}_l + \tilde{Q}_l \end{cases} \quad (3)$$

DC values (\bar{P}_l, \bar{Q}_l) of P_l and Q_l are average active and reactive power originating from the positive-sequence component of the nonlinear load current. AC values (\tilde{P}_l, \tilde{Q}_l) of P_l and Q_l are the ripple active and reactive powers.

For harmonic and reactive power compensation, all of the reactive power (\bar{Q}_l and \tilde{Q}_l components) and harmonic component (\tilde{P}_l) of active power are selected as compensation power references and the compensation currents reference are calculated as (4).

$$\begin{bmatrix} i_{f\alpha}^* \\ i_{f\beta}^* \end{bmatrix} = \frac{1}{v_{s\alpha}^2 + v_{s\beta}^2} \begin{bmatrix} v_{s\alpha} & v_{s\beta} \\ v_{s\beta} & -v_{s\alpha} \end{bmatrix} \begin{bmatrix} \tilde{P}_l \\ Q_l \end{bmatrix} \quad (4)$$

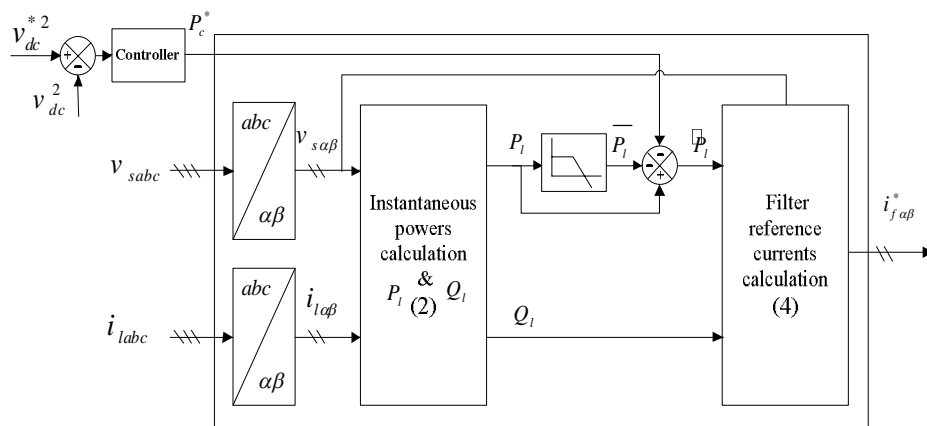


Fig. 2. Harmonic currents extraction scheme using PQ theory.

On the other hand the signal P_c^* is used as an average real power, and is obtained from the DC voltage controller.

B. Harmonic currents extraction using PQ theory based on Multivariable filter

a- Multivariable filter

The multivariable filter (Fig. 3) is designed to extract the fundamental component of electrical signals (voltage or current) directly in the $\alpha\beta$ axes. The transfer function is obtained from the integration of the synchronous reference. The transfer function is defined as [20]:

$$\begin{aligned}\bar{X}_\alpha(s) &= \frac{k}{s}[X_\alpha(s) - \bar{X}_\alpha(s)] - \frac{\omega}{s}\bar{X}_\beta(s) \\ \bar{X}_\beta(s) &= \frac{k}{s}[X_\beta(s) - \bar{X}_\beta(s)] + \frac{\omega}{s}\bar{X}_\alpha(s)\end{aligned}\quad (5)$$

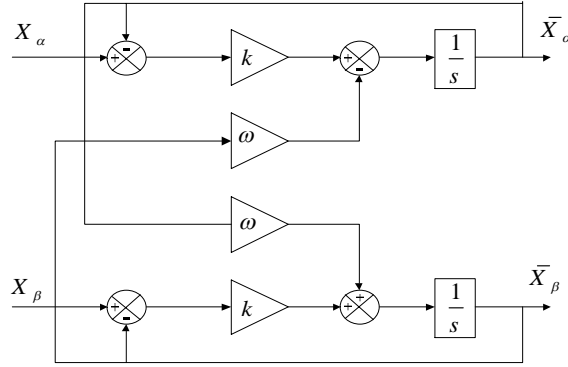


Fig. 3. Harmonic currents extraction scheme using PQ theory.

Finally the robust PQ theory algorithm is shown in Fig. 4.

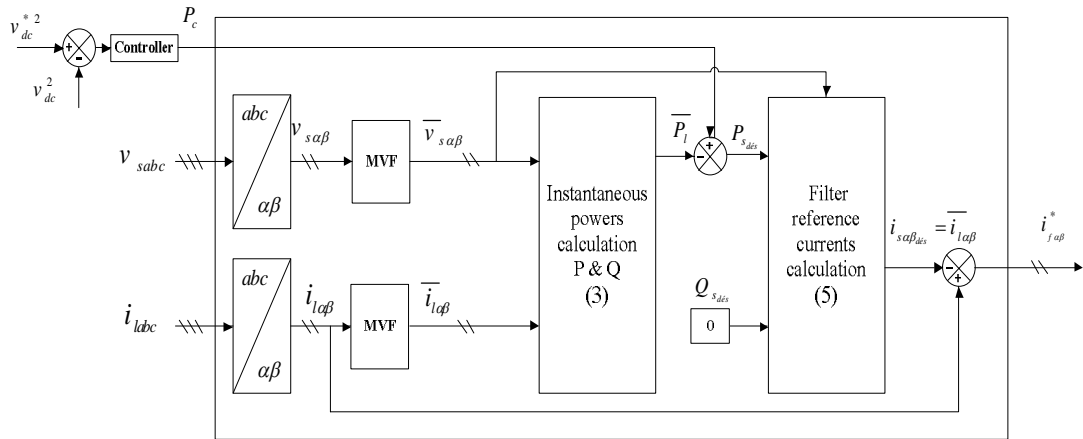


Fig. 4. Harmonic currents extraction scheme using PQ theory.

Sliding Mode Controller (SMC) Synthesis

Consider the nonlinear system represented by:

$$\dot{x} = f(x) + g(x)u \quad (6)$$

where $g(x)$ and $f(x)$ are scalar functions.

The well-known method to form the sliding control law of the previous system is shown in Fig. 5 [21]. It consists of combination between the equivalent control u_{eq} with the switching part u_s , as follows:

$$u = u_{eq} + u_s \quad (7)$$

u_{eq} and u_s can be calculated as follows [22]:

$$u_{eq} = g(x)^{-1}(-f(x) + \dot{x}^*) \quad (8)$$

$$u_s = U_{max} \text{sgn}(S(x)) \quad (9)$$

Where sgn is the sign function, U_{max} is a positive constant and $S(x)$ is the sliding surface.

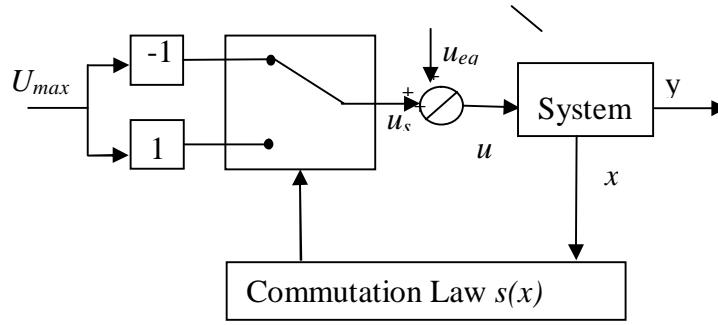


Fig. 5. Adopted sliding mode controller scheme.

A. Currents SMC synthesis

The sliding surfaces are chosen as follows:

$$\begin{aligned} S_1 &= \lambda_1(i_{f\alpha} - i_{f\alpha}^*) \\ S_2 &= \lambda_2(i_{f\beta} - i_{f\beta}^*) \end{aligned} \tag{10}$$

The equivalent control takes the following form:

$$u_{eq} = g(x)^{-1}(-f(x) + \dot{x}^*) \tag{11}$$

The switching control law is designed as follows:

$$u_s = -U_{max} \text{sign}(S) \tag{12}$$

where:

$$S = \begin{bmatrix} S_1 \\ S_2 \end{bmatrix}, \quad U_{max} = \begin{bmatrix} U_{max1} \\ U_{max2} \end{bmatrix}$$

Finally, the control law is given by:

$$\begin{cases} v_{f\alpha}^* = R_f i_{f\alpha} + v_{s\alpha} + L_f \dot{i}_{f\alpha}^* - U_{max1} \text{sign}(S_1) \\ v_{f\beta}^* = R_f i_{f\beta} + v_{s\beta} + L_f \dot{i}_{f\beta}^* - U_{max2} \text{sign}(S_2) \end{cases} \tag{13}$$

where, U_{max1}, U_{max2} are positive constants.

B. DC voltage SMC synthesis

The sliding surface is chosen as follows:

$$S_{dc} = \lambda_{dc} e_{vdc} \tag{14}$$

where:

$$e_{vdc} = v_{dc}^2 - v_{dc}^{*2}$$

The control law is given by the following linear feedback with switching functions.

$$P_c^* = c_1 e_{vdc} y_1 + c_2 \dot{e}_{vdc} y_2 \tag{15}$$

Where, c_1 and c_2 are positive constants, and the switching functions y_1 and y_2 are given by [23]:

$$y_1 = \begin{cases} 1 & \text{si } S_{dc} e_{vdc} > 0 \\ -1 & \text{si } S_{dc} e_{vdc} < 0 \end{cases} \quad \text{and} \quad y_2 = \begin{cases} 1 & \text{si } S_{dc} \dot{e}_{vdc} > 0 \\ -1 & \text{si } S_{dc} \dot{e}_{vdc} < 0 \end{cases} \tag{16}$$

Space Vector Modulation

In this section, SVM technique is presented to produce PWM control signals (s_a, s_b and s_c) to the power switches of the inverter. SVM compensates the required volt-seconds using discrete switching states and their on-times. The space vector diagram of a three phase voltage source inverter is a hexagon (Fig. 6), consisting of six sectors. Every sector is an equilateral triangle of a

height $h = \sqrt{3}/2$ [24]. For any given reference vector, the sector of operation is determined by using Eq (17).

$$S_i = \text{int}\left(\frac{\theta_s}{60}\right) + 1 \quad (17)$$

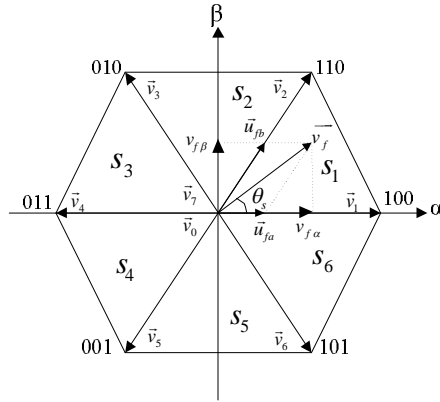


Fig. 6. Space vector diagram.

The on-time calculation is similar for all sectors. Volt-second equation is given by:

$$\vec{v}_f T_s = t_i \vec{v}_i + t_{i+1} \vec{v}_{i+1} + t_0 \vec{v}_0 \quad (18)$$

where $T_s = 1/f_s$, with f_s is the switching frequency.

In the first sector,

$$\begin{cases} \vec{v}_1 = \sqrt{\frac{2}{3}} v_{dc} \\ \vec{v}_2 = \sqrt{\frac{2}{3}} v_{dc} \left(\frac{1}{2} + j \frac{\sqrt{3}}{2}\right) \\ \vec{v}_0 = 0 \end{cases} \quad (19)$$

The reference vector can be also written as follows,

$$\vec{v}_f = v_{f\alpha} + j v_{f\beta} \quad (20)$$

From Equations (18, 19 and 20) one can find:

$$\begin{cases} v_{f\alpha} = \sqrt{\frac{2}{3}} v_{dc} \frac{t_1}{T_s} + \frac{1}{\sqrt{6}} v_{dc} \frac{t_2}{T_s} \\ v_{f\beta} = \frac{1}{\sqrt{2}} v_{dc} \frac{t_2}{T_s} \end{cases} \quad (21)$$

From equation (21), ON times calculation are given below

$$\begin{cases} t_1 = \frac{\sqrt{6} v_{f\alpha} - \sqrt{2} v_{f\beta}}{v_{dc}} T_s \\ t_2 = \frac{\sqrt{2} v_{f\beta}}{v_{dc}} T_s \\ t_0 = T_s - (t_1 + t_2) \end{cases} \quad (22)$$

The choice of the null vector determines the SVM scheme. There are a few options: the null vector v_0 only, the null vector v_7 only, or a combination of the null vectors. A popular SVM technique is to alternate the null vector in each cycle and to reverse the sequence after each null vector as shown in Fig. 7. This will be referred to as the symmetric 7-segment technique [25].

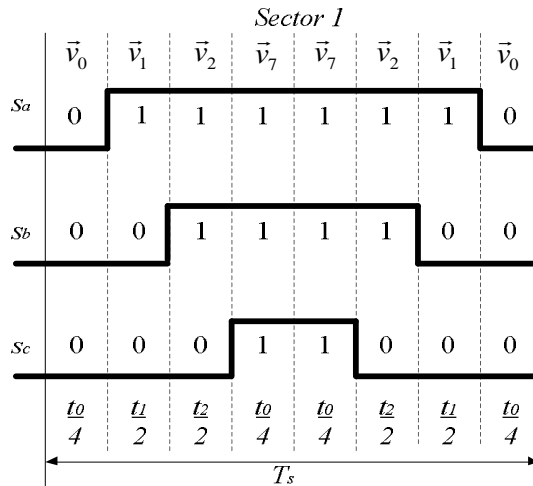


Fig. 7. 7-Segment Switching Sequence for Vref in sector 1.

3. SIMULATION RESULTS AND DISCUSSION

Harmonic current filtering, reactive power compensation and performance of the SHAPF with the proposed control have been examined in Matlab/Simulink environment, under nonlinear load variation and voltage sag. The parameters used in the present study are shown in Table 1.

Table1 System parameters

Parameter	value
RMS value of the source voltage	220 V
DC-link capacitor C_{dc}	8 mF
Source impedance R_s, L_s	3m Ω , 2.6 μ H
Shunt filter impedance R_f, L_f	20 m Ω , 2.5 mH
Line impedance R_l, L_l	10 m Ω , 0.3 μ H
Diode rectifier load R_d, L_d	15 Ω , 2 mH
DC-link voltage reference	900 V
Switching frequency f_s	12 kHz
$\lambda_1 = \lambda_2 = \lambda_{dc}$	1
$U_{max1} = U_{max2}$	840
C_1, C_2	0.3, 0.08

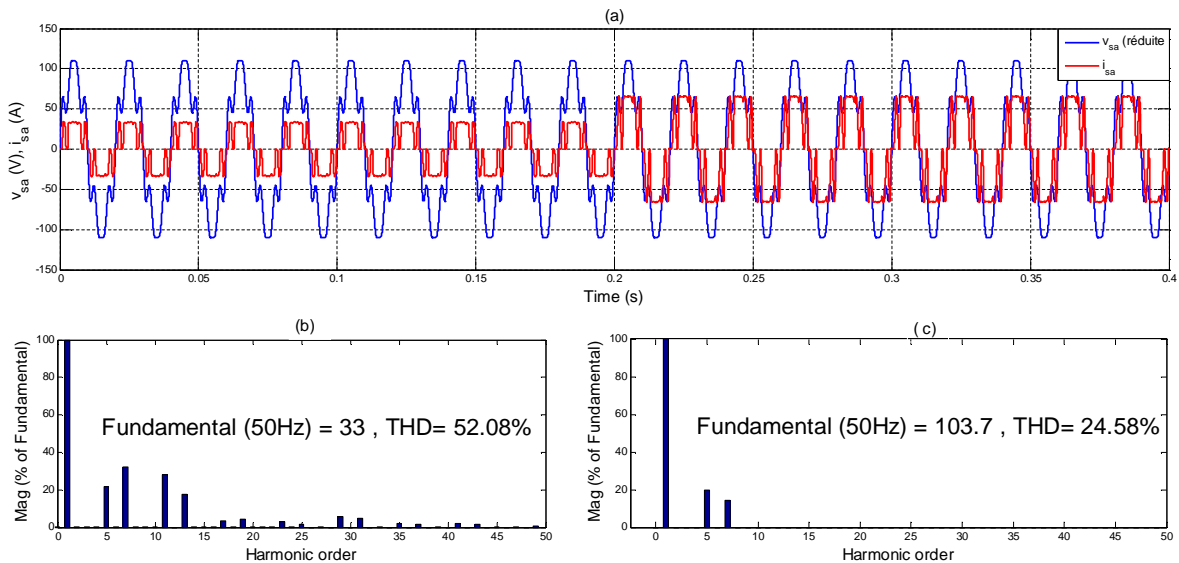


Fig. 8. Simulation results of the perturbed system before compensation. a): Source voltage and source current of a-phase, b): Harmonic spectrum of source current, c): Harmonic spectrum of source voltage

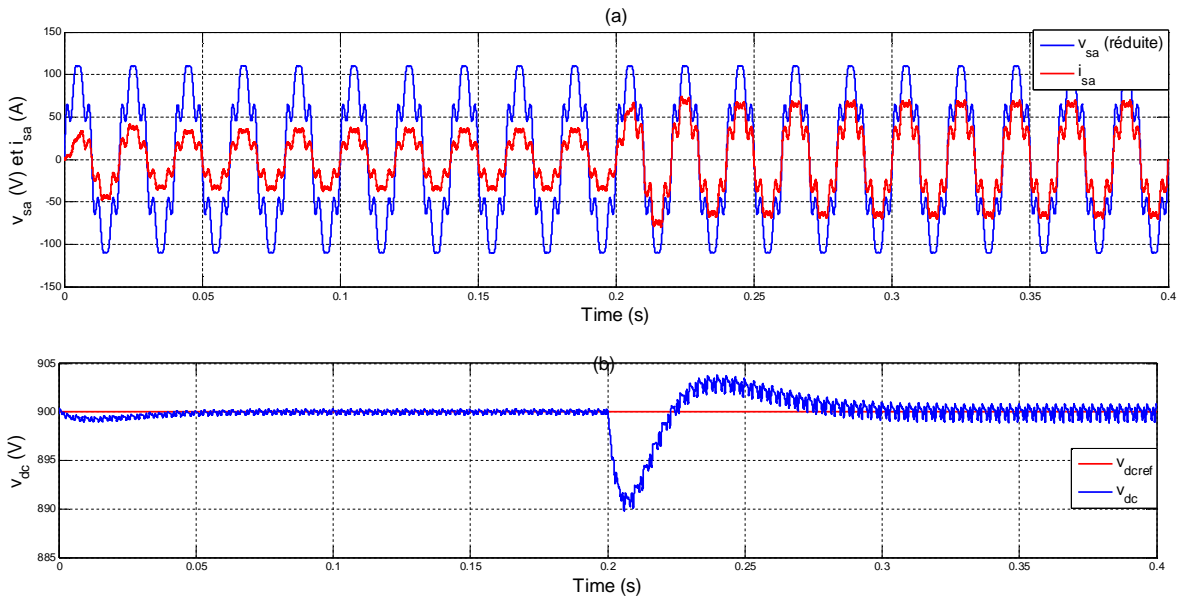


Fig. 9 Simulation results of the proposed sliding mode controller with conventional PQ theory. a): Source voltage and source current of a-phase after compensation, b): DC-link voltage v_{dc} .

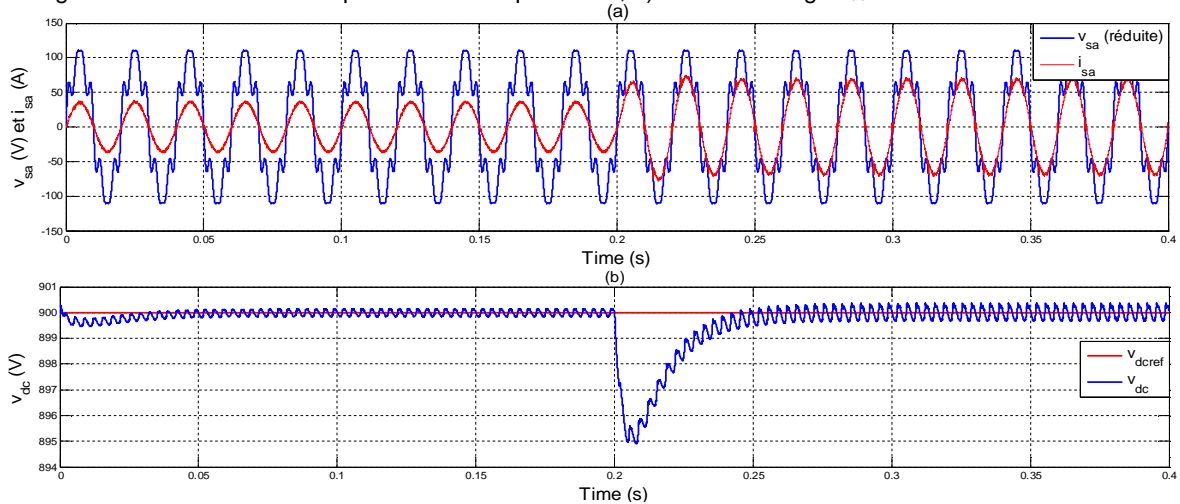


Fig. 10 Simulation results of the proposed sliding mode controller with Robust PQ theory. a): Source voltage and source current of a-phase after compensation, b): DC-link voltage v_{dc} .

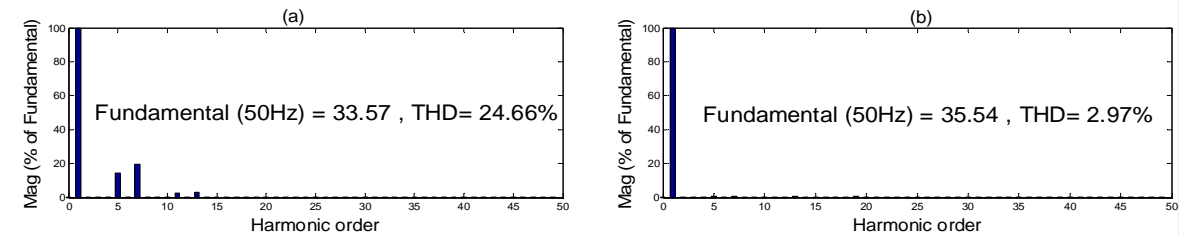


Fig. 11 Harmonic spectrum. a): Harmonic spectrum of source current with conventional PQ theory, b): Harmonic spectrum of source current with robust PQ theory.

The dynamic behavior under a step change of the load at $t = 0.2$ s is presented in Figs. 9.(a) and 10.(a). It can be observed that the grid current becomes sinusoidal after the control application in the case of robust PQ extraction method, whereas there is no enhancement with the conventional PQ. However, the unity power factor operation is successfully achieved in both cases, even in the transient state.

The harmonic spectrum of AC grid current before and after compensation are illustrated in Fig. 8.(b) and (c), and in Fig. 11.(a) and (b). It results that the SHAPF decreases the total harmonic

distortion (THD) in the grid currents from 52.08% to 24.66% with SMC-PQ which not acceptable, while it is further decreases to 2.97% when SMC-Robust PQ is applied.

The absence of an overshoot in DC voltage response during load change, low rise time and low THD, demonstrates the superiority of the proposed control scheme compared to its counterpart conventional controller as illustrated in Table. 2.

Table1 System parameters

Factor	SMC-PQ	SMC-Robust PQ
THDi (%)	24.66	2.97
Charging of DC link (s)	0.08	0.06
Overshoot	+	-

4. CONCLUSION

In this paper a control design of the SHAPF is carried out including its mathematical model and harmonic extraction methods where we have chosen a conventional PQ and a modified PQ based on MVF. A combined sliding mode space vector modulation controller is derived to regulate injected currents. The control of the inverter is derived from space vector modulator due to its benefits in term of fixed frequency and ease of implementation.

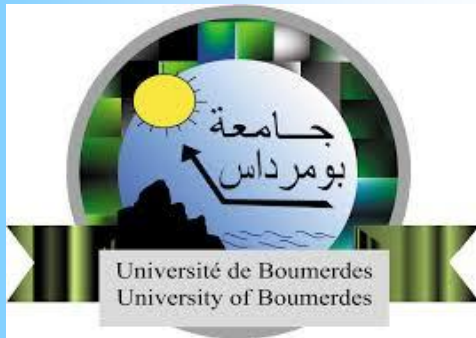
Because it absolutely restored to the balanced set of sinusoidal the source currents under unbalanced source voltage and single-phase loads in the case of SMC-Robust PQ, it has been establish as a successful solution to power quality problems.

References

- [1] Jos Arrillaga, Math H. J. Bollen, Neville R. Watson, "Power Quality Following Deregulation", Pro-ceedings of the IEEE, Vol. 88, No. 2, Feb. 2000.
- [2] W. Edward Reid, "Power Quality Issues - Standards and Guidelines", IEEE Transactions on Industry Applications, Vol. 32, No. 3, May/June 1996.
- [3] Chen, Wenjie, Xu Yang, and Zhaoan Wang. "An active EMI filtering technique for improving passive filter low-frequency performance.", IEEE Transactions on Electromagnetic Compatibility, Vol. 48, No. 1, February 2006.
- [4] Chen, Xiyu, et al. "A novel inverter-output passive filter for reducing both differential-and common-mode dv/dt at the motor terminals in PWM drive systems.", IEEE Transactions on Industrial Electronics, Vol. 54, No. 1, February 2007.
- [5] Hamadi, Abdelhamid, Salem Rahmani, and Kamal Al-Haddad. "A hybrid passive filter configuration for VAR control and harmonic compensation.", IEEE Transactions on Industrial Electronics, Vol. 57, No. 7, July 2010.
- [6] B. M. Han, B. H. Cho, S. K. Sul and J. E. Kim, "Unified Power Quality Conditioner for Compensating Voltage Interruption", Journal of Electrical Engineering & Technology, Vol. 1, No. 4, pp. 503- 512, 2006.
- [7] H-M. Nejad, S. Mohammadi, B. Farhangi, "Novel Control Method for Reducing EMI in Shunt Active Filters with Level Shifted Random Modulation",IEEE,The 6th International Power Electronics Drive Systems and Technologies Conference (PEDSTC), 2015, pp. 585 -590
- [8] S. Rahmani, N. Mendalek and K. Al-Haddad, "Experimental Design of a Nonlinear Control Technique for Three-Phase Shunt Active Power Filter," in *IEEE Transactions on Industrial Electronics*, vol. 57, no. 10, pp. 3364-3375, Oct. 2010.
- [9] L. Asiminoaei, E. Aeloiza, P. N. Enjeti and F. Blaabjerg, "Shunt Active-Power-Filter Topology Based on Parallel Interleaved Inverters," in *IEEE Transactions on Industrial Electronics*, vol. 55, no. 3, pp. 1175-1189, March 2008.
- [10] Chaoui, Abdelmadjid, et al. "PI controlled three-phase shunt active power filter for power quality improvement." *Electric Power Components and Systems*35.12 (2007): 1331-1344.
- [11] Pinto, J. G., et al. "3-phase 4-wire shunt active power filter with renewable energy interface." (2007).
- [12] Bhattacharya, Avik, and Chandan Chakraborty. "A shunt active power filter with enhanced performance using ANN-based predictive and adaptive controllers." *Industrial Electronics, IEEE Transactions on* 58.2 (2011): 421-428.
- [13] Karuppanan, P., and Kamala Kanta Mahapatra. "PI and fuzzy logic controllers for shunt active power filter—A report." *ISA transactions* 51.1 (2012): 163-169.
- [14] A. Benaissa, B. Rabhi, A. Moussi, M. F. Benkhoris, J.C. Le Claire "Fuzzy logic controller for five-level shunt active power filter under distorted voltage conditions" IEEE, 38th Annual Conference on Industrial Electronics Society, IECON 2012, pp: 4973–4978, 25-28 Oct. 2012.

- [15] H. Kouara, A. Chaghi « Three phase four wire shunt active power filter based fuzzy logic dc- bus voltage control” Acta Technica Corviniensis-Bulletin of Engineering, Tome V, 2012.
- [16] P. Kanjiya, V. Khadkikar, H-H. Zeineldin “Optimal Control of Shunt Active Power Filter to Meet IEEE Std. 519 Current Harmonic Constraints Under Nonideal Supply Condition” IEEE Transactions on industrial electronics, vol. 62, no. 2, february 2015.
- [17] Shintemirov, A., “Mathematical morphology based reference signals generation for active power filters,” Electronics Letters , Vol.49, No.10, pp.671-672, May 2013.
- [18] A. Ozdemir.and Z. Ozdemir., "Digital current control of a three-phase four-leg voltage source inverter by using p-q-r theory," Power Electronics, IET , Vol.7, No.3, pp.527-539, March 2014.
- [19] L.S Czarnecki, "Constraints of instantaneous reactive power p-q theory," in Power Electronics, IET , vol.7, no.9, pp.2201-2208, September 2014
- [20] [5] Allali M A. A Contribution to the Study of Active Compensating Low-voltage Electrical, Doctoral thesis ULP – Strasbourg, 2002.
- [21] Y. Harbouche, L. Khellache and R. Abdessemed, “Sliding Mode Control of the Double Fed Asynchronous Machine Applied by Current Sources”, Asian Journal of Information Technology, vol. 6, no. 3, pp. 362-368, 2007.
- [22] R. Guzman, L.G Vicuna,J. Morales, M. Castilla, J. Matas,. "Sliding-Mode Control for a Three-Phase Unity Power Factor Rectifier Operating at Fixed Switching Frequency," in Power Electronics, IEEE Transactions on , vol.31, no.1, pp.758-769, Jan. 2016
- [23] A. Chebabhi, M.K Fellah and M.F Benkhoris “Sliding Mode Controller for Four Leg Shunt Active Power Filter to Eliminating Zero Sequence Current, Compensating Harmonics and Reactive Power with Fixed Switching Frequency ”, Serbian Journal Of Electrical Engineering , Vol. 12, No. 02, pp. 205- 218, june 2015.
- [24] K.Ramya and R.Prakash “Comparative Analysis of PWM Techniques for Three Level Diode Clamped Voltage Source Inverter”, International Journal of Power Electronics and Drive System, Vol. 5, No. 01, pp. 15- 23, July-2014.
- [25] P.Tripura, Y.S.Kishore Babu and Y.R.Tagore “Space Vector Pulse Width Modulation Schemes for Two-Level Voltage Source Inverter”, International Journal on Control System and Instrumentation, Vol. 02, No. 03, pp. 34- 38, October 2011.

People's Democratic Republic of Algeria
Ministry of Higher Education and Scientific research
M'hamed Bougara University, Boumerdes
Institute of Electrical and Electronic Engineering,
Laboratory of Signals and Systems (LSS)



ALGERIAN JOURNAL OF SIGNALS AND SYSTEMS

ISSN : 2543-3792

Title : **Hyperchaos-Based Cryptosystem for Multimedia Data Security**

Authors: **S. Benzegane, S. Sadoudi, M. Djeddou**

Affiliation: **Laboratoire Systèmes de Communications, Ecole Militaire Polytechnique(EMP), Algiers, Algeria.**

Page range: **47- 58**

IMPORTANT NOTICE

This article is a publication of the Algerian journal of Signals and Systems and is protected by the copyright agreement signed by the authors prior to its publication. This copy is sent to the author for non-commercial research and education use, including for instruction at the author's institution, sharing with colleagues and providing to institution administration. Other uses, namely reproduction and distribution, selling copies, or posting to personal, institutional or third party websites are not allowed.

Volume : 1 Issue : 1 (June 2016)

Laboratory of Signals and Systems

Address : IGEE (Ex-INELEC), Boumerdes University, Avenue de l'indépendance, 35000, Boumerdes, Algeria

Phone/Fax : 024 79 57 66

Email : lss@univ-boumerdes.dz ; ajsyssig@gmail.com

Hyperchaos-Based Cryptosystem for Multimedia Data Security

S. Benzegane, S. Sadoudi^{*} and M. Djeddou

Laboratoire Systèmes de Communications, Ecole Militaire Polytechnique(EMP), Algiers, Algeria
sadoudi.said@gmail.com

Abstract: In this paper, we present a software development of multimedia streaming encryption using Hyperchaos-based Random Number Generator (HRNG) implemented in C#. The software implements and uses the proposed HRNG to generate keystream for encrypting and decrypting real-time multimedia data. The used HRNG consists of Hyperchaos Lorenz system which produces four signal outputs taken as encryption keys. The generated keys are characterized by high quality randomness which is confirmed by passing standard NIST statistical tests. Security analysis of the proposed encryption scheme through image and audio security analysis confirms its robustness against different kind of attacks.

Keywords: Hyperchaos Lorenz System, HRNG, Multimedia security, C#.

1. INTRODUCTION

In recent years, with the rapid growth of wireless multimedia service, there is an increasing requirement for higher secure data transmission such as video and audio data. In this way, to protect multimedia contents, cryptology, which appears to be an effective way for information security, has been employed in many practical applications [1]. However, traditional ciphers like DES [2], IDEA [3], RSA [4] and AES [5], are often used for text or binary data, while not suitable for direct video and audio encryption [6]. The main reason is that multimedia applications require real-time operations, which imposes logically the use of stream ciphers instead of block ciphers.

Recently, an increasing attention has been devoted to the usage of chaos theory to implement encryption process. The main advantage of these encryptions lies in the observation that a chaotic signal looks like noise for non-authorized users ignoring the mechanism for generating it [7-13]. In fact, chaotic system is sensitive to initial condition values, this means that the different initial conditions produce different trajectories, but the same conditions can produce the same trajectories. It is known that most chaotic cryptosystems in essence behave as stream ciphers [12]. In this way, the authors in [10] and [11] have proposed hardware chaos-based stream cipher for ciphering audio and image data respectively. The cryptosystems are implemented in FPGA circuits which offer high speed and low cost. However, applying these hardware chaos-based cryptosystems to secure real-time multimedia data seem to be very difficult. For that reason, and with the rapid development of Internet and the place taken by multimedia data exchange in internet, software chaos-based cryptosystems appear as an interesting and less difficult alternative to secure multimedia data instead of hardware cryptosystems. In fact, many research works are proposed in this domain. We cite the work in [13], where a new fast and light stream cipher, named Enigmedia, based on a hyperchaotic dynamical system is proposed. It has been implemented in a videoconference Application for Smartphone. In [14-16] various cryptographic schemes are reported for streamcipher and image encryption. In addition, many chaotic Map based block ciphers are proposed including [17-18]. However, it is known that 1D or 2D chaotic Map systems have a poor chaotic dynamical behavior. In [6], the authors give an interesting survey of chaos-based encryption algorithms for image, video and audio respectively. They affirm that chaos-based multimedia encryption demonstrates superiority over the conventional encryption methods and can be used as the foundation of future research. However, they suggest that chaos-based multimedia encryption is not yet mature and more efforts are needed for its further development toward practical applications with high security, low computational complexity, invariance of compression ratio, format compliance, real-time, multiple levels of security, and strong transmission error tolerance.

In this paper, we propose a software development application designed in C# using the “.NET Framework” for real-time multimedia data encryption in Wi-Fi network. We exploit the four

simultaneously generated signals of the implemented hyperchaotic Lorenz system to generate cryptographic keys with good statistical properties. To implement the Lorenz system, we use the well-known fourth order Runge-Kutta (RK-4) method for resolving autonomous continuous chaotic system models. For encoding data, we use base64 encoded numbers class provided with the “.NET Framework” which use 64 bits (16Q48) double precision data format after removing the decimal parts, i.e, we take only the fractional parts. The generated keys are validated through the NIST statistical tests [16], which demonstrate their good statistical performances. In addition, a security analysis of both, encrypted image and encrypted audio results, are realized by analyzing histogram of ciphered data, key sensitivity of the algorithms, statistical analysis using the correlation parameters and entropy and by looking at the key space, the probability distributions and spectrogram representation. Concerning the transmission of the real-time video data over IP network, we use UDP (User Datagram Protocol) protocol via Wi-Fi connection.

The rest of this paper is organized as follows. A principle generation of the hyperchaotic encryption keys generation with C# implementation is given in Section 2. Section 3 further describes the principle of the proposed hyperchaos-based cryptosystem. Section 4 shows a graphic user interface of developed software application. Image and audio security analysis of the cryptosystem is given in Section 5 and Section 6 respectively. Conclusions are finally drawn in Section 7.

2. ROBUST HYPERCHAOTIC ENCRYPTION KEYS

To generate robust encryption keys, we use the hyperchaotic Lorenz system which is described by the following nonlinear dynamic equations [19]:

$$\begin{cases} \dot{x} = a(y - x) \\ \dot{y} = x(b - z) - y + w \\ \dot{z} = xy - cz \\ \dot{w} = -dx \end{cases} \quad (1)$$

where x , y , z and w are four state variables, and a , b , c and d are positive real constants. The system is hyperchaotic for the parameters values $a = 10$, $b = 28$, $c=8/3$ and $d =5$, and with the initial conditions values $x_0 = -10$, $y_0 = -10$, $z_0 = -10$ and $w_0 = -10$.

Chaotic Encryption Keys Problem

It should be noted that the generated hyperchaotic keys encoded on 64-bits floating point data format suffer from long sequences of zeros and ones particularly in the integer parts. This leads to generate encryption keys with bad statistical performances, which is verified by testing them in the NIST test battery [20]. Thus, to overcome this problem and that of finite precision, we should increase the fractional data length. As a solution, we propose to increase the data length of the fractional part and decrease that of the integer part, and choose the fractional part as the encryption keys. This solution is the basic idea of the proposed Hyperchaos-based RNG (HRNG) for which the principle detail is given in the next subsection. This is the same idea used in [7] for fixed-point data format, it has given good results for hardware FPGA implementation of continuous chaotic systems.

HRNG Principle

The proposed HRNG principle scheme is illustrated in Fig. 1. It is composed by an hyperchaotic Lorenz generator implemented previously in C# using RK-4 method. After the generation of the four hyperchaotic signals x , y , z and w , we take only the fractional parts $F(.)$ of the hyperchaotic samples. To obtain the hyperchaotic encryption keys K_1 , K_2 , K_3 and K_4 , we encode on 64-bits double precision floating point data format, the obtained fractional parts $F(x)$, $F(y)$, $F(z)$ and $F(w)$. Note that the use of 64-bit double precision permits to overcome the problem of finite precision. Also it is possible to obtain long encryption keys multiple of 64 as 128, 192, 256 and so on by using concatenation operation. From this idea, we can express mathematically the HRNG equation system as follow:

$$\begin{cases} K_1 = F(x) \\ K_2 = F(y) \\ K_3 = F(z) \\ K_4 = F(w) \end{cases} \quad (2)$$

In fig. 2, we present the analog representation of the encryption keys K_1 , K_2 , K_3 and K_4 and different 2D attractors (K_1/K_2 , K_1/K_3 , K_1/K_4) (Fig. 2(a)) compared to that of the hyperchaotic Lorenz system x , y , z and w , and 2D hyperchaotic attractors (x/y , x/z , x/w) respectively (Fig. 2(b)). Note that the obtained encryption keys K_1 , K_2 , K_3 and K_4 have the same behavior of that noise signals and the 2D attractors show that the phase spaces are completely and randomly occupied by the hyperchaotic trajectories.

To confirm and validate the claimed performance, we must evaluate the quality of randomness of the proposed HRNG. For this, statistical tests of the generated 64-bit encryption keys are commonly performed using the standard NIST SP 800-22 statistical test suite [20]. Table 1 summarizes the results of NIST test for the proposed HRNG. In this test suite, each test was performed 300 times on 1 Mbit substrings. A single test is considered as passed if the *P-value* is above the significance level of 0.01 or below 0.99 [20]. However, in Table 1, we show the measured values of *P-value_T* knowing that if *P-value_T* ≥ 0.0001 , then the sequences can be considered to be uniformly distributed and the minimum pass rate for each statistical test with the exception of the random excursion (variant) test is approximately 0.972766 for sample size equal to 300 binary sequences, for more details see the reference [20].

From the results of Table 1, we note that the encryption keys generated by the HRNG pass all kinds of the NIST test. Thus, we can say that our HRNG generates encryption keys with good statistical performances, i.e., good randomness keys.

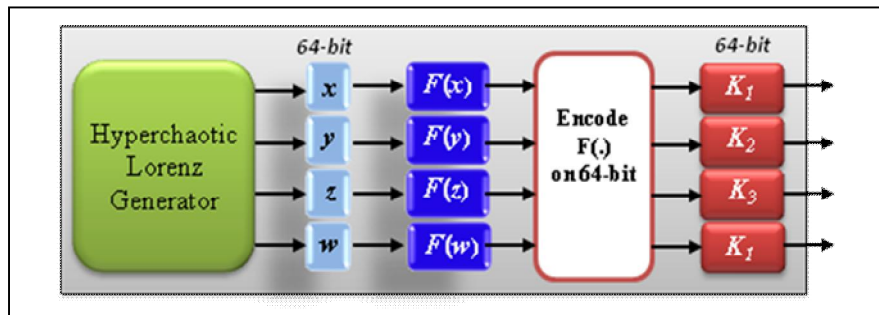


Fig. 1 HRNG principle scheme.

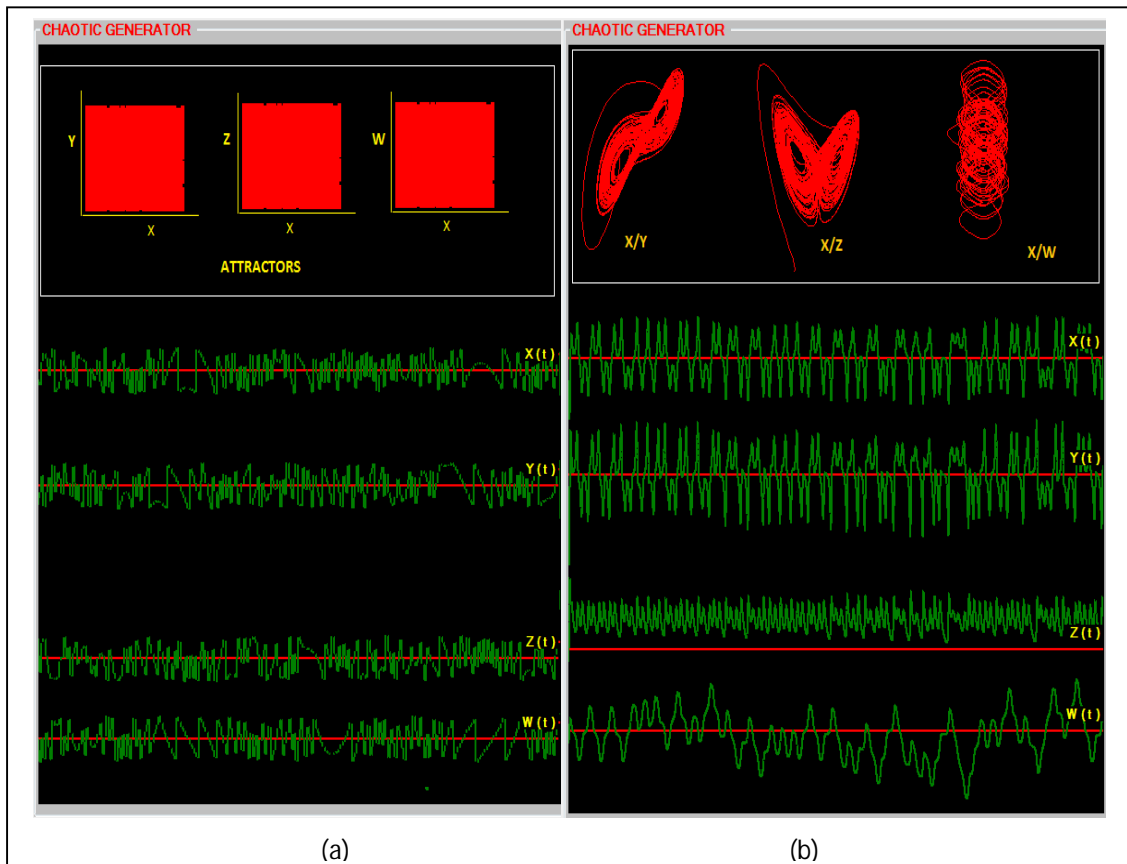


Fig. 2 C# Simulation result: (a) The analog representation of the encryption keys K_1 , K_2 , K_3 and K_4 and (b) The hyperchaotic 2D attractors and signals (x, y, z, w) .

Table 1 Nist Test Results

Statistical Tests	$P\text{-VALUE}_T$	Proportion
Frequency	0.644060	0.9800
Block-Frequency	0.023545	0.9833
Cumulative Sum up	0.671779	0.9900
Cumulative Sum down	0.699313	0.9933
Runs	0.117661	0.9933
Longest-run	0.630178	0.9967
Rank	0.840081	0.9867
FFT	0.100508	1.0000
N.P. templates	0.588652	0.9767
Over. Templates	0.547637	1.0000
Universal	0.568055	0.9833
App. Entropy	0.162606	0.9933
R.Excursions	0.249991	0.9947
R.E variant	0.711827	0.9840
Serial 1	0.706149	0.9833
Serial 2	0.110952	0.9833
Lempel ziv	0.071177	0.9900
L. Complexity	0.487885	0.9967

3. PROPOSED HYPERCHAOS-BASED CRYPTOSYSTEM

The principle scheme of the proposed hyperchaos-based multimedia cryptosystem is presented in figure (3). The encryption process consists of XORing the compressed video data with dynamical hyperchaotic keys K_1 and the compressed audio data with other dynamical keys K_2 . Note that these

dynamical keys K_1 and K_2 are generated simultaneously by the proposed HRNG (Fig. 1). We say dynamical keys because the HRNG generates a great number of keys without any repetition. Knowing that in symmetric cryptographical system, it is important to not repeat the same key because if an eavesdrop identifies the keystream, it could use this information to recover the message. For that reason, continuous chaotic systems offers great advantage for the encryption keys generation in cryptography. The obtained video (or audio) keystream is then packetized to be streamed over UDP. Also, the Decryption process consists of XORing the received buffered stream data (video or audio) by the same hyperchaotic keys K_1 or K_2 respectively followed by decompression level and then visualization process (listening through speaker).

Compressed Video Encryption

For the compressed video encryption process, we can define the keys K_1 as follow:

$$K_1 = [K_{11}, K_{12}, K_{13}, \dots, K_{1M}] \tag{3}$$

where M is the number of the generated keys K_1 for the video encryption, Knowing that each key K_{1i} ($i=1, \dots, M$) is encoded on 64-bit. Thus, in the proposed encryption process, M is fixed by the length of video data stream. For example, if the data stream length is 1024 bytes and the key length is 8-bit, then $M=1024$.

At the receiver, it should be noted that, it is necessary to use identical hyperchaotic keystream for the decryption process. This is guaranteed by robust synchronization of the received data with the locally generated hyperchaotic keys by using UDP package.

Compressed Audio Encryption

We use the same reasoning as above for the compressed audio encryption process. In fact, we can define the keys K_2 as follow:

$$K_2 = [K_{21}, K_{22}, K_{23}, \dots, K_{2N}] \tag{4}$$

where N is the number of the generated keys K_2 for the audio encryption.

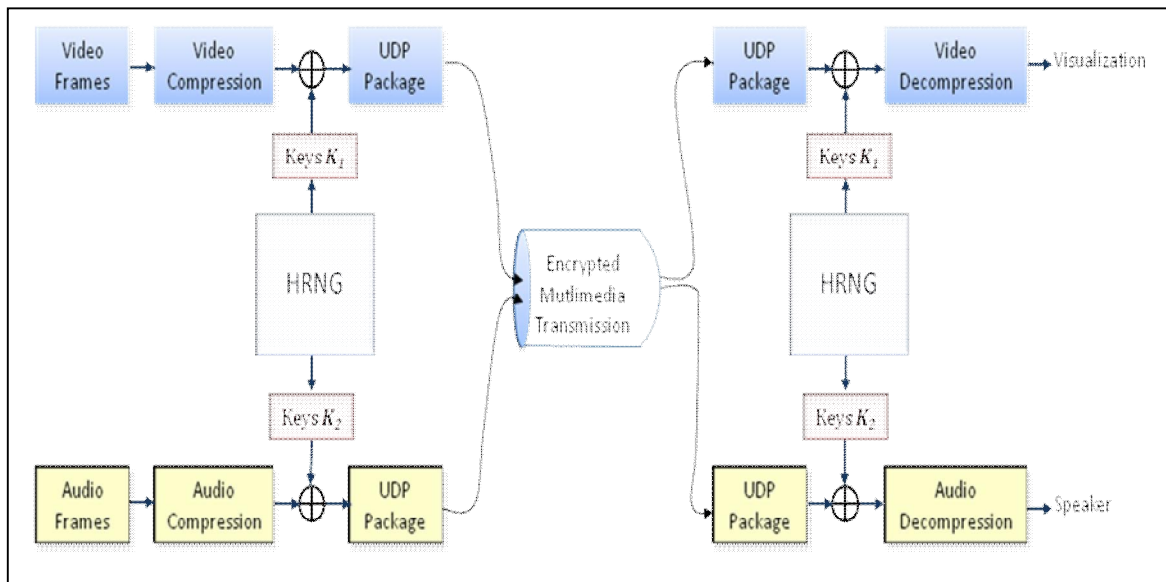


Fig. 3 Block diagram of the proposed hyperchaos-based multimedia cryptosystem.

4. APPLICATION

To validate the proposed hyperchaos-based multimedia cryptosystem, we have developed the software main form presented in the figure (4-a). This latter includes the necessary widgets for

easier use. To evaluate performance for video delivery between two devices (laptops), we use Wi-Fi ad-hoc mode where the server device and the client device communicate directly. Experiments results for video and audio streaming with encryption and decryption process are represented in the figure (4-b) and figure (4-c) for server and client side respectively. The streaming video data from web camera and audio streaming data from microphone are played in real-time with a good quality and low latency.

5. IMAGE SECURITY ANALYSIS

In this section, we give the security analysis of the encryption image results. This latter must not be recovered by cryptanalyst if they want to break the cipher text. In this way, security analysis on chaos-based encryption is done by analyzing histogram cipher image, key sensitivity of the algorithms, statistical analysis using the correlation parameters and entropy and by looking at the key space available if carried out and analyze the cipher strength of a brute force attack [20].

Entropy

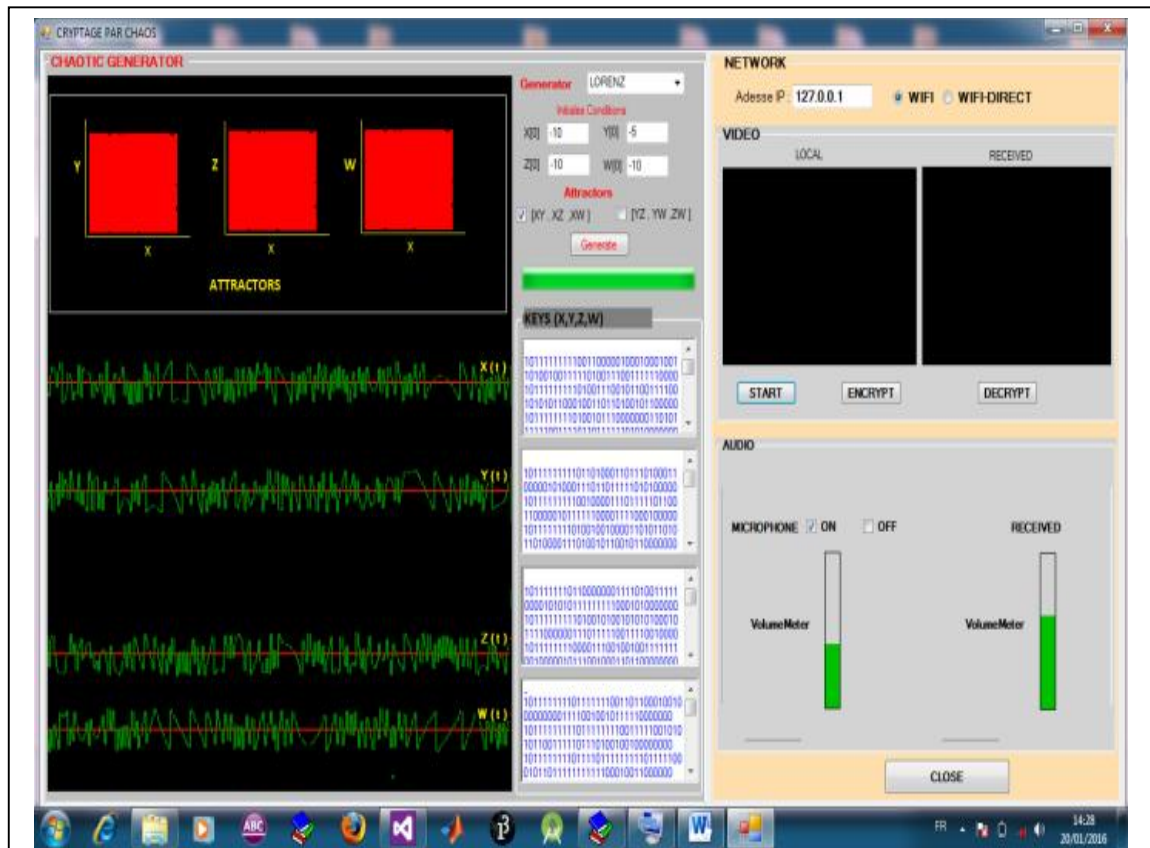
It is considered that ideal entropy value was 7.99902 (≈ 8). Thus, an encryption system designed safe from entropy attack, if it guaranty an entropy value ≈ 8 [20]. The result of the entropy calculation is shown in Table 2.

Table 2 Entropy Evaluation

Test Image	Size	Entropy Value
Mandaril	512 x 512	7.9993
Cameramman	256 x 256	7.9968

Image Correlation

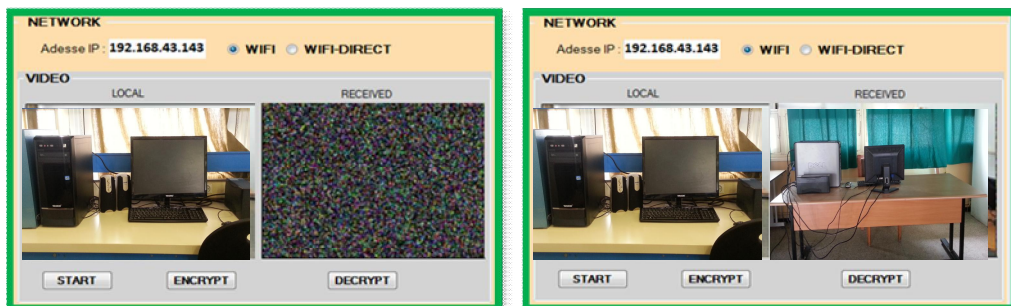
It is known that an ideal encryption algorithm should produce the cipher images with no such correlation in the adjacent pixels (correlation ≈ 0) [20]. The result of the calculation of the correlation is shown in Table 3. These results indicate and confirm that the proposed cryptosystem possesses high security against statistical attacks.



(a)



(b)



(c)

Fig. 4 C# Main form of the application: (a) Server side, (left) received encrypted video from the client and (right) the decrypted video and (b) Client side, (left) received encrypted video from the server and (right) the decrypted video.

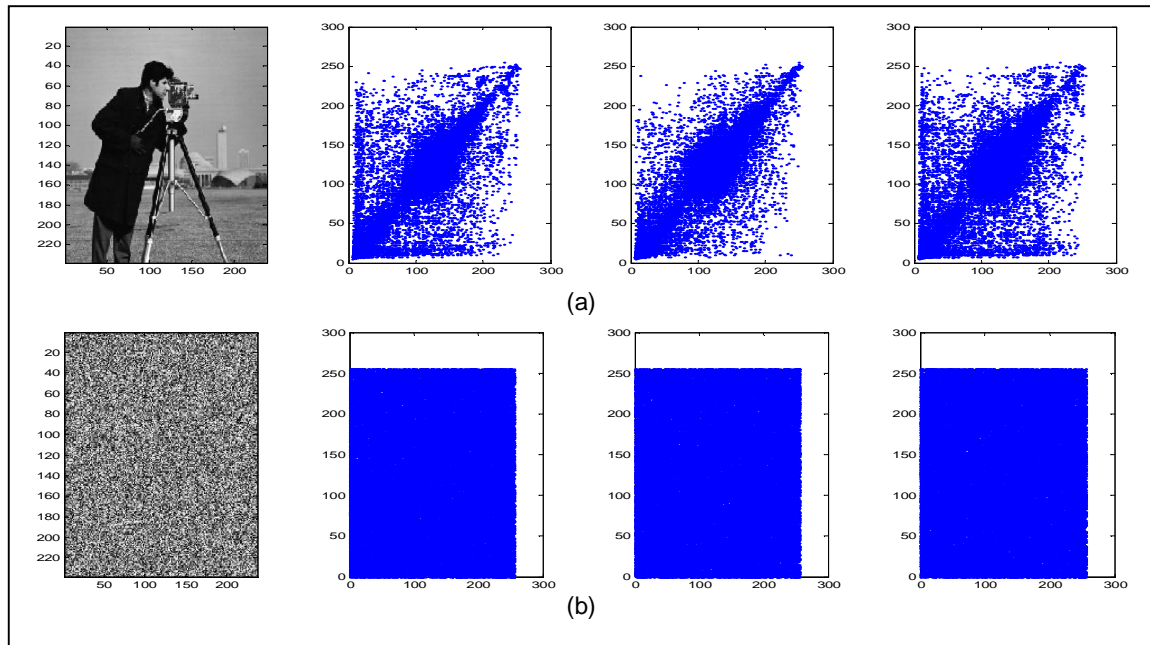


Fig. 5 Image correlation compute results: (a) Original Cameraman image and (b) Encrypted Cameraman image.

Table 3 Correlation Evaluation

Test Image	Size	Entropy Value
Mandaril	512 x 512	0.00128098
Cameramman	256 x 256	-0.00484255

Histogram of encrypted images

In cryptography, an ideal image encryption scheme should generate a ciphered image with different histogram from original images. As it is shown by the results in Fig. 9 and Fig. 10, the histograms of the ciphered images Mandril and Cameraman respectively are significantly different from original images, and allow no statistical resemblance to the plain image.

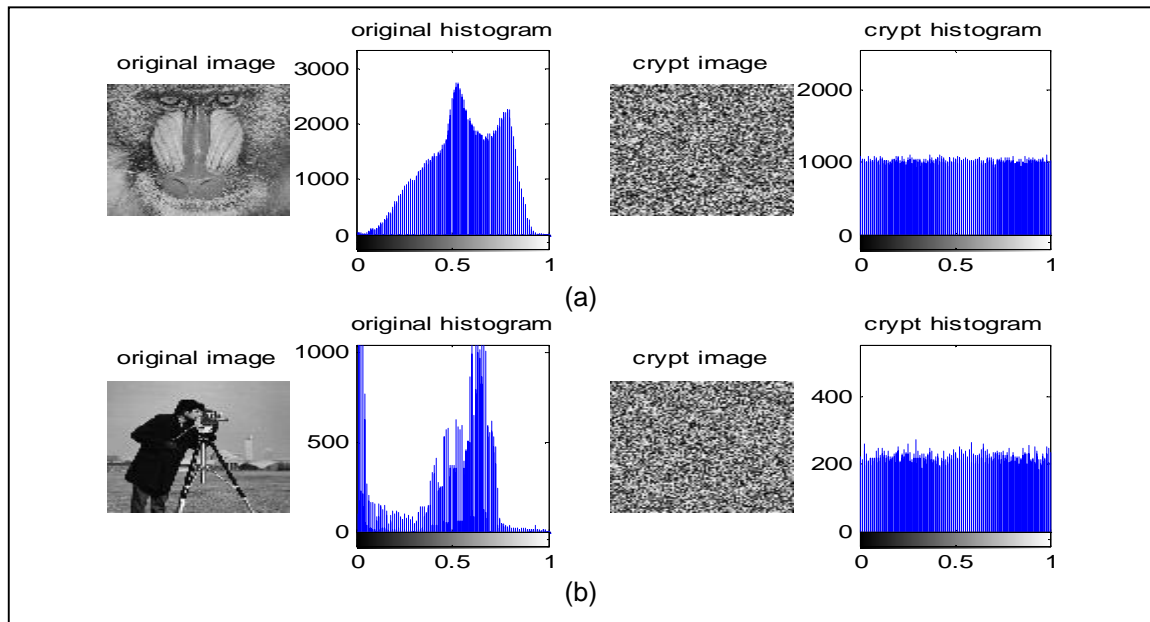


Fig. 6 Histogram of encrypted images: (a) Madril image and (b) Cameraman image.

Key Sensitivity

Another performance measure in cryptography is the guaranty of key sensitivity. This means that, the cryptosystem should be sensitive with respect to both the secret key and plain image. In fact, the change of a single bit in either the secret key or plain image should produce a completely different encrypted image [20].

The figures (11) and (12) give the results of decrypting the ciphered images Mandril and cameraman respectively with a difference of 10^{-14} between the two keys. These results show that the proposed cryptosystem is very sensitive to small difference in the secret key.



Fig. 7 Key sensitivity analysis: (a) madril image and (b) cameraman image.

Key Space

In image encryption domain, the secret key space should be large enough. This leads to make brute force attacks not possible [12]. For the proposed cryptosystem, the key space is estimated as follows:

- Secret Keys are the parameters (a, b, c, d) and the initial conditions (x_0, y_0, z_0, w_0) of the hyperchaotic Lorenz system. Thus, we have 8 parameter keys,
- Each secret keys is encoded on 64-bit,
- So it is likely that the key space is:

$$H(x_0, y_0, z_0, w_0, a, b, c, d) = 2^{(8 \times 64)} = 2^{512}$$

We can conclude that the Key space of the proposed cryptosystem is large enough to resist the brute-force attack. In Table IV, we show a comparison of our key space value with that of [21] and [22].

Table 4 Evaluation of the Keys Space

Encryption scheme	Key Space
Ref. [21]	2^{266}
Ref. [22]	2^{349}
Proposed cryptosystem	2^{512}

6. AUDIO SECURITY ANALYSIS

In the figure (8), we present the audio security analysis including the autocorrelation computation, the probability distribution and the specteogram representation of the original and encrypted audio signals. In fig.(8-a), we present the original audio signal (left) and the encrypted signal (right). Figure (8-b) shows the autocorrealtions of the original signal (left) and the encrypted audio signal (right). The probability distributions, compred to that of normal ditribution, of the original signal (left) and the encrypted signal (right) are presented in figure (8-c). Finally, the figure (8-d) presents spectogram representation of the original (left) and encrypted signals (right). All of these results show and validate the robustness of the encryption audio process using the hyperchaotic encryption keys K_2 .

7. CONCLUSION

In this paper, we have proposed hyperchaos-based cryptosystem for multimedia data security. To generate dynamic ciphering keys, an Hyperchaos-based Random Number Generator (HRNG) implemented on C# language is used. The basic idea is to exploit the four hyperchaotic signals of the Lorenz system to generate the ciphering keys with good statistical properties i.e, high quality of randomness. By passing all of the NIST tests, the proposed HRNG provides good quality random encryption keys which are used as keystream for video and audio encryption and decryption process via Wi-Fi network. In addition, the security analysis of the proposed hyperchaos-based cryptosystem has demonstrated and validated its robustness against several attacks. The proposed approach can be applied for securing all type of multimedia data transmission in dvice to device communication systems.

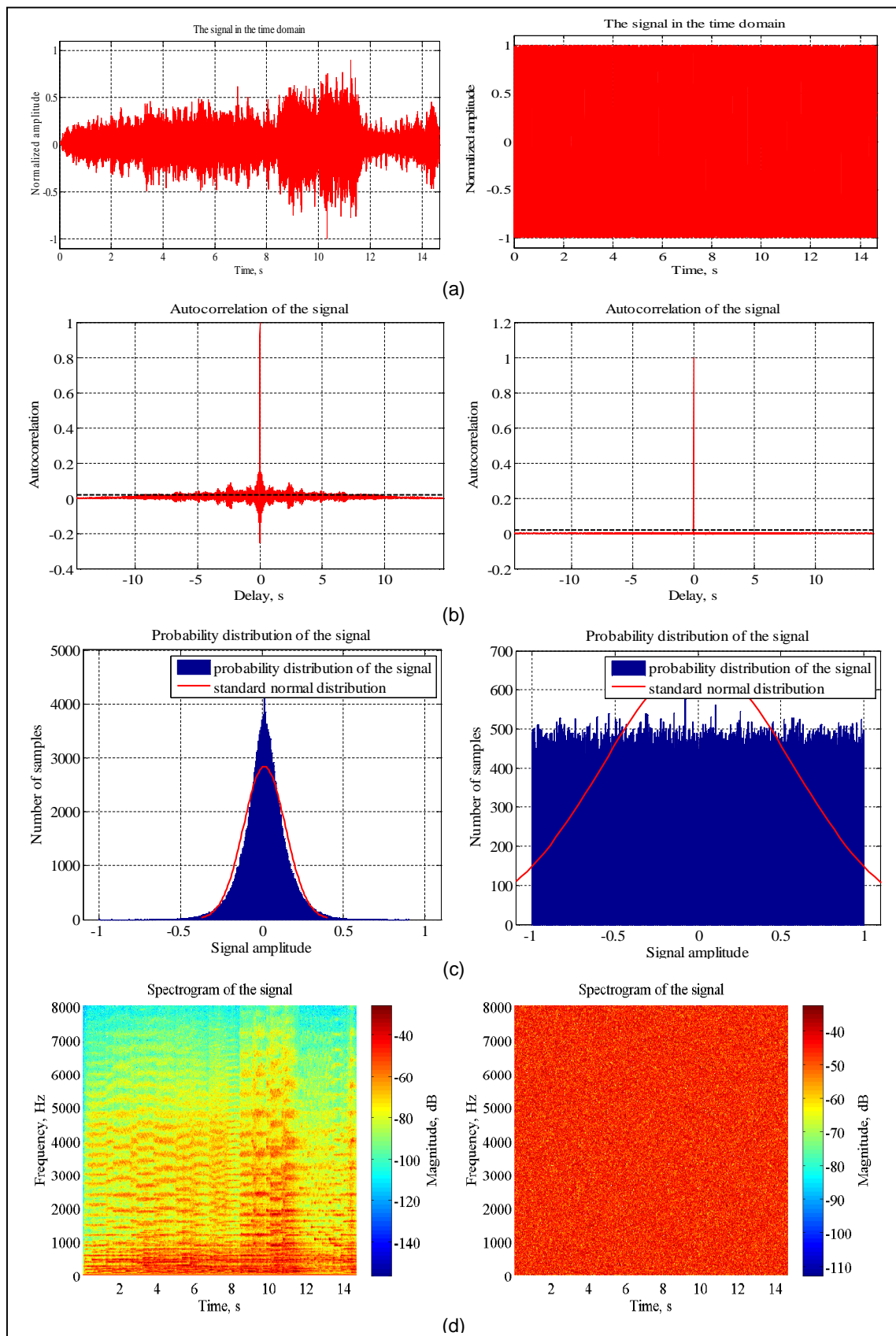


Fig. 8 Audio security analysis results: (a) Original audio signal (L) encrypted audio signal (R), (b) the autocorrelations of the original signal (L) and the encrypted audio signal (R), (c) the probability distributions of the original signal (L) and of the encrypted signal (R), (d) the spectrogram representation (L) and encrypted signals (R).

References

- [26] S. Lian, "Multimedia Content Encryption: Techniques and Applications," Auerbach Publication, Taylor & Francis Group, 2008.
- [27] W. Tuchman, "A brief history of the data encryption standard," ACM Press, Addison-Wesley Publishing Co., New York, 1997.
- [28] P. P. Dang and P.M. Chau, "Implementation IDEA algorithm for image encryption," In Mathematics and Applications of Data/Image Coding, Compression, and Encryption III. Proceedings of SPIE, vol. 4122, 2000, pp. 1–9.
- [29] T. H. Cormen, C. E. Leiserson, R. L. Rivest and C. Stein, "Introduction to algorithms," 2nd edn. MIT Press, McGraw-Hill, Cambridge, 2001.
- [30] FIPS Publication 197, the Advanced Encryption Standard (AES), U.S. DoC/NIST, November, 2001.
- [31] Zhaopin Su, Guofu Zhang and Jianguo Jiang, "Multimedia Security: A Survey of Chaos-Based Encryption Technology," Multimedia - A Multidisciplinary Approach to Complex Issues, Dr. Ioannis Karydis (Ed.), ISBN: 978-953-51-0216-8, 2012, InTech.
- [32] S. Sadoudi, C. Tanougast and A. Dandache, "Hyperchaos-Based True Random Number Generator for Data Stream Encryption," Book Chapter in "Progress in Data Encryption Research", Nova Publisher, 2013.
- [33] T. Yang, C.W. Wu, L.O. Chua, "Cryptography based on chaotic systems," IEEE Trans. on Circuits and Systems-I: Fundamental Theory and Applications, 44, 469–472 (1997).
- [34] C. K. Volos, I. M. Kyprianidis, and I. N. Stouboulos, "Image encryption process based on chaotic synchronization phenomena," Signal Processing, 93, 2013, pp. 1328-1340.
- [35] M. S. Azzaz, C. Tanougast, S. Sadoudi and A. Bouridane, "Synchronized hybrid chaotic generators: application to real-time wireless speech encryption," Communications in Nonlinear Science and Numerical Simulation, 2013, 18(8): 2035-2047.
- [36] S. Sadoudi, C. Tanougast, M. S. Azzaz and A. Dandache, "Design and FPGA implementation of wireless hyperchaotic communication system for secure real-time image transmission", EURASIP Journal on Image and Video Processing 2013, 2013:43.
- [37] G. Alvarez, S. Li, "Some Basic Cryptographic Requirements for Chaos-Based Cryptosystems", Int. J. Bifurcat. Chaos Appl. Sci. Eng. 2006, 16, 2129–2151.
- [38] G. Vidal, M.S. Baptista and H. Mancini, "A fast and light stream cipher for smartphones," Eur. Phys. J. Special Topics, (2014).
- [39] K. Ganesan, K. Murali, "Image encryption using eight dimensional chaotic cat map", Eur. Phys. J. Special Topics 223(8), 1611 (2014).
- [40] P. Shanmugavadivu, P.S. Eliahim Jeevaraj, "Adaptive integrated function systems filter for images highly corrupted with fixed-value impulse noise", Eur. Phys. J. Special Topics 223(8), 1623 (2014).
- [41] T.M. Hoang, D. Tran, "Cryptanalysis and security improvement for selective image encryption", Eur. Phys. J. Special Topics 223(8), 1635 (2014).
- [42] Y.B. Mao, G. Chen, S.G. Lian, "A novel fast image Encryption scheme based on the 3D CB Map", Int. J. Bifurcate Chaos, 2004, Vol. 14, pp. 3613–3624.
- [43] Fengjian Wang, Yongping Zhang and Tianjie Cao, "Research of chaotic block cipher algorithm based on Logistic map", 2nd Int. Conference on Intelligent Computation Technology and Automation, 2009, pp. 678–681.
- [44] R. Barboza, "Dynamics of a hyperchaotic Lorenz system," Int. J. of Bifurcation and Chaos, vol. 17, no. 12, pp. 4285–4294, 2007.
- [45] A. Rukhin, J. Soto, J. Nechvatal, M. Smid, E. Barker, S. Leigh, M. Levenson, M. Vangel, D. Banks, A. Heckert, J. Dray, S. Vo, "A Statistical Test Suite for Random and Pseudorandom Number Generators for Cryptographic Applications," NIST Special Publication 800-22 Revision 1a, April 2010.
- [46] P. Irfan, Y. Prayudi and I. Riadi, "Image Encryption using Combination of Chaotic System and Rivers Shamir Adleman (RSA)," Int. J. of Computer Applications, Vol. 123, N.6, 0975–8887.
- [47] M. A. B. Younes, A. Jantan, "Image Encryption Using Block-Based Transformation Algorithm," IAENG, International Journal of Computer Science, 35:1, 200

People's Democratic Republic of Algeria
Ministry of Higher Education and Scientific research
M'hamed Bougara University, Boumerdes
Institute of Electrical and Electronic Engineering,
Laboratory of Signals and Systems (LSS)



ALGERIAN JOURNAL OF SIGNALS AND SYSTEMS

ISSN : 2543-3792

Title : **Sliding mode control of a Five-Phase Series-Connected Two-Motor Drive**
Authors: **L. Nezli, O. Zouaid**
Affiliation: **Laboratory of control and processing Polytechnic school Bp 182 Hassan Badi El Harrach Alger, Algeria.**
Page range: **59- 68**

IMPORTANT NOTICE

This article is a publication of the Algerian journal of Signals and Systems and is protected by the copyright agreement signed by the authors prior to its publication. This copy is sent to the author for non-commercial research and education use, including for instruction at the author's institution, sharing with colleagues and providing to institution administration. Other uses, namely reproduction and distribution, selling copies, or posting to personal, institutional or third party websites are not allowed.

Volume : 1 Issue : 1 (June 2016)

Laboratory of Signals and Systems
Address : IGEE (Ex-INELEC), Boumerdes University, Avenue de l'indépendance, 35000,
Boumerdes, Algeria
Phone/Fax : 024 79 57 66
Email : lss@univ-boumerdes.dz ; ajsyssig@gmail.com

Sliding mode control of a Five-Phase Series-Connected Two-Motor Drive

Lazhari.NEZLI^{(1)*}Omar Zouaid^{(2)*}

Laboratory of control and processing Polytechnic school Bp 182 Hassan Badi El Harrach Alger,
Email: L_Nezli@yahoo.fr ,Email: o_zomardj125@yahoo.fr

Abstract: In this work, we study vector control and sliding mode control of series-connected five-phase two asynchronous machines supplied with a three levels inverter. After presentation of multiphase machines, we worked out the mathematical model of five phase asynchronous machine supplied with voltage inverter. Application of Park transformation reduces considerably the mathematical model of machine. After, we applied vector control and sliding mode control to the five-phase induction machine. After that, we study a multi-machine system which comport five-phase two asynchronous machines supplied with a single voltage inverter.

In the last, we had the independent vector control and the sliding mode control of series-connected five-phase two asynchronous machines. We observe that an appropriate transposition of phase's order permits an independent control of two machines.

Keywords: Five-phase, asynchronous machine, multi-machine systems, phase's transposition, vector control, sliding mode control.

1.INTRODUCTION

Ever since the inception of the first five- phase variable speed drive in 1969 [1], five-phase machines have been considered as a viable alternative to three-phase machines. This especially holds true for high-power and safety-critical variable speed applications, where a five-phase drive can be realized using inverters with smaller rating per leg while enabling fail-safe operation in redundancy mode [2], [3].

A vector control scheme for a five-phase machine is in its basic form, regardless of the machine type, identical to the corresponding vector control scheme for a three-phase machine [4], [5]. However, since vector control of an ac machine requires only two axis currents for decoupled flux and torque control, higher torque density can be achieved in a five-phase machine by utilizing the remaining two degrees of freedom. The injection of the third stator current harmonic enables utilization of the third spatial harmonic of the field for torque production, in addition to the fundamental harmonic of the field [2], [3].

A rather different use of these additional degrees of freedom was proposed in [5]. On the basis of considerations related to the machine's rotating field, it was suggested to connect two five-phase machines in series and supply them from a single five-phase source. By introducing an appropriate phase transposition in this series connection, it was reasoned that the two machines could be controlled completely independently, using basic vector control schemes, although they are supplied from the common five-phase source. The major advantage of such a two-motor drive system is the reduction OP the number of required inverter legs, when compared to an equivalent two-motor three-phase drive system (from six to five). This translates into increased reliability, due to a smaller number of components.

On the basis of this novel d-q axis model of the series-connected two-motor drive system, an indirect rotor flux oriented control scheme is designed.

A detailed simulation study is finally undertaken. The complete drive system, including the hysteresis current controllers and the voltage source inverter (VSI), is simulated for a number of transients. It is shown that completely decoupled flux and torque control results not only for each of the two machines, but for one machine with respect to the other as well. The correctness of the developed models and the vector control scheme are verified in this way.

A. Description of the drive

The drive consists of two five-phase machines, which can be either induction or synchronous (permanent magnet or synchronous reluctance) and which can be freely mixed within the system. It is here assumed that the machines in question are both induction motors, without any loss of generality. Five-phase stator windings of the two machines are connected in series, with an appropriate phase transposition, as illustrated in Fig. 1. Phase transposition in the series connection is a necessary prerequisite for independent vector control of the two control. Inverter phase sequence is denoted in Fig. 1 with capital letters A,B,C,D,E, while the phase sequence of the two machines, respecting the spatial distribution of the windings, is identified with lower case letters a,b,c,d,e. Spatial displacement between any two consecutive phases in the machines equals $\alpha = 2\pi/5$.

According to the connection diagram of Fig. 1, inverter phase-to-neutral voltages and the correlation between inverter output currents and machine phase currents are given with

$$\begin{aligned} v_A &= v_{as1} + v_{as2} \\ v_B &= v_{bs1} + v_{cs2} \\ v_C &= v_{cs1} + v_{es2} \\ v_D &= v_{ds1} + v_{bs2} \\ v_E &= v_{es1} + v_{ds2} \end{aligned} \quad (1)$$

$$\begin{aligned} i_A &= i_{as1} = i_{as2} \\ i_B &= i_{bs1} = i_{cs2} \\ i_C &= i_{cs1} = i_{es2} \\ i_D &= i_{ds1} = i_{bs2} \\ i_E &= i_{es1} = i_{ds2} \end{aligned} \quad (2)$$

It is assumed for modeling purposes that all the standard assumptions of the general theory of electrical machines apply [9], including the one related to sinusoidal distribution of the resulting field in the machine. Rotor windings are initially taken as five-phase as well, for the sake of generality.

B- DRIVE MODELING

B-1. Phase-Variable Model

Two machines of Fig. 1 are assumed to be of different parameters and ratings, for the sake of generality. The electrical subsystem's model of the drive in Fig.1 is of the 15th order and it can be represented in matrix form (underlined quantities) with

$$\underline{v} = \underline{R}\underline{i} + \frac{d(\underline{L}\underline{i})}{dt} \quad (3)$$

Where machines. Its purpose is to make flux/torque-producing currents of one machine non flux/torque-producing currents in the second machine, and vice versa [5]. The two-motor drive is supplied from a single five-phase VSI, which is current controlled. Current control is exercised upon phase currents in the stationary reference frame, using either hysteresis **or** ramp-comparison current

$$\underline{v} = \begin{bmatrix} \underline{v}^{INV} \\ \underline{0} \\ \underline{0} \end{bmatrix} \quad \underline{i} = \begin{bmatrix} \underline{i}^{INV} \\ \underline{i}_{r1} \\ \underline{i}_{r2} \end{bmatrix} \quad (4)$$

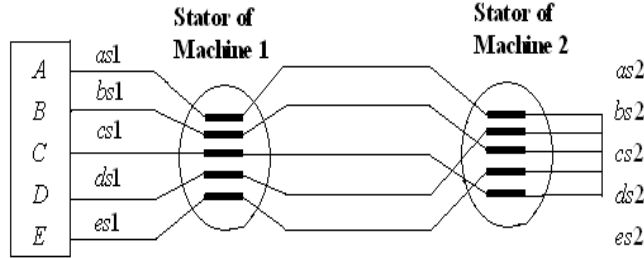


Fig.1: Five-phase two-motor drive with series connection of phase windings and an appropriate phase transposition.

$$\underline{v}^{INV} = [v_A \quad v_B \quad v_C \quad v_D \quad v_E]^T \quad (5)$$

$$\underline{i}^{INV} = [i_A \quad i_B \quad i_C \quad i_D \quad i_E]^T$$

$$\underline{R} = \begin{bmatrix} \underline{R}_{s1} + \underline{R}_{s2} & & \\ & \underline{R}_{r1} & \\ & & \underline{R}_{r2} \end{bmatrix} \quad (6)$$

$$\underline{L} = \begin{bmatrix} \underline{L}_{s1} + \underline{L}_{s2}' & \underline{L}_{sr1} & \underline{L}_{sr2}' \\ \underline{L}_{rs1} & \underline{L}_{r1} & \underline{0} \\ \underline{L}_{rs1}' & \underline{0} & \underline{L}_{r2} \end{bmatrix}$$

Sub-matrices of the inductance matrix identified with the prime symbol are those whose form has been altered through the phase transposition operation.

B.2. Decoupling transformation

Decoupling (Clark's) transformation matrix is applied first. Let the correlation between original phase variables and new (α, β) variables be given with $f_{-\alpha\beta} = \underline{C} f_{-abcde}$.

Where \underline{C} is the power-invariant transformation matrix [6]

$$\underline{C} = \begin{bmatrix} \alpha & 1 & \cos \alpha & \cos 2\alpha & \cos 3\alpha & \cos 4\alpha \\ \beta & 0 & \sin \alpha & \sin 2\alpha & \sin 3\alpha & \sin 4\alpha \\ x & 1 & \cos 2\alpha & \cos 4\alpha & \cos 6\alpha & \cos 8\alpha \\ y & 0 & \sin 2\alpha & \sin 4\alpha & \sin 6\alpha & \sin 8\alpha \\ 0 & 1/\sqrt{2} & 1/\sqrt{2} & 1/\sqrt{2} & 1/\sqrt{2} & 1/\sqrt{2} \end{bmatrix} \quad (7)$$

Application of (8) in conjunction with inverter voltages yields axis components of the inverter voltages

$$\begin{bmatrix} v_{\alpha}^{INV} \\ v_{\beta}^{INV} \\ v_x^{INV} \\ v_y^{INV} \\ v_0^{INV} \end{bmatrix} = \underline{C} \begin{bmatrix} v_A \\ v_B \\ v_C \\ v_D \\ v_E \end{bmatrix} \quad (8)$$

Which can be further expressed, using correlation (1), as functions of the voltage axis components of the two machines

$$\begin{bmatrix} v_{\alpha}^{INV} \\ v_{\beta}^{INV} \\ v_x^{INV} \\ v_y^{INV} \\ v_0^{INV} \end{bmatrix} = \underline{C} \begin{bmatrix} v_{as1} + v_{as2} \\ v_{bs1} + v_{cs2} \\ v_{cs1} + v_{es2} \\ v_{ds1} + v_{bs2} \\ v_{es1} + v_{ds2} \end{bmatrix} = \begin{bmatrix} v_{\alpha s1} + v_{xs2} \\ v_{\beta s1} - v_{ys2} \\ v_{xs1} + v_{\alpha s2} \\ v_{ys1} + v_{\beta s2} \\ 0 \end{bmatrix} \quad (9)$$

Due to the absence of the neutral conductor inverter zero sequence voltage components must equal zero. The correlation between inverter voltage axis components and individual machine's voltage axis components implies series connection between appropriate $\alpha - \beta$ and x-y circuits of the two machines. A corresponding correlation between inverter output currents and $\alpha - \beta$ and x-y current components of the two machines is obtained by using (8) in conjunction with (2).

$$\begin{aligned} i_{\alpha}^{INV} &= i_{\alpha s1} = i_{xs2} \\ i_{\beta}^{INV} &= i_{\beta s1} = -i_{ys2} \\ i_x^{INV} &= i_{xs1} = i_{\alpha s2} \\ i_y^{INV} &= i_{ys1} = i_{\beta s2} \end{aligned} \quad (10)$$

The zero sequence component is omitted due to the star connection of the system without neutral conductor.

B.3. Model in the Stationary Common Reference Frame

Upon application of the decoupling transformation matrix (9) onto inverter and rotor voltage equations of (3). Rotational transformation matrix, leading to the d-q system of equations, is applied in conjunction with rotor equations (angle θ is the instantaneous rotor position, which is different for the two machines:

$$\underline{D}_r = \begin{bmatrix} \cos \theta & -\sin \theta & & & \\ \sin \theta & \cos \theta & & & \\ & & 1 & & \\ & & & 1 & \\ & & & & 1 \end{bmatrix} \quad (11)$$

Since the stator-to-rotor coupling appears in $\alpha - \beta$ equations only and torque production' is entirely governed by $\alpha - \beta$ current (flux) components, rotational transformation is not applied to x-y rotor equations. As rotational transformation is applied to rotor windings only, indices α , β and d, q are interchangeable in inverter (stator) equations (8)-(10).

The resulting system model is in the stationary common reference frame and is in general of the 15th order. However, taking into account that rotor windings of the two machines are short-circuited, rotor x-y component equations and rotor zero sequence equation can be omitted from further consideration. Zero sequence component equation for the inverter can be omitted as well. The electro-magnetic part of the drive system can then be represented with eight first-order differential equations. The four inverter equations are

$$\begin{aligned} v_d^{INV} &= R_{s1}i_d^{INV} + (L_{ls1} + L_{m1})\frac{di_d^{INV}}{dt} + L_{m1}\frac{di_{dr1}}{dt} + R_{s2}i_d^{INV} + L_{ls2}\frac{di_d^{INV}}{dt} \\ v_q^{INV} &= R_{s1}i_q^{INV} + (L_{ls1} + L_{m1})\frac{di_q^{INV}}{dt} + L_{m1}\frac{di_{qr1}}{dt} + R_{s2}i_q^{INV} + L_{ls2}\frac{di_q^{INV}}{dt} \\ v_x^{INV} &= R_{s1}i_x^{INV} + L_{ls1}\frac{di_x^{INV}}{dt} + R_{s2}i_x^{INV} + (L_{ls2} + L_{m2})\frac{di_x^{INV}}{dt} + L_{m2}\frac{di_{dr2}}{dt} \\ v_y^{INV} &= R_{s1}i_y^{INV} + L_{ls1}\frac{di_y^{INV}}{dt} + R_{s2}i_y^{INV} + (L_{ls2} + L_{m2})\frac{di_y^{INV}}{dt} + L_{m2}\frac{di_{qr2}}{dt} \end{aligned} \quad (12)$$

Or, in terms of individual machine d-q **axis** stator voltage components (according to (9))

$$\begin{aligned} v_d^{INV} &= v_{ds1} + v_{xs2} \\ v_q^{INV} &= v_{qs1} - v_{ys2} \\ v_x^{INV} &= v_{xs1} + v_{ds2} \\ v_y^{INV} &= v_{ys1} + v_{qs2} \end{aligned} \quad (13)$$

Rotor voltage equilibrium equations of the two machines are:

$$\begin{aligned} 0 &= R_{r1}i_{dr1} + L_{m1}\frac{di_d^{INV}}{dt} + (L_{r1} + L_{m1})\frac{di_{dr1}}{dt} + \omega_1(L_{m1}i_q^{INV} + (L_{r1} + L_{m1})i_{qr1}) \\ 0 &= R_{r1}i_{qr1} + L_{m1}\frac{di_q^{INV}}{dt} + (L_{r1} + L_{m1})\frac{di_{qr1}}{dt} - \omega_1(L_{m1}i_d^{INV} + (L_{r1} + L_{m1})i_{dr1}) \\ 0 &= R_{r2}i_{dr2} + L_{m2}\frac{di_x^{INV}}{dt} + (L_{r2} + L_{m2})\frac{di_{dr2}}{dt} + \omega_2(L_{m2}i_y^{INV} + (L_{r2} + L_{m2})i_{qr2}) \\ 0 &= R_{r2}i_{qr2} + L_{m2}\frac{di_y^{INV}}{dt} + (L_{r2} + L_{m2})\frac{di_{qr2}}{dt} - \omega_2(L_{m2}i_x^{INV} + (L_{r2} + L_{m2})i_{dr2}) \end{aligned} \quad (14)$$

Finally, torque equations of the two series connected machines are given in terms of inverter current axis components with

$$\begin{aligned} C_{em1} &= P_1 L_{m1} \left[i_{dr1} i_q^{INV} - i_d^{INV} i_{qr1} \right] \\ C_{em2} &= P_2 L_{m2} \left[i_{dr2} i_y^{INV} - i_x^{INV} i_{qr2} \right] \end{aligned} \quad (15)$$

2. Design of sliding mode control

The sliding mode control is one of simplest approaches of the robust control. Very good performances (response time, precision) can be obtained in the presence of uncertainties on the parameters of the system and their variations on the one part, and uncertainties on the models of the system on the other part. These performances are obtained at the price of a very strong activity of order which can result in very strong oscillations called "Chattering". The design of the controllers by sliding mode takes into account the problems of stability and good performances in a systematic way in its approach, which is devised into three principal stages [6]:

- Choice of surfaces,
- Establishment of the conditions of existence and convergence,
- Determination of the law of control.

A.Choice of the surface of commutation

J.J. Slotine proposes a format general equation to determine sliding surface

$$s(x) = \left(\frac{d}{dt} + \lambda \right)^{n-1} e \tag{16}$$

$e = X_d - X$: Variation

λ : Positif coefficient

n: order of the system

X_d : Desired value

B.Condition of convergence

The condition of convergence is defined by the equation of Lyapunov. It makes surface attractive and invariant

$$s(x) \cdot \dot{s}(x) < 0$$

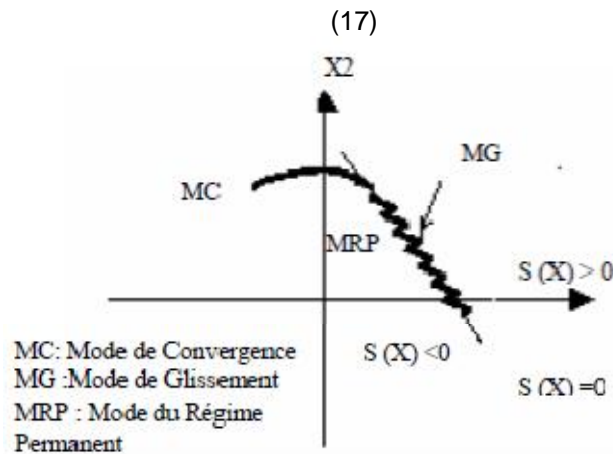


Fig. 2: Modes of trajectory in the plan of phase.

3.Sliding mode control of a Five-Phase Series-Connected Two-Motor Drive

If one chooses $n=1$, surfaces are written:

For the first machine:

$$\begin{cases} S(\Omega_{r1}) = \Omega_{r1ref} - \Omega_{r1} \\ S(\phi_{r1}) = \phi_{r1ref} - \phi_{r1} \\ S(i_{d1}^s) = i_{d1ref}^s - i_{d1}^s \\ S(i_{q1}^s) = i_{q1ref}^s - i_{q1}^s \end{cases} \tag{18}$$

For the second machine:

$$\begin{cases} S(\Omega_{r2}) = \Omega_{r2ref} - \Omega_{r2} \\ S(\phi_{r2}) = \phi_{r2ref} - \phi_{r2} \\ S(i_{d2}^s) = i_{d2ref}^s - i_{d2}^s \\ S(i_{q2}^s) = i_{q2ref}^s - i_{q2}^s \end{cases} \quad (19)$$

Decoupling resulting from the orientation of the rotor flow of the two machines enables us to control flow and speed separately, by using the current i_d^s for the control of flow and the current i_q^s for the speed control.

A. Application of the control to the first machine

Along the axe "d"

$$\dot{S}(\phi_{r1}) = 0 \Rightarrow \begin{cases} i_{d1n}^s = K_{\phi1} \text{sign}(S(\phi_{r1})) \\ i_{d1eq}^s = \frac{T_{r1}}{L_{m1}} \phi_{r1ref} + \frac{1}{L_{m1}} \phi_{r1} \end{cases} \quad (20)$$

And

$$\dot{S}(i_{d1}^s) = 0 \Rightarrow \begin{cases} V_{d1n}^s = K_{id1} \text{sign}(S(i_{d1}^s)) \\ V_{d1eq}^s = (\sigma_1 L_{s1} + L_{s2}) i_{d1ref}^s + R_{1d1} i_{d1}^s - (\sigma_1 L_{s1} + L_{s2}) \omega_{s1} i_{q1}^s - \frac{L_{m1}}{T_{r1} L_{r1}} \phi_{r1}^f \end{cases} \quad (21)$$

Along axe "q"

$$\dot{S}(\Omega_{r1}) = 0 \Rightarrow \begin{cases} i_{q1n}^s = K_{\Omega1} \text{sign}(S(\Omega_{r1})) \\ i_{q1eq}^s = \frac{J_1 \dot{\Omega}_{r1ref} + f_1 \Omega_{r1}}{p_1 \frac{L_{m1}}{L_{r1}} \phi_{r1}} \end{cases} \quad (22)$$

And

$$\dot{S}(i_{q1}^s) = 0 \Rightarrow \begin{cases} V_{q1n}^s = k_{iq1} \text{sign}(S(i_{q1}^s)) \\ V_{q1eq}^s = (\sigma_1 L_{s1} + L_{s2}) i_{q1ref}^s + R_{1q1} i_{q1}^s + (\sigma_1 L_{s1} + L_{s2}) \omega_{s1} i_{d1}^s + \frac{L_{m1}}{L_{r1}} \omega_{r1} \phi_{r1}^f \end{cases} \quad (23)$$

B. Application of the control to the second machine

Along the axe "d"

$$\begin{cases} i_{d2n}^s = K_{\phi2} \text{sign}(S(\phi_{r2})) \\ i_{d2eq}^s = \frac{T_{r2}}{L_{m2}} \phi_{r2ref} + \frac{1}{L_{m2}} \phi_{r2} \end{cases} \quad (24)$$

And

$$\begin{cases} V_{d2n}^s = K_{id2} \text{sign}(S(i_{d2}^s)) \\ V_{d2eq}^s = (\sigma_2 L_{s2} + L_{ls1}) i_{d2ref}^s + R_2 i_{d2}^s - (\sigma_2 L_{s2} + L_{ls1}) \omega_{s2} i_{q2}^s - \frac{L_{m2}}{T_{r2} L_{r2}} \phi_2^r \end{cases} \quad (25)$$

Along the axe "q"

$$\begin{cases} i_{q2n}^s = K_{\Omega 2} \text{sign}(S(\Omega_{r2})) \\ i_{q2eq}^s = \frac{J_2 \Omega_{r2ref} + f_2 \Omega_{r2}}{p_2 \frac{L_{m2}}{L_{r2}} \phi_{r2}} \end{cases} \quad (26)$$

And

$$\begin{cases} V_{q2n}^s = K_{\Omega 2} \text{sign}(S(i_{q2}^s)) \\ V_{q2eq}^s = (\sigma_2 L_{s2} + L_{ls1}) i_{q2ref}^s + R_2 i_{q2}^s + (\sigma_2 L_{s2} + L_{ls1}) \omega_{s2} i_{d2}^s + \frac{L_{m2}}{L_{r2}} \omega_{r2} \phi_2^r \end{cases} \quad (27)$$

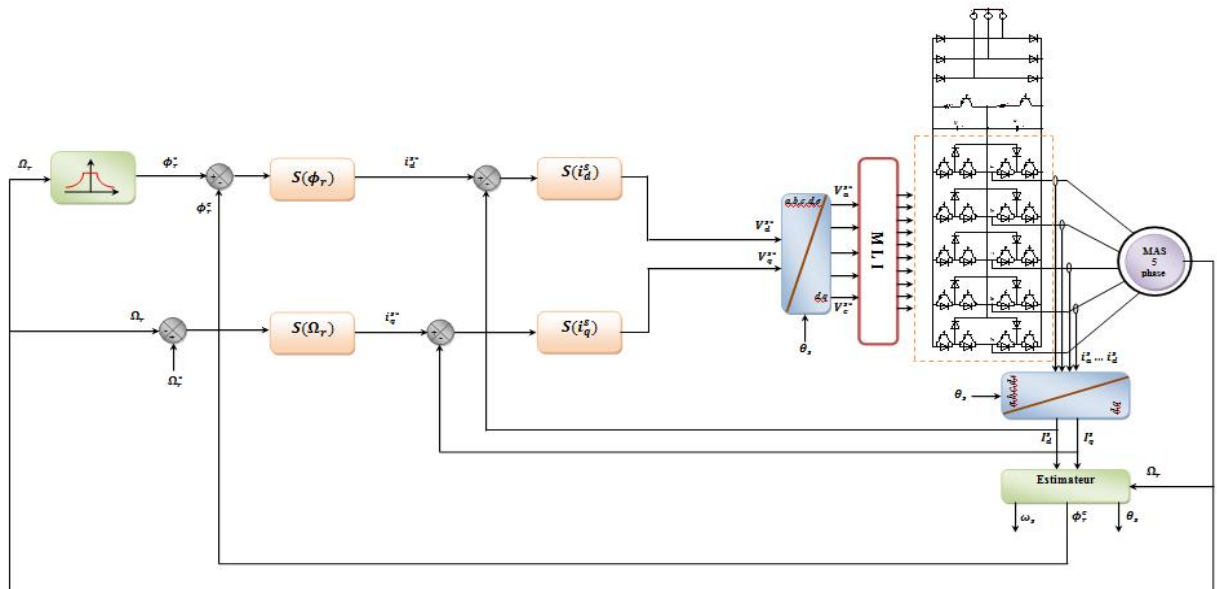


Fig .3: Sliding mode control of a Five-Phase Series-Connected Two-Motor Drive

4.Simulation results

The transposition of the phases allowed the independent control from two machines. we notice that the speed and rotor flux of two machines after a short transitory regime towards the compulsory references. During the application of the load at the moment $t=0.5s$, the speed decreases, then returns to its reference. we notice the same thing when the load is eliminated. The undulations of the couple are always due to the not sinusoidal shape of the tension of exit of the inverter.

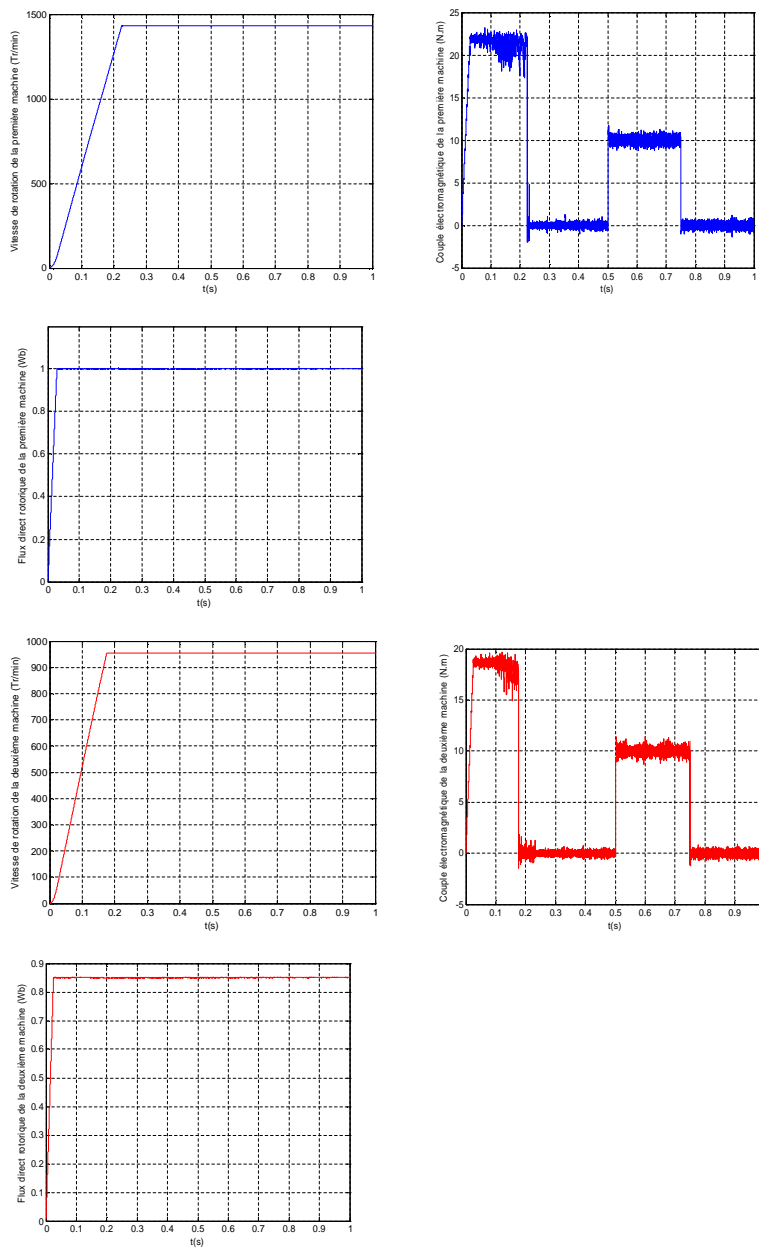


Fig.4: Simulation results of the Sliding mode control of a Five-Phase Series-Connected Two-Motor Drive

5. Conclusion

The results of simulation showed the importance of the transposition of phases applied for the independent control from two machines. We noticed that the use of regulators "sliding mode" improved the answer of the machine, better than during the use of regulators PI, we supposed that the parameters do not vary, what is not the case in practice, the parameters of machines vary either by heating or by saturation, these variations influence directly the variables of exit of the control.

Acknowledgements

I would like to thank my advisor Lazhari Nezli for her constant support, suggestions and scientific guidance during all stages of my work.

References

- [1] E.Semail, E.Levi, A.Bouscayrol, X.Kestelyn: Multi-machine modeling of two series connected five-phase synchronous machines: affect of harmonics on control, IEEE-IAS'04, Seattle (Washington), October 2004, Vol.1, pp.71-78.
- [2] H.A.Toliyat, H.Xu, L.J.Petersen: Five-phase induction motor drives with DSP-based control system », IEEE Transactions on Power Electronics, Vol.17, N° 4, July 2002, pp.524-533.
- [3] E.Levi, M.Jones, S.N.Vukosavic, H.A.Toliyat: A novel concept of a multiphase, multi-motor vector controlled drive system supplied from a single voltage source inverter », IEEE [Lip-80]:
- [4]. C.Namuduri and P.C. Sen "A servo control system using a self controlled synchronous motor (SCSM) with sliding mode controller" IEEE IAS Annual Meeting 1986 pp56-65
- [5] E.Levi, M.Jones, S.N.Vukosavic, H.A.Toliyat, A.Iqbal: Modelling, control and experimental investigation of a five-phase series-connected two-motor drive with single inverter supply, IEEE Trans. Energy Convers, 2006.
- [6]T.A.Lipo: A d-q model for six phase induction machines , proc. ICEM'80, pp.860-867, Athens, Greece, 1980 Trans. Power Electronics, vol. 19, pp. 320-335, 2004.

People's Democratic Republic of Algeria
Ministry of Higher Education and Scientific research
M'hamed Bougara University, Boumerdes
Institute of Electrical and Electronic Engineering,
Laboratory of Signals and Systems (LSS)



ALGERIAN JOURNAL OF SIGNALS AND SYSTEMS

ISSN : 2543-3792

Title: Design and Evaluation of a DSP Based Differential Relay of Power Transformer

Authors: A. Abdelmoumene, R.Bouderbala, H.Bentarzi

Affiliation: Signals and Systems Laboratory, IGEE, University of M'hamed Bougara, Boumerdes, Algeria.

Page range: 69- 78

IMPORTANT NOTICE

This article is a publication of the Algerian journal of Signals and Systems and is protected by the copyright agreement signed by the authors prior to its publication. This copy is sent to the author for non-commercial research and education use, including for instruction at the author's institution, sharing with colleagues and providing to institution administration. Other uses, namely reproduction and distribution, selling copies, or posting to personal, institutional or third party websites are not allowed.

Volume : 1 Issue : 1 (June 2016)

Laboratory of Signals and Systems

Address : IGEE (Ex-INELEC), Boumerdes University, Avenue de l'indépendance, 35000, Boumerdes, Algeria

Phone/Fax : 024 79 57 66

Email : lss@univ-boumerdes.dz ; ajsyssig@gmail.com

Design and Evaluation of a DSP Based Differential Relay of Power Transformer

Abdelkader ABDELMOUMENE, Rachid BOUDERBALA, and Hamid BENTARZI*

Signals and Systems Laboratory, IGEE, University of M'hamed Bougara, Boumerdes, Algeria

Abstract: The problem of mal operation of differential protection of power transformer due to the inrush magnetizing current has long considered as a challenging problem. Several types of protection relays have been used to solve the issue (basic relay, percentage relay, multi slop ...). Each of them has its advantage and its limits.

In this paper, a Digital differential relay has been developed and simulated. The logic used to distinguish between the inrush current and the internal fault is based on the theory of harmonic analysis. The behavior of the presented relay has been simulated versus various situations (inrush current, internal fault and external fault). The obtained results show that the proposed algorithm provides a good discrimination and a fast action.

Keywords: Algorithm, Differential, DSP, Digital, power transformer, harmonic analysis.

1. INTRODUCTION

One of the most important and expansive element in power systems is the power transformer, which is used in different sizes, types, and connections. A power transformer functions as a node to connect two (02) different voltage levels. Therefore, the continuity of its operation is of vital importance in maintaining the reliability of power supply [1, 2]. However, transformers are expected to many internal and external stresses and the consequence of any failure can be very heavy in term of damage as well as in terms of operating losses [3]. So a performing and secure protection is needed.

Differential protection is widely used to protect large power transformer against internal faults. Its principle of operation is based on the fact that if the difference between the entering and the leaving currents in the protected zone exceed a predetermined value; the relay transmits a trip signal to the circuit breaker and isolates the faulted zone.

Based on this principle, the relay must operate when, and only when, an internal fault occurs. However, certain phenomena (such as inrush current, CT saturation levels,

nonlinearities...) in power transformer can create a differential current between its two terminals, even without internal fault, causing thus mal tripping.

When a transformer is energized, magnetizing inrush current that flows in one set of terminals may equal many times the transformer rating [4]. This is the most challenging problem in power transformer differential protection.

Over the years, many different methods of preventing differential relay operation on inrush have been utilized [5]:

- **Deactivate the relay:** since the magnetizing current has a damped nature, the simple way to avoid the mal tripping at the energizing moment was the deactivation of the relay until the death (disappearance) of the inrush current.
- **Decrease the acting speed:** Use slow-speed induction-type relays with long time and high current settings.

- **Power differential method:** This method is based on the idea that the average power drawn by a power transformer is almost zero on inrush, while during a fault the average power is significantly higher [5,6].
- **Rectifier relay :** This method takes advantage of the fact that magnetizing inrush current is in effect a half-frequency wave. Relays based on this method use rectifiers and have one element functioning on positive current and one on negative current. Both elements must operate in order to produce a trip. On inrush, the expectation is that one element only will operate, while on an internal fault, the waveform will be sinusoidal and both elements will operate. [5] [7]
- **Methods based on inrush current analysis:** Waveform recognition, wavelet transform, harmonic analysis...

In this paper, we propose an algorithm for digital differential relay based on the detection of the second harmonic component to discriminate between the false differential current at the energizing moment of power transformer and that causing by a real internal fault.

The first part of the paper is devoted to the description of the traditional differential relays, the DSP (Digital Signal Processing) based relay and the proposed algorithm. In the second part, simulations of the relay's behavior in several cases have been done and interpreted.

2. OPERATING PRINCIPLE OF TRADITIONAL DIFFERENTIAL RELAY

The basic scheme of the power transformer differential protection is shown in figure.1.

Differential relay compares the currents that enter with the currents that leave the protected zone. If the differential current (called also operating current I_{op}) is essentially zero, it is concluded that there is no fault in the protection zone. However, if operating current is not zero, the differential protection concludes that a fault exists in the zone and takes steps to isolate the zone from the rest of the system [8].

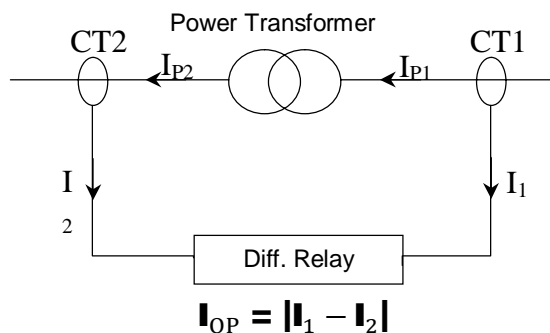


Fig.1 Typical Differential Relay Connection Diagram

The operating current in the differential relay is equal to:

$$I_{OP} = |I_1 - I_2| \quad (1)$$

If:

$I_{OP} = 0 \Rightarrow$ No internal fault.

$I_{OP} \neq 0 \Rightarrow$ An internal fault occurs.

Theoretically, the differential relay performs well as long as we consider that the behaviors of the CTs and the power transformer are ideals (no saturation of the magnetic circuit, no inrush current, no iron losses...).

In fact, the basic differential relay may operate incorrectly due to:

- Magnetizing inrush current
- Current transformer saturation
- Overexcitation conditions
- On-Load Tap-Changer (OLTC).

To do face against the weakness points of mal tripping causing by the phenomena cited above (previously) – except the problem of inrush current – the percentage restraint differential protective relay have been used for many years.

Percentage restrain relays employ a restraining current. The following are the most common ways to obtain the restraint current [9]:

$$I_{RT} = k \left| \vec{I}_1 - \vec{I}_2 \right|$$

$$I_{RT} = k \left(\left| \vec{I}_1 \right| + \left| \vec{I}_2 \right| \right)$$

$$I_{RT} = \text{Max} \left(\left| \vec{I}_1 \right|, \left| \vec{I}_2 \right| \right)$$

Where k is a compensation factor, generally taken as 0.5 or 1.

The differential relay generates a tripping signal if the operating current, I_{OP} , is greater than a percentage of the restraining current, I_{RT} :

$$I_{OP} > SLP \cdot I_{RT}$$

Figure.2 represents the operating characteristics of such relay. This characteristic consists of a line divides the coordinate plane in two parts. The upper part is the operating region while the lower part is the restraining region.

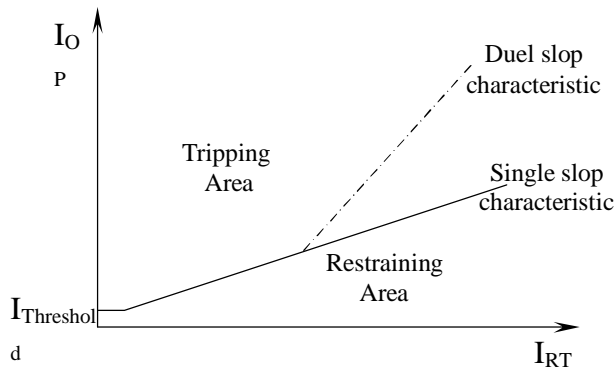


Fig.2 Characteristic of a percentage differential relay

3. DSP BASED RELAY

DSP based relay consists of the following main subsystems:

- Analog input subsystem,
- Analog and digital output subsystem,
- Analog to digital and digital to analog conversion subsystems,
- Processor.

The relay receives input currents via CTs from each phase of the power transformer. This analog signal is pre-processed using low pass filters to avoid aliasing effect. This later is passed through

an Analog to Digital Converter (ADC) because the processor can handle only numerical (logical) data. The digitized signal is processed in a Digital processor according to the algorithm implemented in its software. In the light of the processing results, a decision signals may be issued to the concerned organs (Circuit breaker, signalization, communication.....).

Figure.3 represents the general aspect of a DSP based Relay.

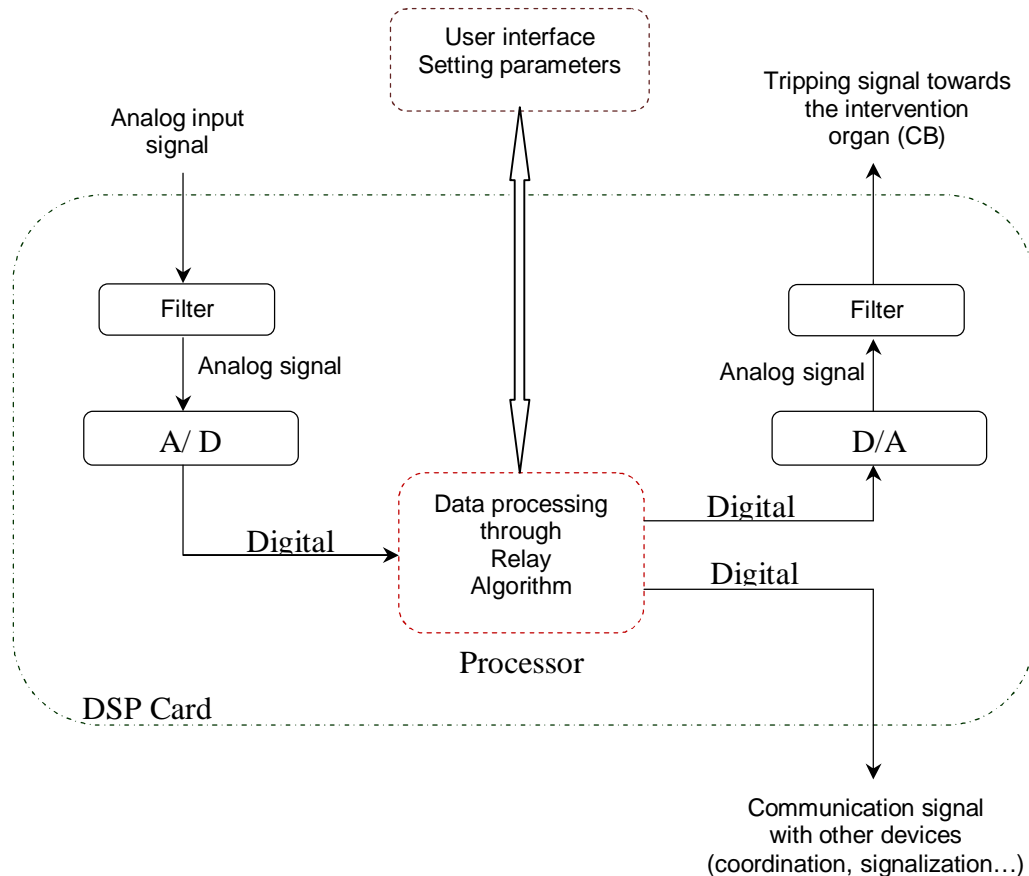


Fig.3: Block diagram of typical DSP based relay

4. THE PROPOSED ALGORITHM

The proposed algorithm is relied on the fact that the magnetizing inrush currents are characterized by having high second harmonic content [10]. While this character is not notified in the case of internal or external faults.

Research studies have found that the second harmonic component compared with the fundamental, in the case of inrush current, is somewhere between 30 % and 70 % [10-12].

To achieve the harmonic analysis of the differential current, the FFT (Fast Fourier Transform) has been used. FFT is a powerful mathematical tool that helps to extract the fundamental and higher harmonic components from the differential signal:

$$i(t) = \frac{a_0}{2} + \sum_{k=1}^{\infty} (C_k \cos(k\omega t) + S_k \sin(k\omega t))$$

a_0 : is the DC component.

C_k : Fourier cosine coefficient.

S_k : Fourier sine coefficient.

The discrete forms of the cosine and sine coefficients can be expressed as follow:

$$C_k = \frac{2}{N} \sum_{n=1}^{N-1} X(n) \cos\left(\frac{2k\omega t}{N}\right)$$

$$S_k = \frac{2}{N} \sum_{n=1}^{N-1} X(n) \sin\left(\frac{2k\omega t}{N}\right)$$

$X(n)$: is the current $i(t)$ in its discrete form.

The Fourier harmonic coefficients are given by:

$$F_k = \sqrt{S_k^2 + C_k^2}$$

F_k : is the k^{th} harmonic coefficient for $k=1,2,\dots,N$.

The flow chart of the developed algorithm is shown in figure.4.

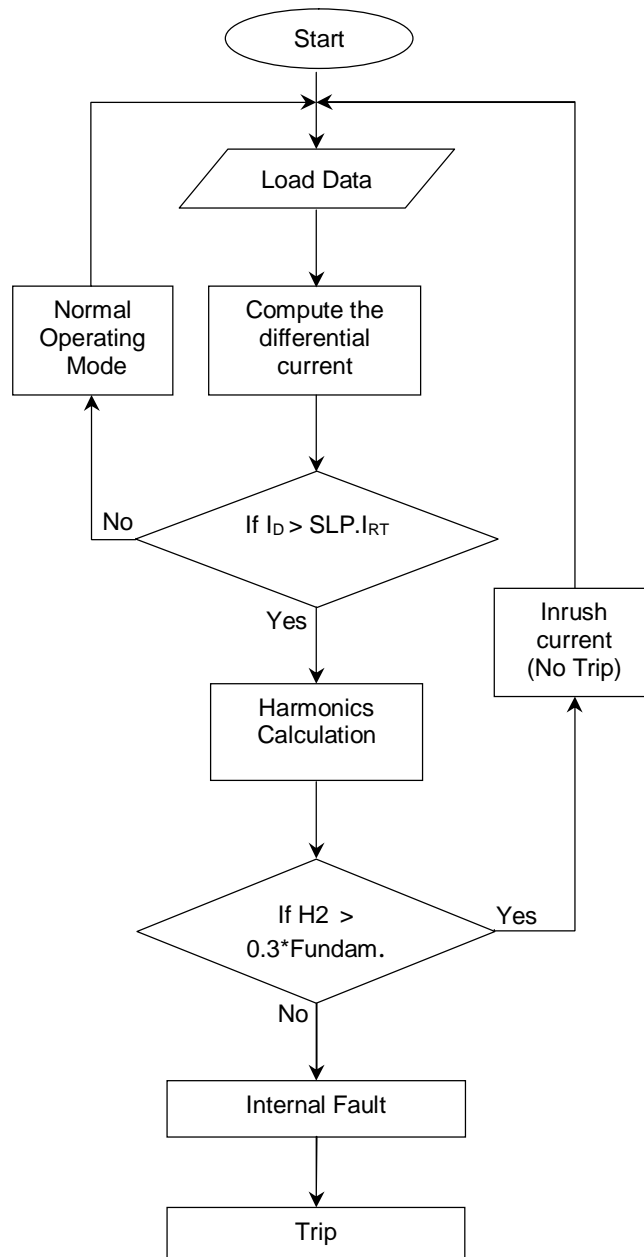


Fig.4: Flow chart of the proposed algorithm.

First, the relay loads the setting parameters and reads data from CTs, then it calculate the difference of current, I_D , between the primary and the secondary sides of the power transformer. If the differential current is less than the threshold; the situation is classed as a normal operating mode. Otherwise, two cases are possible: an internal fault or a magnetizing inrush current.

To discriminate between these phenomena, the relay must make a second test based on harmonic analysis (fact that the magnetizing inrush current is specified by high harmonic components content that have not significant presence in fault currents. So it proceeds to the harmonic analysis and compare the second harmonic with the fundamental. If the test is satisfied (2^{nd} Harmonic is greater than 30 % of the fundamental) this means that the remarked differential current is due to the energizing inrush current, and consequently the relay must not release the tripping signal.

If the second condition is not satisfied, the relay recognizes an internal fault and releases a trip signal to isolate the transformer.

5. SIMULATIONS AND RESULTS

The proposed algorithm has been implemented using Matlab/Simulink packages. As the software MatLab and Simulink presently do not have a toolbox which helps us in simulating power system protective devices, we have built a model for the differential relay according to the logic discussed in the above cited algorithm.

The simulations presented in this paper is performed on a step-down three-phase power transformer 250 MVA rated power; the primary and the secondary line to line voltages were 230kV \ 63 kV respectively.

To prove the effectiveness of (the proposed algorithm) developed relay, we have simulated the behavior of the relay versus three essential cases:

- Behavior of the relay versus the magnetizing inrush current.
- Behavior of the relay versus an internal fault.
- Behavior of the relay versus an external fault.

A. *The first case:* magnetizing inrush current

The magnetizing inrush current occurs each time when the transformer is energized. Figure 5 represents the result of simulation of the primary current (phase A).

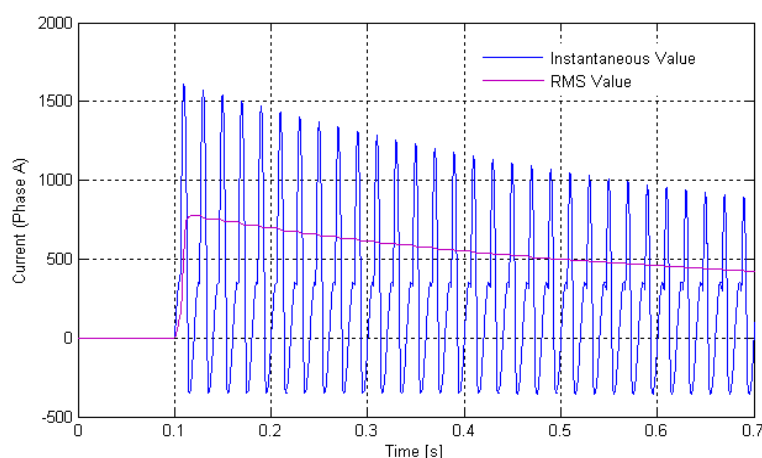


Fig.5: Inrush current resulted following the energizing of the transformer.

Since the inrush current appears mainly in the primary side of the transformer, the currents caught by the CTs at the transformer terminals are greatly different. Consequently, the relay detects a differential current (see figure.6).

This inrush current usually causes mal operation of traditional differential relays. Furthermore, the disconnection of the transformer during the inrush phenomenon may be very dangerous (a considerable overvoltage can be generated and leads to micro-dielectric breakdown of the transformer insulation).

That is why in our algorithm, after the detection of the differential current, a second condition (based on harmonic analysis) is added for best discrimination between the differential current caused by the inrush situation and that caused by internal fault.

Figure.6 shows that the second harmonic is greater than 30% of the fundamental. Hence, this blocks the relay to generate the trip signal (fig.6).

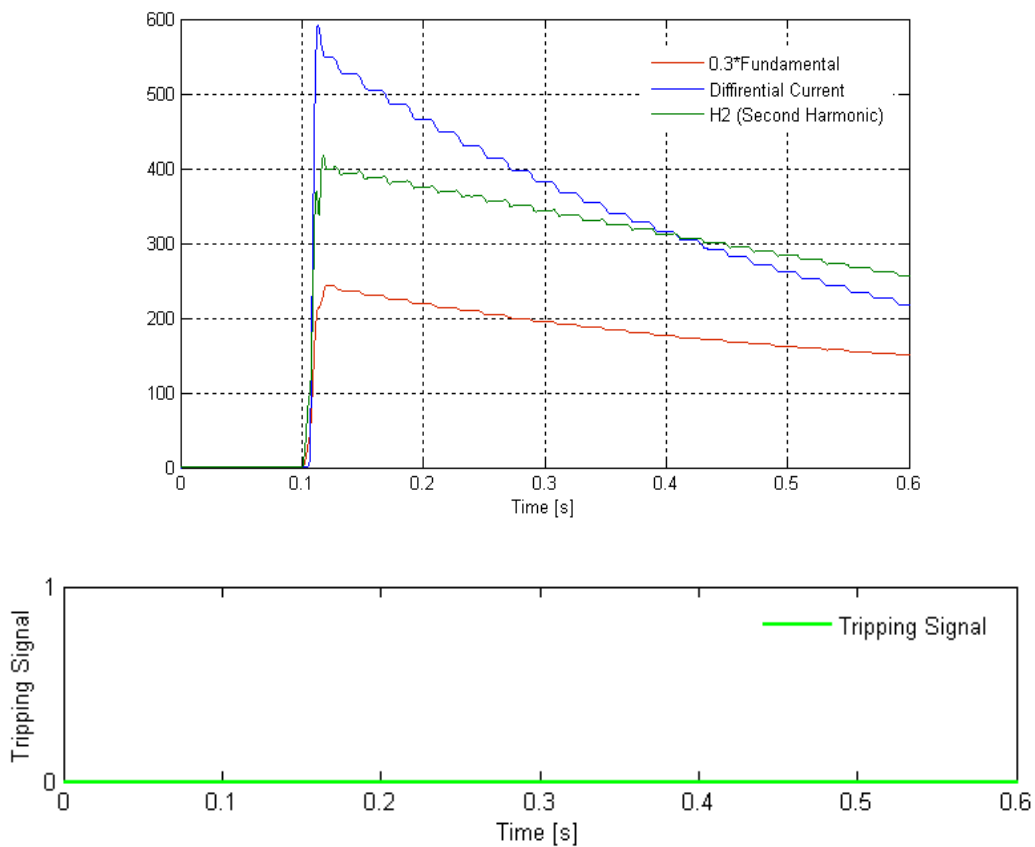


Fig.6: Simulation results in the case of magnetizing inrush current.

B. The second case: Internal fault

At $t = 4s$, an internal fault, between phase A and the ground, is created at the secondary side of the transformer. The simulation results (figure.7) show that the relay detects an important differential current. At this point, two cases are possible: inrush current or internal fault. Therefore, the relay must proceed to harmonic analysis to decide whether a tripping signal is needed or not. As the second harmonic is significantly less than 30% of the fundamental, the first case is eliminated and a decision to trip is carried out.

It should be noted also that the acting time of the relay is just 21 milliseconds which is considerably lower than the maximum acceptable time (100 msec) specified by IEEE standard for transformer protection, Thing which proves the fast character of the proposed algorithm.

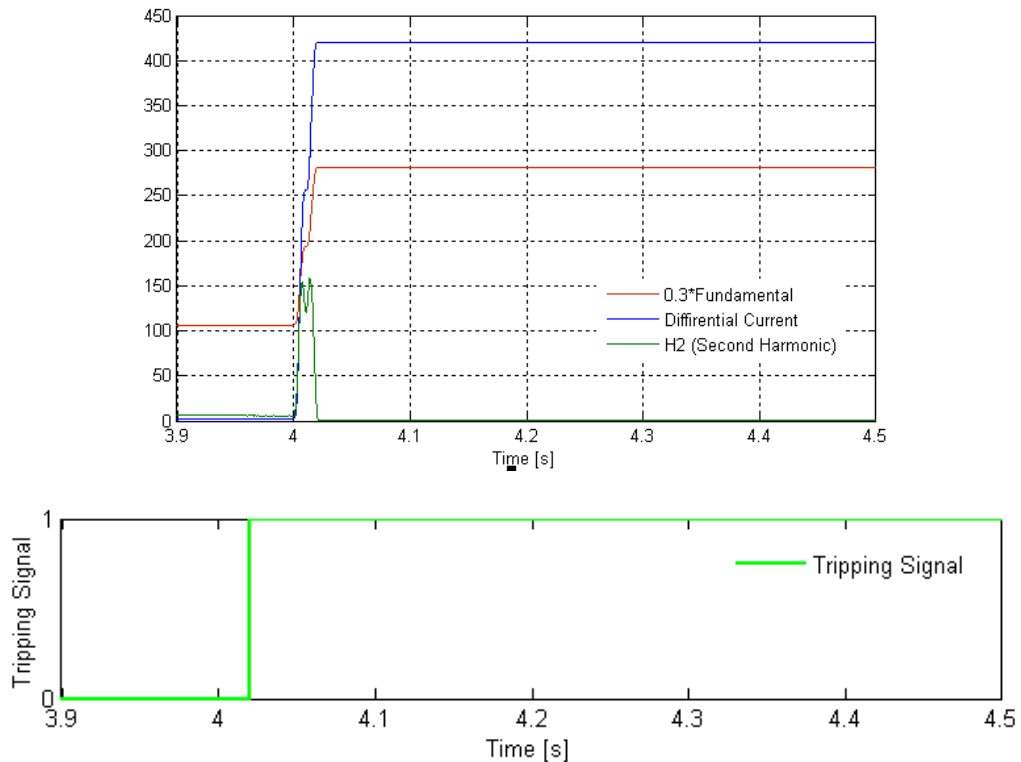


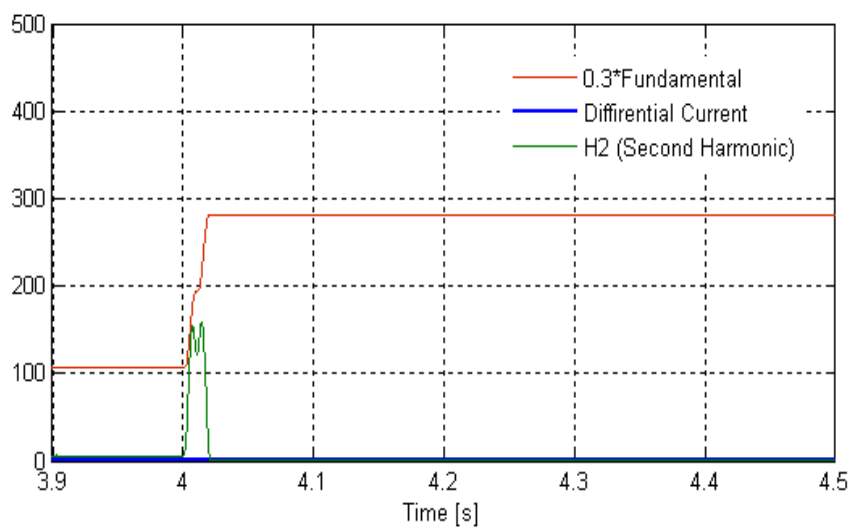
Fig.7: Simulation results in the case of Internal fault.

C. The third case: External fault

In this case, an external fault, between phase A and the ground, is simulated at the secondary side of the transformer.

The results of simulation are shown in figure.8.

No differential current is detected, no matter for the relay because the fault is occurred outside the responsibility area of the differential relay.



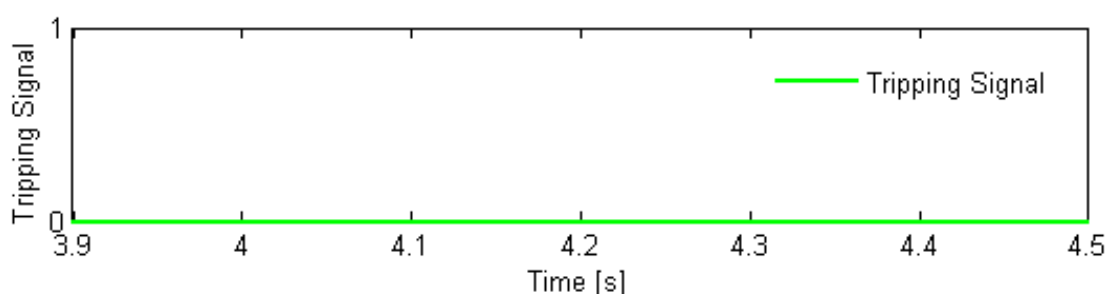


Fig.8: Simulation results in the case of external fault.

6. CONCLUSIONS

In this paper, a DSP based differential relay for large power transformer has been implemented and simulated. The proposed algorithm is based on the theory of harmonic analysis to discriminate between the internal fault and the inrush current created during the switching of the power transformer.

As Matlab \ Simulink lacks a toolbox that helps us in simulating protective devices; we have developed our own Relay's model. The simulation results of the proposed differential relay gave very satisfactory results in term of discrimination as well as in term of rapidity (operating time).

The success of such algorithm for digital relays allows reducing the complexity of traditional relays with more accurate results, higher reliability and less cost.

7. ACKNOWLEDGMENT

Authors acknowledge the immense help received from the scholars whose articles are cited and included in references of this manuscript. The authors are also grateful to authors / editors / publishers of all those articles, journals and books from where the literature for this article has been reviewed and discussed.

8. REFERENCES

- [1] Hassan KHORASHADI-ZADEH, Zuyi LI, "A sensitive ANN based differential relay for transformer protection with Security against CT Saturation and Tap Changer Operation", Turk J Elec Engin, VOL.15, NO.3 2007.
- [2] H. Khorashadi Zadeh, S. Hosseini Naveh, S. Irannejad, B.T. Hosseini, "An ANN Based Differential Transformer Protection", proceeding of the australasian universities power engineering conference AUPEC 2005.
- [3] A. ABDELMOUMENE and H. BENTARZI, "Reliability Enhancement of Power Transformer Protection System," Journal of Basic and Applied Scientific Research (J. Basic. Appl. Sci. Res., 2(10)10534-10539, 2012).
- [4] IEEE Std C37.91-2000, "IEEE guide for protective relay applications to power transformer", 2000.
- [5] Russell W. Patterson, Walter P. McCannon, Gary L. Kobet, "A Consideration of Inrush Restraint Methods in Transformer Differential Relays", the54th Annual Georgia Tech Protective Relaying Conference, 2000.
- [6] Yabe, K., "Power Differential Method for Discrimination between Fault and Magnetizing Inrush Current in Transformers", IEEE Transactions on Power Delivery, Vol. 12, No. 3, July 1997.
- [7] Michelson, E.L., "Rectifier Relay for Transformer Protection", AIEE Transactions, Volume 64, May 1945

- [8] Sandro G. Aquiles Perez, PhD thesis entitled: "MODELING RELAYS FOR POWER SYSTEM PROTECTION STUDIES", University of Saskatchewan, Canada, 2006.
- [9] IEEE, Guide for Protecting Power Transformers, 2008.
- [10] A.H Hana, N. S. Noorpi, M. Amirruddin and M.M. Nurhakimah, "Simulation Analysis of Harmonic Content of Transient Current During Sympathetic Inrush Current", 1st International Conference on Future Trends in Computing and Communication Technologies, 2012.
- [11] M.S. El-Bages, "Improvement of Digital Differential Relay Sensitivity For Internal Ground Faults In Power Transformers", International Journal on Technical and Physical Problems of Engineering , Vol. 3, No. 3, Sep. 2011.
- [12] Nikhil Mallikarjun And Devdutta Sahoo,"Transient Harmonic Analysis of Transformer", Department Of Electrical Engineering, National Institute of Technology, Rourkela, 2009.

People's Democratic Republic of Algeria
Ministry of Higher Education and Scientific research
M'hamed Bougara University, Boumerdes
Institute of Electrical and Electronic Engineering,
Laboratory of Signals and Systems (LSS)



ALGERIAN JOURNAL OF SIGNALS AND SYSTEMS

ISSN : 2543-3792

Title: Fast Ensemble Empirical Mode Decomposition Using the Savitzky Golay Filter

Authors: Wahiba Mohguen and Raïs El'hadi Bekka

Affiliation: Department of Electronics, LIS Laboratory Faculty of Technology, Université de Sétif 1, 19000 Sétif, Algeria.

Page range: 79- 86

IMPORTANT NOTICE

This article is a publication of the Algerian journal of Signals and Systems and is protected by the copyright agreement signed by the authors prior to its publication. This copy is sent to the author for non-commercial research and education use, including for instruction at the author's institution, sharing with colleagues and providing to institution administration. Other uses, namely reproduction and distribution, selling copies, or posting to personal, institutional or third party websites are not allowed.

Volume : 1 Issue : 1 (June 2016)

Laboratory of Signals and Systems

Address : IGEE (Ex-INELEC), Boumerdes University, Avenue de l'indépendance, 35000, Boumerdes, Algeria

Phone/Fax : 024 79 57 66

Email : lss@univ-boumerdes.dz ; ajsyssig@gmail.com

Fast Ensemble Empirical Mode Decomposition Using the Savitzky Golay filter

WAHIBA MOHGUEN AND RAÏS EL'HADI BEKKA*

Department of Electronics, LIS Laboratory
Faculty of Technology, Université de Sétif 1
19000 Sétif, Algeria
*bekka_re@yahoo.fr

Abstract: Empirical mode decomposition (EMD) is a powerful algorithm proposed to analysis of nonlinear and non-stationary signals. The phenomenon of mode mixing is one of the major disadvantages of the EMD. The Ensemble EMD (EEMD) was introduced to eliminate the mode-mixing effect. The principle of EEMD is to add additional white noise into the signal with many trials. The noise in each trial is different; and the added noise can be completely cancelled out on average, if the number of trials is very high. The number of trials is a high computational load. The improvement on computational efficiency of EEMD is therefore required. In this paper, an improvement on the computing time of the EEMD was proposed by replacing white noise with white noise filtered using Savitzky-Golay (SG) filter. Numerical simulations were performed to demonstrate that such replacement has effectively reduced the number of trials to obtain a noise-free reconstructed signal.

Keywords: EMD, EEMD, Mode mixing, Savitzky-Golay filter.

1. INTRODUCTION

The Empirical Mode Decomposition (EMD) method was introduced by Huang et al. [1] for the analysis of non stationary and/or nonlinear signals. The EMD was designed to adaptively decompose a signal into a set of intrinsic mode functions (IMFs) using a sifting process. One of the major drawbacks of the original EMD is the phenomenon of mode mixing which is defined by the coexistence of oscillations of different time scales in a single IMF or existence of the same oscillation with the same time scale in different IMFs [2]. Mode mixing is often produced by signal intermittent. To overcome the mode mixing problem, a noise assisted data analysis method called the ensemble empirical mode decomposition (EEMD) was recently developed by Wu and Huang [2]. The principle of EEMD is to add white noise into the signal with an ensemble of trials and the mixed signals are repeatedly decomposed by EMD. EEMD defines the true IMF components as the mean of an ensemble of trials, each consisting of the signal plus a white noise of finite amplitude. Indeed, EEMD achieves a significant improvement over the original EMD method for eliminating the mode mixing problem. But theoretically, the added noise can be completely cancelled out on average, if the number of trials would be infinite. Therefore, the very high number of ensemble trails to eliminate the residue noise in the signal reconstruction is synonymous with the very high computational cost. In order to improve the efficiency of the EEMD algorithm, many approaches were proposed [3]-[9].

Yeh et al. [3] expanded the EEMD method into complementary EEMD (CEEMD) by using both positive and negative white noise to the original data (i.e. one positive and one negative) to generate two sets of ensemble IMFs. CEEMD has effectively eliminated residue noise in the IMFs. However, a larger number of ensemble trials are also necessary to yield the root-mean-square (RMS) noise of CEEMD comparable to that of EEMD. Recently, Zheng et al. [4] modified the CEEMD method and developed a faster noise-assisted method called partly ensemble empirical mode decomposition (PEEMD) by performing the original EMD method on the noise signal obtained by an ensemble way and detected by permutation entropy. Although an important

improvement in computation time was achieved by PEEMD, the determination of the permutation entropy threshold is not adaptive and tough.

Zhang et al. [5] proposed a modified EEMD (MEEMD) method to reduce the computational cost of the original EEMD by replacing white noise with a band-limited noise to be added to the signal to be decomposed. But, this improvement is not significant. Recently, a sensitive improvement over the MEEMD was achieved with the right choice of the filter type and its characteristics [6].

A complete ensemble empirical mode decomposition with Adaptive Noise (CEEMDAN) was developed by Torres et al. [7]. In this method, a particular noise was added at each stage of the decomposition and a unique residue was computed to obtain each IMF, and achieved a complete decomposition with no reconstruction error. The CEEMDAN method requires less than half the sifting iterations that EEMD does.

Bekka and Berrouche [8] showed that a significant reduction for the computational complexity in EEMD can be obtained by over-sampling the original signal to reduce the ensemble trials. For very high-frequency signals, this method can lead to physically unrealizable sampling frequencies.

Very recently, an adaptively fast EEMD method combined with complementary EEMD was proposed by Xue, et al. [9] to resolve the problem of high computational cost.

In this paper an improved EEMD method, namely SGEEMD, was proposed. In this method, a significant improvement of computational efficiency was obtained with a white noise filtered using Savitzky-Golay (SG) filter. Numerical evaluation on a test signal showed the effectiveness of the SGEEMD method. A comparative study with the original EEMD showed that the proposed method allowed reducing the computation time by approximately 90%.

2. EMD AND EEMD ALGORITHMS

EMD Algorithm

EMD is an adaptive method to decompose a signal $x(t)$ into a set of IMFs. The IMFs must satisfy the following two conditions:

- (1) The number of maximum must equal the number of zeros or differ at most by one.
- (2) In each period, it is necessary that the signal average is zero.

The EMD algorithm (the sifting process of extracting IMFs) consists of the following steps [1]:

1. Identify local maxima and minima in $x(t)$ to construct the upper and lower envelopes respectively using cubic spline interpolation.
2. Calculate the mean envelope, $m(t)$, by averaging the upper and lower envelopes.
3. Calculate the temporary local oscillation $h(t) = x(t) - m(t)$.
4. Calculate the average of $h(t)$, if average is close to zero, then $h(t)$ is considered as the first IMF, named $IMF_1(t)$, otherwise, repeat steps (1)–(3) while using $h(t)$ for $x(t)$.
5. Calculate the residue $r(t) = x(t) - c_i(t)$.
6. Repeat the procedure from steps (1) to (5) using $r(t)$ for $x(t)$ to obtain the next IMF and residue.

The decomposition process stops when the residue $r(t)$ becomes a monotonic function or a constant that no longer satisfies the conditions of an IMF.

$$x(t) = \sum_{i=1}^N IMF_i(t) + r_N(t) \quad (1)$$

The sifting process is continued until the last residual is either a monotonic function or a constant.

EEMD Algorithm

The true IMFs in the EEMD are defined as the mean of an ensemble of trials. Each trial consists of the signal and the added white noise of finite amplitude. This noisy signal is then decomposed by EMD into noisy IMFs. In fact, the true IMFs are obtained by averaging the IMFs of the same order. Since the noise in each trial is different from other trials, noise added to the true IMFs is canceled out in the ensemble mean of relatively large number of trials [3]. For a number of ensemble trials given N_t , the EEMD algorithm consists of the following steps [2]:

1. Add a white noise $n(t)$ to the target signal $x(t)$: $x_j(t) = x(t) + n_j(t)$, $1 \leq j \leq N_t$
2. Decompose the noisy signal $x_j(t)$ by EMD algorithm into IMFs.
3. Repeat step 1 and step 2 until the end of number of ensemble trials, but with different added white noise each time.
4. Estimate the true IMFs of EEMD noted IMF_{iEEMD} by averaging the IMFs of the same order:

$$IMF_{iEEMD}(t) = \frac{1}{N_t} \sum_{j=1}^{N_t} IMF_j(t), \quad 1 \leq i \leq N \quad (2)$$

where N denotes the IMF number.

In the SGEEMD algorithm, $n(t)$ is replaced par $n_{SG}(t)$: a white noise filtered by Savitzky-Golay (SG) filter.

3. SG FILTER

The data smoothing is to replace each data point by some kind of local average of surrounding data points. The averaging can reduce the level of noise without biasing the value obtained. In this work a particular type of low-pass filter, well-adapted for data smoothing termed Savitzky-Golay filter was used to eliminate the residue noise by assuming that relatively distant data points have some important redundancy that can be used to reduce the level of noise.

Given N samples of a white noise $\eta(n)$ ($\eta(0), \eta(1), \dots, \eta(N-1)$) and a window size of $2M+1$ points (frame size) centered at the central point of the interval, the smoothed value of $\eta(i)$ by Savitzky-Golay filter is given by:

$$c(i) = \sum_{j=-M}^{M_t} g(j)\eta(i+j) \quad (3)$$

where $g(j)$ are filter coefficients.

$\hat{c}(i)$ is the average of the data points $\eta(i-M), \dots, \eta(-1), \eta(0), \eta(1), \dots, \eta(i+M)$. The concept of Savitzky-Golay filtering is to find the coefficients $g(j)$ that preserve higher moments within the moving window by a higher order polynomial [9]. For a polynomial order and for each point $\eta(i)$, the coefficients $g(j)$ must be determined optimally to minimize the least-squares error in fitting a polynomial to all $2M+1$ points in the moving window such that the $\hat{c}(i)$ is the corresponding value of the polynomial curve at position i .

4. RESULTS AND DISCUSSION

In order to evaluate the accuracy of the SGEEMD, a simulated signal $x(t)$ consisting of widely disparate scales, i.e. permanent component of low frequency (100 Hz) and of a transient component of high frequency (1500 Hz) was used to show the resolution of the mode mixing problem and the reduction of residue noise in the reconstructed signal. The signal is described as (Fig.1):

$$x(t) = \sin(2\pi f_1 t) + \lambda \sin(2\pi f_2 t) \left(e^{-\frac{(t-t_0)^2}{\sigma}} + e^{-\frac{(t-t_1)^2}{\sigma}} + e^{-\frac{(t-t_2)^2}{\sigma}} + e^{-\frac{(t-t_3)^2}{\sigma}} \right), 0 \leq t \leq 0.055 \text{ s} \quad (4)$$

With $t_0 = 0.0125 \text{ s}$, $t_1 = 0.0225 \text{ s}$, $t_2 = 0.0325 \text{ s}$, $t_3 = 0.0425 \text{ s}$, $\sigma = 10^{-6}$, $\lambda = 0.1$, $f_1 = 100 \text{ Hz}$ and $f_2 = 1500 \text{ Hz}$.

The test signal was sampled at $f_e = 10000 \text{ Hz}$.

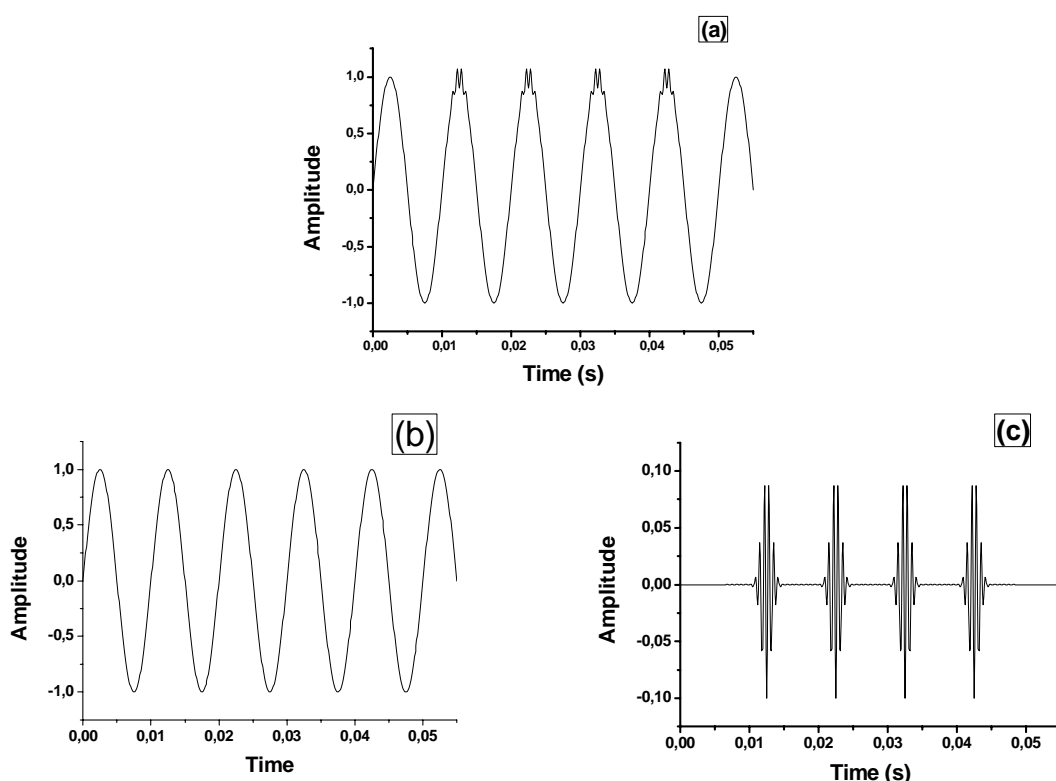


Fig. 1 (a) The simulated signal $x(t)$ and its components: (b) The components of low-frequency and (c) The intermittent of high frequency.

EMD decomposes the signal $x(t)$ into three IMFs (Fig. 2). The IMF1 in "Fig. 2" shows mode-mixing deficiency where both high frequency and low frequency components are mixed. To solve the problem of mode mixing, the EEMD was proposed [2], where Gaussian white noises with finite amplitude are added to the original signal during the decomposition process. However, to overcome the problem of mode mixing, the noise amplitude must be controlled. A suitable choice of the amplitude of the noise is obtained by using the signal to noise ratio SNR [5]. Figure 3a shows the relationship between SNR and IMFs resulting from the EEMD decomposition of signal $x(t)$. Positive values represent the number of redundant IMFs, the value of 0 indicates that there is no redundant IMF, and the value of -1 corresponds to mode mixing. Therefore, "Fig. 3a" shows that SNR within the range of 37-45 dB provides a good EEMD decomposition without mode mixing and also without redundant IMF. The number of ensemble trials must be theoretically infinite to fully remove the impact of the white noise added to the signal. Thus, the number of ensemble trials is also a parameter that must be controlled. In this study, the number of ensemble trials was determined by the correlation coefficient between IMF1 and the corresponding component in the simulated signal. Fig. 3b shows when the number of ensemble trials is 100, the corresponding correlation coefficient is 0.99 which an adequate threshold value to determine the number [5], [8]. The EEMD decomposition result of signal $x(t)$ is shown in "fig. 4", where the $SNR = 37dB$ and $N_t = 100$. As a result, mode mixing is effectively eliminated by the EEMD process. It should be noted however that after 100 trials that IMF1 still contains a very low residue that is visible in "Fig.4a". Although the EEMD method has solved the mode mixing problem, the large number of ensemble trails to reduce the added noise increases the computational time. It has been shown that a solution to the problem of high computational cost of the EEMD method can be obtained by replacing the white noise by a band-limited noise [5], [6]. Such substitution has reduced the number of ensemble trials required to obtain free-noise IMFs, especially by appropriate choice of the filter type and its order [6].

In this work, an improvement of computing time is obtained by filtering the white noise through the SG filter. The parameters of the SG filter were 41 for size, and 3 for the order. The relationship

between the SNR and the SGEEMD decomposition results for the test signal is given in “Fig. 5”. This figure shows that SNR within the range of 30-42 dB provides a good SGEEMD decomposition without mode mixing and also without redundant IMF. Figure 6 shows the decomposition results using SGEEMD. The high frequency component has been easily identified in IMF1 after only 10 trials, instead of the 100 trials required previously. In addition, it can be appreciated in Fig. 6a that the residue in the IMF1 was completely eliminated. So, the proposed method provides a sharper decomposition than that of EEMD Method. The performance of proposed new method was also evaluated using Root Mean Squared Error ($RMSE$) and the correlation coefficient between the IMF1 and the corresponding high-frequency component in the simulated signal $x(t)$. Results are also compared with those of the reference [6], where the white noise was filtered using a low-pass Elliptic filter of 4th order. The table 1 clearly shows the advantage of using a white noise filtered by SG filter. It is seen from table 1 that the percentage improvement of the computational efficiency is 66.66 % compared to MEEM method with 4th order elliptic low-pass filter [6] and 90% compared to the original EEMD method.

In summary, the method here proposed provides an exact reconstruction of the original signal by summing the IMFs with a lower computational cost.

Table 1 Comparative Study Between EEMD ,MEEMD (4th order elliptical low-pass filter) and SGEEMD.

	EEMD	MEEMD (4th order elliptical low-pass filter)	SGEEMD
SNR (dB)	37 dB	10 dB	39 dB
Correlation coefficient	0,99	0,99	0.99
N_t	100	30	10
$RMSE_{IMF1}$	0,0015	0,0019	0.001

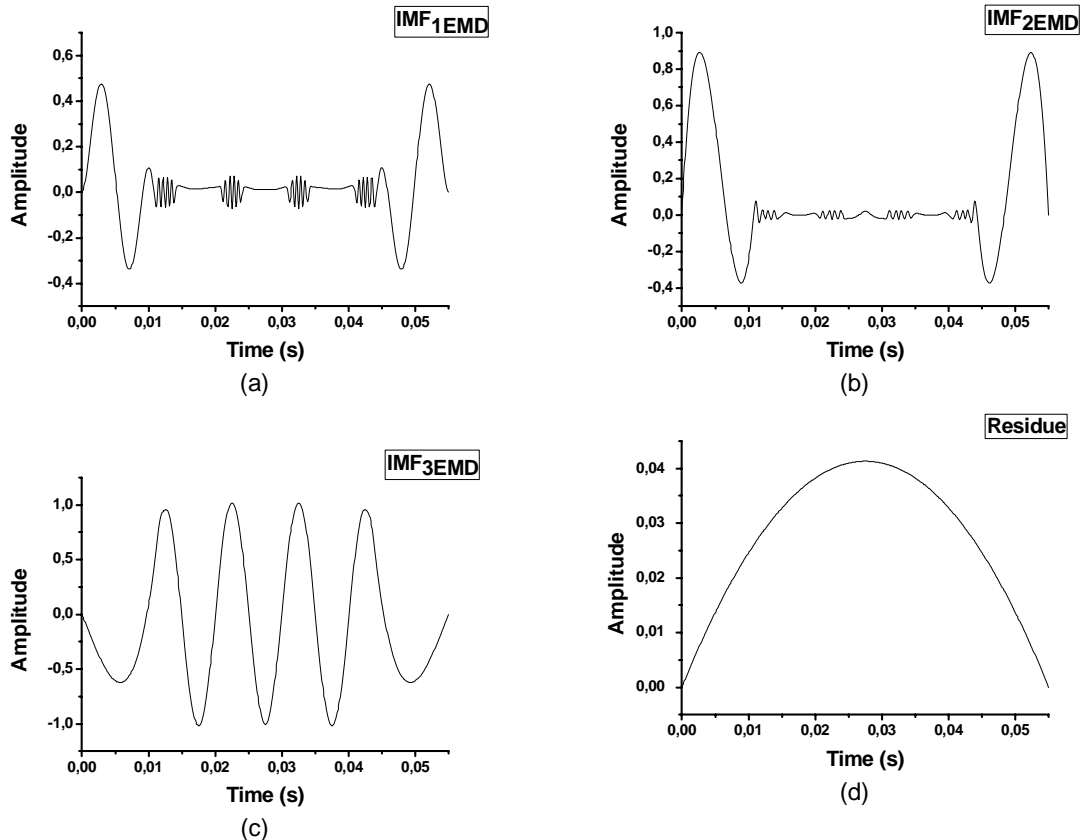


Fig. 2 Decomposition of signal $x(t)$ by EMD method. Mode mixing is observed in IMF_{1EMD} in (a).

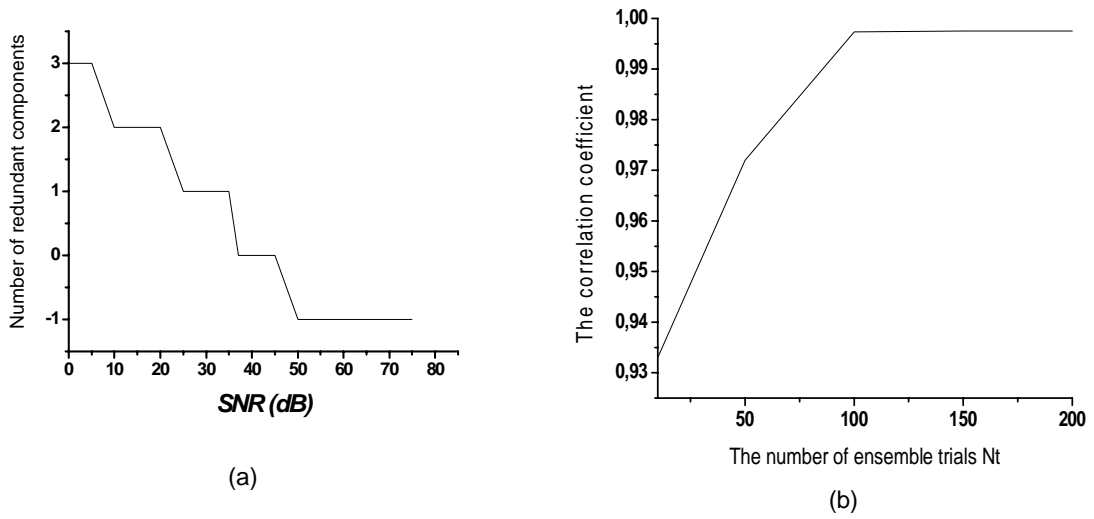


Fig. 3 (a) Relationship between SNR and the decomposition results of the signal $x(t)$ by EEMD method $N_t = 100$.

(b) Relationship between the correlation coefficient and the number of ensemble trials in EEMD method.

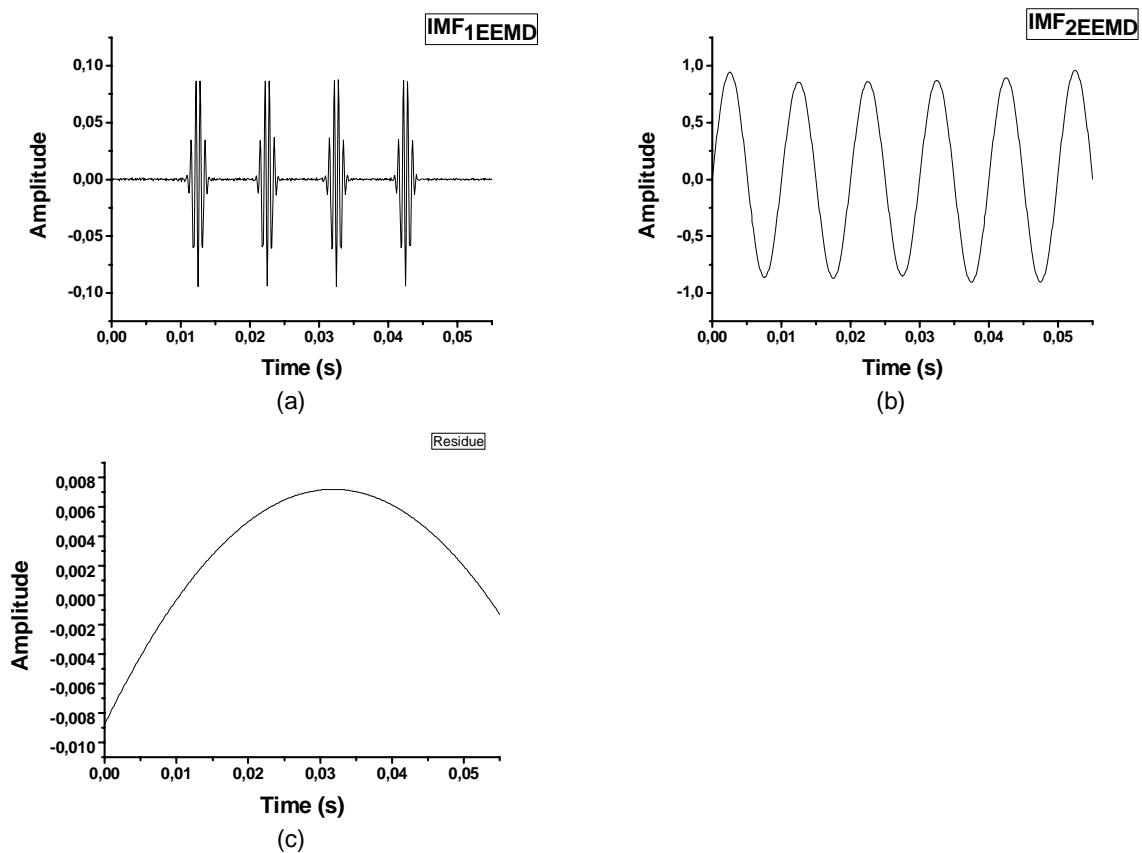


Fig. 4 Decomposition of signal $x(t)$ by EEMD method with $SNR = 37\text{ dB}$ and $N_t = 100$.

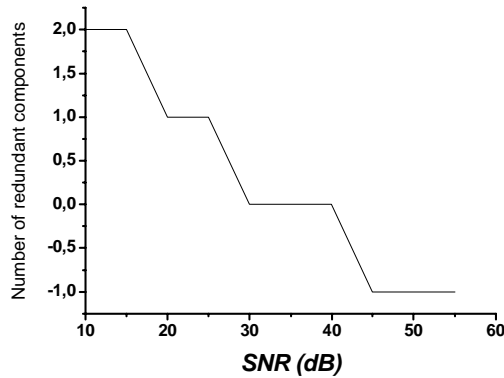


Fig. 5 Relationship between IMFs and SNR of the signal $x(t)$ by SGEEMD method.

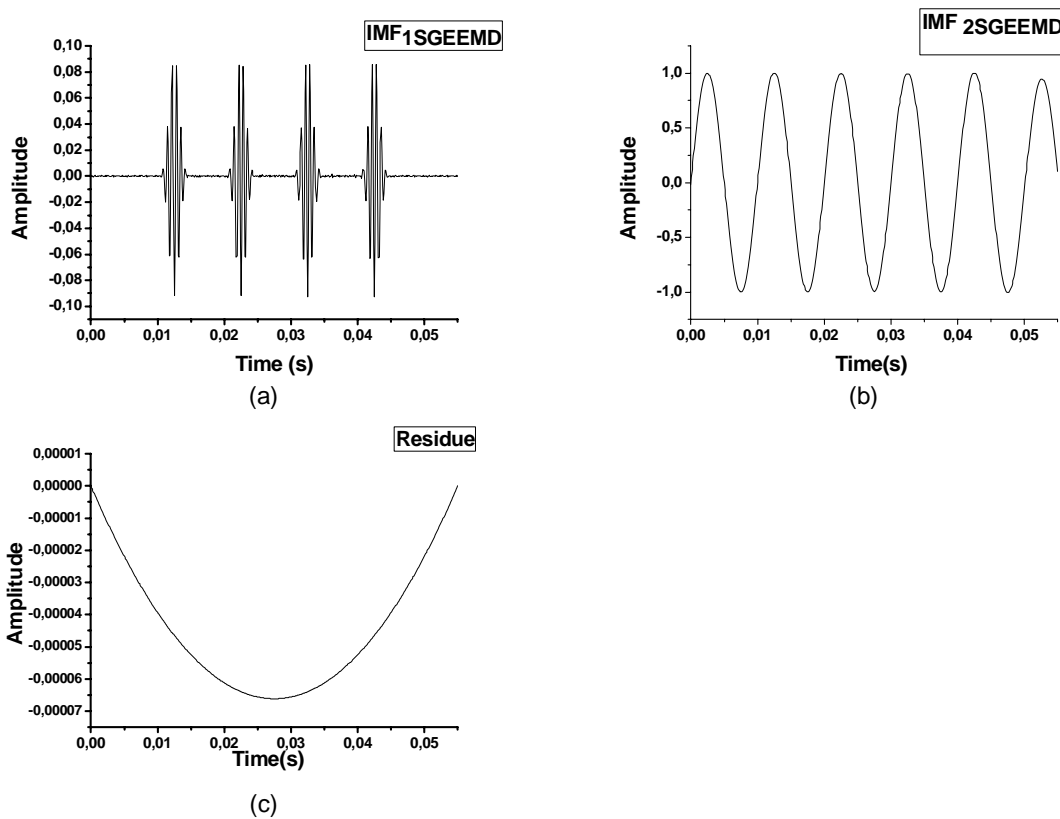


Fig. 6 Decomposition of signal $x(t)$ by SGEEMD with $SNR = 39dB$ and $N_t = 10$.

5. CONCLUSION

In this paper an improved EEMD method, called SGEEMD, has been proposed to reduce the residue noise in the IMFs and thus to allow an exact reconstruction of the original signal whilst also reducing the computational cost of the original EEMD method. This new method uses white noise filtered by SG filter instead of white noise to improve processing efficiency of original EEMD by reducing the number of ensemble trials. In SGEEMD, the high frequency component can be easily identified in the first IMF after 10 ensemble trials, instead of the 100 trials needed by the original method. This represents an improvement of the computational efficiency of approximately 90%. In addition the $RMSE$ derived from SGEEMD to decompose the test signal was smaller than that obtained with the original EEMD.

Finally, The results showed that the amplitude of the added white noise must be chosen appropriately to ensure EEMD performance.

. References

- [1] N. E. Huang, Z. Shen, S. R. Long, M. C. Wu, H. H. Shih, Q. Zheng, N. C. Yen Tung., H. H. Liu, "The empirical mode decomposition and the hilbert spectrum for non-linear and non-stationary time series analysis," *Proceedings of the Royal Society of London*, 454, pp. 903–995, 1998.
- [2] Z. Wu, N. E. Huang, "Ensemble empirical mode decomposition: a noise-assisted data analysis method," *Adv. Adapt. Data Anal.*, vol. 1 (1), pp. 1–41, 2009.
- [3] J. R. Yeh, J. S. Shieh, "Complementary ensemble empirical mode decomposition a novel noise enhanced data analysis method," *Adv. Adapt. Data Anal.*, vol. 2 (2), 135–156, 2010.
- [4] J. D. Zheng, J. S. Cheng, Y. Yang, "Partly ensemble empirical mode decomposition: an improved noise-assisted method for eliminating mode mixing," *Sign. Process.* 96, 362–374, 2014.
- [5] J. Zhang, R. Yan, R. X. Gao, Z. Feng Z., "Performance enhancement of ensemble empirical mode decomposition," *Mechanical Systems and Signal Processing*, vol. 24 (7), pp. 2104-2123, 2010.
- [6] W. Mohguen, R. E. Bekka, "Improvement of ensemble Empirical Mode Decomposition by a band-limited white noise", 2015 4th International Conference on Electrical Engineering (ICEE), Boumerdes, Algeria, pp. 1 - 4, 13-15 Dec. 2015.
- [7] M. E. Torres, M. A. Colominas, G. Schlotthauer, and P. Flandrin, "A complete ensemble empirical mode decomposition with adaptive noise," *IEEE International Conference on Acoustics, Speech and Signal Processing (ICASSP)*, pp. 4144–4147, 2011.
- [8] R. E. Bekka, and Y. Berrouche, "Improvement of ensemble empirical mode decomposition by over-sampling" *Adv. Adapt. Data Anal.*, **5**, (10 pages) 2013.
- [9] X. Xue, J. Zhou, Y. Xu, W. Zhu, C. Li, "An adaptively fast ensemble empirical mode decomposition method and its applications to rolling element bearing fault diagnosis", *Mech. Syst. Sig. Process.* [vol. 62–63](#), pp. 444–459, 2015.
- [10] W. H. Press, B. P. Flannery, S. A. Teukolsky, W. T. Vetterling, "*Numerical Recipes in C: The Art of Scientific Computing*." New York, NY: Cambridge University Press, 1988.